

WASHINGTON UNIVERSITY

Department of Physics

Dissertation Examination Committee:

Henric Krawczynski, Chair

James Buckley

Ramanath Cowsik

Mark Franklin

Martin Israel

Aaron Stump

OBSERVATIONS OF THE ACTIVE GALACTIC NUCLEUS MARKARIAN 421

WITH THE FIRST TWO VERITAS ČERENKOV TELESCOPES

by

Scott Brandon Hughes

A dissertation presented to the
Graduate School of Arts and Sciences
of Washington University in
partial fulfillment of the
requirements for the degree
of Doctor of Philosophy

January 2007

Saint Louis, Missouri

Acknowledgements

I would like to thank my advisor, Dr. Henric Krawczynski, for all his help throughout my graduate school career. Dr. Jim Buckley and Dr. Martin Israel have also been integral in my education, both in serving on my committee as well as being around to provide fresh insight into my work. Thanks to the rest of my thesis defense committee as well for their comments and opinions. I also thank Marty Olevitch, for providing both expert computer programming knowledge and sarcastic, spiteful retorts. I thoroughly appreciate the help from Trevor Weekes and the entire VERITAS collaboration for not only creating a project that I have contributed so much to, but also for their knowledge and assistance with problems too large for me to tackle alone.

I gratefully acknowledge the McDonnell Center for Space Sciences for a fellowship that allowed me to jump-start my research immediately upon entering grad school. Additionally, the staff at Washington University has been most helpful in this important process. Sarah Jordan, Julia Hamilton, Allison Verbeck, Jan Foster, Christine Monteith, Paul Dowkontt, Ira Jung, and Richard Bose, among others, have all been there at one time or another to help with administrative or technical problems that crept up along the way.

I cannot even begin to thank my fellow graduate students, past and present, for their assistance, both intellectual and not so intellectual. In particular, to Jeremy Perkins, Karl Kosack, Paul Rebillot, Lauren Scott, Randy Wolfmeyer, Mairin Hynes, Allyson Gibson, Brian Rauch, Kuen “Vicky” Lee, Trey Garson, Kelly Lave, Frank Gyngard, and honorary grad student Ellen Wurm, as well as many others I am not able to list.

A special thanks goes out to Jason Rosch, who continually helped me to get out and temporarily forget about my problems when the going got tough. Also, to Erica Barnhill, who has been there since college whenever I needed someone to talk to and is always able to cheer me up. In addition, to Morgann Reilly, who unintentionally showed me that things could be much worse, and who was always up for a drink and a movie to distract us both from our troubles at work.

Several others have also helped provide me with joy and amusement outside of school during my stay in St. Louis. Most importantly, the *ANTM* crew—Danette Wilson, Rose Martelli, Amber Specter, and Allyson Gibson (who does in fact deserve to be mentioned again)—for that much-needed downward spiral into trashy TV. Anna MacKay has also provided entertainment, though in much more than a “guilty pleasure” capacity. Finally, I must thank all my friends out in Phoenix. Most important of these is Mike Drabick, who not only let me crash at his place when I needed to get away, but without whom I would never have met any of the many other wonderful people I have come to know in my visits out there.

Contents

Acknowledgements	ii
List of Figures	viii
List of Tables	ix
Abstract	x
Copyright	xii
1 Summary of Thesis Work	1
2 Astrophysics of Blazars	4
2.1 Introduction to γ -ray Astrophysics	4
2.2 Instruments to Detect γ -rays	6
2.2.1 Space-based Instruments	6
Compton Gamma Ray Observatory	7
Swift	8
GLAST	9
2.2.2 Ground-based Instruments	10
Imaging Atmospheric Čerenkov Telescopes	10
Čerenkov Solar Array Telescopes	12
Particle Air Shower Arrays	14
2.3 TeV γ -ray Sources	14
2.4 Blazars	20
2.4.1 Spectral Energy Distributions	21
2.4.2 Emission Models and Particle Acceleration	23
Synchrotron Self-Compton	23
External Compton	24
Hadronic Models	25
Particle Acceleration	25
2.4.3 Markarian 421	26

3	γ-ray Detection and VERITAS	28
3.1	γ -ray Propagation	28
3.1.1	Propagation Through Space	29
3.1.2	Air Showers in the Atmosphere	29
	γ -ray Induced Showers	30
	Čerenkov Radiation	31
	Cosmic Ray Induced Showers	33
3.2	Detection Using an Imaging Atmospheric Čerenkov Telescope (IACT)	33
3.2.1	Atmospheric Technique	33
3.2.2	Imaging Čerenkov Radiation	35
3.3	VERITAS: Very Energetic Radiation Imaging Telescope Array System	37
3.3.1	Telescope Array	37
3.3.2	Camera	39
3.3.3	Trigger	42
3.3.4	Data Acquisition	43
4	Mrk 421 Data Analysis	44
4.1	Event Reconstruction	44
4.1.1	Hillas Parameterization	45
4.1.2	Stereo Reconstruction	47
4.1.3	Analysis Tools	50
4.2	Data Cuts and Significances	51
4.3	Spectral Reconstruction	52
4.4	Mrk 421 Data from April–May 2006	53
4.4.1	Observation Modes	53
	ON–OFF Pairs	54
	Tracking Runs	54
	Wobble Runs	56
4.4.2	Final Data Set	56
4.5	Comparison of Experimental and Monte Carlo Data	58
4.6	First Stereo Results from VERITAS	64
4.6.1	Cutting on θ^2	65
4.6.2	Cutting on Mean Scaled Width	67
4.6.3	Mrk 421 Light Curve	68
4.6.4	Energy Spectrum	70
5	SSC Modeling of Blazar Emission	71
5.1	Rationale	71
5.2	Measurement of the Jet Magnetic Field	72
5.3	Synchrotron Self-Compton Simulations	74
5.4	Generating Data Sets	76
5.5	Analysis Procedure	81
5.6	Measuring Time Lags with the Discrete Correlation Function (DCF) .	84

5.7	Comparing of DCF Time Lags to Expected Results	91
6	Discussion	94
6.1	Summary of Thesis Results	94
6.2	VERITAS Performance	95
6.3	The Future of γ -ray Astrophysics	97
A	X-ray Data Analysis of 1ES 1959+650 and Mrk 421	99
A.1	Multiwavelength Campaign Overview	99
A.2	RXTE Data	100
A.3	“Orphan” Flares	102
B	Daily VERITAS Data Quality Monitoring	105
B.1	Motivation and Procedure	105
B.2	Analysis and Results	106
B.3	The <i>dt</i> Bump	110
C	VAC: VERITAS Array Control GUI	112
C.1	Starting <i>VAC</i>	113
C.1.1	Normal Operation	113
C.1.2	Debugging Systems	114
C.2	Using the <i>VAC</i>	115
C.2.1	Main Window	115
	System Status	115
	Run Management	118
	Run Info for Current Active Run	123
	L2/L3 Rate Plot	124
C.2.2	Observer Menu	125
C.2.3	Test Runs Menu	129
C.2.4	Subsystems Menu	130
	L3 Subsystem	130
	Harvester Subsystem	132
	Event Builder Subsystem	133
	L2 Subsystem	135
	L1 Subsystem	136
	Database Subsystem	136
	Charge Injection (QI) Subsystem	139
	Custom Night	139
C.2.5	Settings Menu	141
	Put CFD Settings	141
	CFD Settings	142
	FADC Settings	142

List of Figures

2.1	The Compton Gamma Ray Observatory (CGRO)	7
2.2	The Gamma-ray Large Area Space Telescope (GLAST)	9
2.3	The Whipple 10 m Telescope	11
2.4	The H.E.S.S. Telescopes	13
2.5	Sky Map of γ -ray Sources	15
2.6	The Crab Nebula	18
2.7	Schematic of an Active Galactic Nucleus	20
2.8	Sample Spectral Energy Distribution	22
2.9	X-ray Light Curve of Mrk 421 with Flares	27
3.1	Electromagnetic Cascading Air Shower	30
3.2	Čerenkov Radiation	31
3.3	Charged Particle Polarizing the Surrounding Medium	32
3.4	Cosmic Ray Air Showers	34
3.5	Cosmic Ray vs. γ -ray Air Showers	36
3.6	Layout of the Four VERITAS Telescopes	38
3.7	A 12 m VERITAS Telescope	40
3.8	PMT Camera	41
4.1	Hillas Parameters	46
4.2	Images of Sky Showers	48
4.3	Stereo Shower Reconstruction	49
4.4	OFF regions	55
4.5	Comparing Monte Carlo Simulations to Data	60
4.6	Energy Threshold of Monte Carlo Simulations	61
4.7	Angular Resolution of Monte Carlo Simulations	62
4.8	Core Resolution of Monte Carlo Simulations	63
4.9	True vs. Reconstructed Energy for the Monte Carlo Simulations	64
4.10	Plots of θ^2	66
4.11	Q-factor for θ^2	67
4.12	Plot of $MSCW$	68
4.13	Q-factor for $MSCW$	68
4.14	Mrk 421 Light Curve	69
4.15	Energy Spectrum of Mrk 421	70

5.1	Sample Input of Simulated Flares	77
5.2	SEDs of Simulated Data Sets	79
5.3	Light Curves of Simulated Data Sets	80
5.4	DCF from Simulated Data	85
5.5	Actual vs. Calculated Lag Times	87
5.6	Actual vs. Calculated B Fields	88
5.7	DCF over Different Energy Ranges	89
5.8	DCF for Flares of Different Durations	90
6.1	Observatory Sensitivity	96
A.1	“Orphan” Flare of 1ES 1959+650	103
B.1	Representative Good DDQM Plots	108
B.2	Representative Poor DDQM Plots	109
B.3	The dt Bump	111
C.1	Main VAC Window	116
C.2	Define Run Window	118
C.3	Run Info Window	128
C.4	L3 Subsystem Window	130
C.5	Harvester Subsystem Window	132
C.6	Event Builder Subsystem Window	134
C.7	L2 Subsystem Window	135
C.8	Database Subsystem Window	137
C.9	Custom Night Window	140
C.10	Put CFD Settings Window	141

List of Tables

2.1	γ -ray Nomenclature	5
2.2	TeV γ -ray Sources	16
4.1	Final Mrk 421 Data Set	57
4.2	Monte Carlo Angular Resolution	62
5.1	Parameters for Simulated Data Files	78
5.2	Calculated and Observed Time Lags	86
5.3	Observed and Calculated B fields	87

Abstract

This thesis describes two projects, the first of which is the analysis of data from the VERITAS (Very Energetic Radiation Imaging Telescope Array System) experiment. VERITAS, an array of ground-based γ -ray telescopes in southern Arizona, USA, has been taking data in hardware stereo mode since March, 2006. The April–May 2006 dark run provided a large set of data from two telescopes on the known blazar Markarian (Mrk) 421. An initial analysis of the 14.3 hours of stereo data produced a light curve and confirmed a detection on the 39 sigma level with a γ -ray rate of $2.91 \pm 0.07 \gamma \text{ min}^{-1}$, reduced from an inferred value of $8.83 \pm 0.21 \gamma \text{ min}^{-1}$ before analysis cuts. The analysis shows the two-telescope array’s energy threshold to be 165 GeV before cuts and 220 GeV after cuts, with an angular resolution of 0.16° . These data were also used to extract an energy spectrum for Mrk 421. This initial analysis allows a test of the performance of the two-telescope array and gives an idea of the data that will come from the full system. The remaining two VERITAS telescopes will be brought online by January, 2007. As a second project, computer simulations were used to model Synchrotron Self-Compton (SSC) emission from blazars that will be relevant for future multiwavelength campaigns. The Discrete Correlation Function

(DCF) was used to calculate the source's magnetic field based on the time lag between emission in different X-ray energy bands. This method, used by different authors in the literature, was shown to overestimate the magnetic field by as much as a factor of six. Understanding the behavior of properties such as this will allow the breaking of model degeneracies and give insight into the physical processes involved in particle acceleration of blazars.

This work is licensed under the Creative Commons
Attribution-NonCommercial-ShareAlike2.5 License.

To view a copy of this license, visit

<http://creativecommons.org/licenses/by-nc-sa/2.5/>

or send a letter to

Creative Commons,

543 Howard Street, 5th Floor,

San Francisco, California, 94105, USA.



Chapter 1

Summary of Thesis Work

For this thesis, I looked at the first true stereo data taken with two of the planned four VERITAS¹ γ -ray telescopes. The April–May 2006 dark run provided a large amount of data on the known blazar Markarian (Mrk) 421. These data were used to verify that the VERITAS system is performing as expected. They were also used to determine some loose data cuts to use in the future. Also, VERITAS’s first energy spectrum of this source was derived. The results of this initial data analysis help us understand what type of data we may get once the entire telescope system is up and running. It will also allow us to tweak our simulations so they more accurately model the telescopes’ behavior.

Operating the VERITAS experiment requires software. I worked to design and

¹ VERITAS (Very Energetic Radiation Imaging Telescope Array System) is supported by grants from the U. S. Department of Energy, the U. S. National Science Foundation, the Smithsonian Institution, by NSERC in Canada, by Science Foundation Ireland, and by PPARC in the U. K. It is being built through a collaboration of nine primary universities and the Smithsonian Astrophysical Observatory, as well as several other contributing institutions. <http://veritas.sao.arizona.edu>

write the entire graphical interface to *arrayctl*, the array control program written by Marty Olevitch. *arrayctl* is responsible for coordinating and overseeing all data taking processes for the entire array. The graphical interface, called *VAC* (VERITAS Array Control), can oversee many aspects of daily observation. It is used to manage data taking, and also displays feedback and data plots from the various subsystems to ensure system and data integrity. *VAC* has become the most important and most depended upon piece of software for VERITAS telescope operation.

Observations have to be complemented with theoretical modeling to reveal the physical processes that produce the observed emission. I worked with a Synchrotron Self-Compton (SSC) simulation code to explore time lags in the light curves measured in different observational bands. Using the Discrete Correlation Function (DCF), one can determine this lag. From that, it is a common approach to calculate the magnetic field of the source. Various parameters were altered and different scenarios tried in order to test the accuracy of this method. Understanding the behavior of properties such as this will allow the breaking of model degeneracies and give insight into the physical processes involved in particle acceleration of blazars.

The text of this thesis is organized as follows. An introduction to γ -ray astrophysics is covered in Chapter 2, focusing on blazars and their observation. A description of how γ -rays are detected on Earth, and the VERITAS telescopes in particular, are covered in Chapter 3. Following are details on the analysis and results from the first VERITAS stereo data in Chapter 4. A complete description of the SSC simulations used to test the DCF as a tool for measuring the magnetic field of sources is

given in Chapter 5, concluding with a discussion of all results, as well as the future of γ -ray astrophysics and VERITAS, in Chapter 6.

The Appendices describe various other studies I have performed during the course of this thesis. A brief overview of the X-ray analyses of Mrk 421 and 1ES 1959+650 are covered in Appendix A. A summary of daily data quality monitoring (DDQM) for the VERITAS telescopes is given in Appendix B. Finally, a description and User's Manual for the graphical interface *VAC* is presented in Appendix C.

Chapter 2

Astrophysics of Blazars

2.1 Introduction to γ -ray Astrophysics

At the high-energy end of the electromagnetic spectrum lie what are called “ γ -rays”. Photons in this range have the shortest wavelengths, and energies from around 500 keV to through TeV and even higher. The energy range covered by γ -rays is more than that of the rest of the electromagnetic spectrum combined (Weekes, 2003). In order to talk about γ -rays, it is appropriate to divide the energy range into smaller sections of similar behavior and detection techniques. Table 2.1 lists the common nomenclature and their corresponding energy ranges.

In order to produce γ -rays, charged particles (electrons, positrons, protons, or other nuclei) must be accelerated to extremely high energies. The particles then emit radiation, which travels through space as γ -rays. There are several relevant emission mechanisms. Synchrotron radiation is emitted when a relativistic charged particle

TABLE 2.1: The common divisions within the span of γ -ray energies, including common descriptive names.

Common Name	Energy Range
Low (LE)	500 keV – 10 MeV
Medium (ME)	10 MeV – 30 MeV
High (HE)	30 MeV – 30 GeV
Very High (VHE)	30 GeV – 30 TeV
Ultrahigh (UHE)	30 TeV – 30 PeV
Extremely High (EHE)	30 PeV and up

spirals around a magnetic field line. To generate TeV photons by this mechanism, either rather strong magnetic fields ($\gg 1$ G) or extremely high-energy electrons or protons are required. Another process is Bremsstrahlung, which occurs when an electron is decelerated by the electromagnetic field of a charged particle or particles. The “braking radiation” produced is a result of the energy loss by the electron, and can be quite substantial. Perhaps the most important process is inverse Compton scattering. When a low-energy photon collides with an energetic electron, it can be scattered to much higher energies. All these processes are described in detail in Section 2.4.2.

γ -rays can be detected through their interaction with matter. Different energy ranges lend themselves to different dominant interaction processes. For the lowest-energy γ -rays, photoelectric absorption is the dominant process. A γ -ray can eject an electron from a tightly bound atom, which also emits an X-ray as the resulting hole in the atom is filled by an electron from a higher orbit. Both the ejected electron and X-ray can be used to detect the original γ -ray. Mid-range γ -rays prefer Compton

scattering. Here, a γ -ray collides with a loosely bound electron, giving up some of its energy. Multiple collisions can occur for the same incident γ -ray. For higher-energy photons, the dominant process is pair production. If the γ -ray photon has energy

$$E_\gamma > 2m_0c^2 = 1.022 \text{ MeV} \quad (2.1)$$

where m_0 is the rest mass of the electron, it can convert to an electron-positron pair in the presence of an atomic nucleus, required for momentum conservation.

2.2 Instruments to Detect γ -rays

Being uncharged and therefore unaffected by magnetic fields permeating the universe, γ -rays are very directional and arrive at Earth from distinct points in the sky. The Earth's atmosphere is opaque to γ -rays, so the only way to see them directly is from space. However, indirect techniques have been developed to observe γ -ray sources from the ground as well (see Sect. 2.2.2).

2.2.1 Space-based Instruments

Early balloon experiments detecting cosmic rays suggested that moving beyond the Earth's atmosphere might be advantageous to finding even higher-energy γ -rays. Despite its small collection area and poor angular resolution, the Explorer XI satellite, launched in 1965, was able to prove the existence of γ -rays originating outside the Earth's atmosphere (Clark *et al.*, 1968). The practice of using balloons for flying spark chambers to detect γ -rays was effectively ended in 1972 with the launch of



FIGURE 2.1: A collection of several instruments including EGRET (center) and BATSE (eight detectors, one on each corner of the spacecraft), the Compton Gamma Ray Observatory was highly successful in observing a wide range of γ -ray phenomena. Figure from <http://cossc.gsfc.nasa.gov>.

NASA's SAS-2. The European Space Agency's COS-B was launched soon after in 1975. By helping map the γ -ray sky in detail, both these telescopes established γ -ray astronomy as a new and exciting field worthy of further study.

Compton Gamma Ray Observatory

The most successful space-based γ -ray telescope to date has been the Compton Gamma Ray Observatory (CGRO; Gehrels *et al.*, 1993), shown in Figure 2.1. Launched in 1991, it remained in orbit for over nine years. It was built to observe γ -rays over the energy range of 15 keV – 30 GeV with several different instruments.

Each of the instruments onboard the CGRO was designed for a specific purpose. The Burst and Transient Source Experiment (BATSE) was able to detect γ -ray bursts (GRBs) on microsecond time scales in the 20 keV – 1.9 MeV energy range. The Compton Telescope (COMPTEL) provided the first sky survey in the 1 – 30 MeV band. The Oriented Scintillation Spectroscopy Experiment (OSSE) performed spectral observations in the 0.05 – 10 MeV energy range.

The final instrument was EGRET, the Energetic Gamma Ray Experiment Telescope. Operating at the highest energies of any of CGRO's components (10 MeV – 30 GeV), EGRET was able to detect over 250 new γ -ray sources in its lifetime, 66 of which were blazars (Thompson *et al.*, 1995; Hartman *et al.*, 1999). The detector itself was massive. The amount of material needed to stop the high energy photons had a mass of 1900 kg and was approximately the size of a compact car, yet had an effective collection area of only 1600 cm² (Fichtel *et al.*, 1993). More recent experiments are able to accomplish more with a lighter detector.

Swift

With the retirement of the CGRO, we were left without a reliable method to detect and report GRBs. Then, in 2004, NASA launched Swift (Burrows *et al.*, 2003), which contained the Burst Alert Telescope (BAT) with five times the sensitivity of BATSE. The satellite is also made up of telescopes for monitoring these bursts in X-rays, UV, and optical bands. This multiwavelength ability helps Swift to detect GRB positions within a few arc seconds.



FIGURE 2.2: Set to launch in 2007, GLAST represents the future of space-based γ -ray astronomy.

GLAST

Set to launch in 2007, the Gamma-ray Large Area Space Telescope (GLAST; see Fig. 2.2) is the successor of EGRET, and will be able to detect sources from 20 MeV – 300 GeV (Ritz *et al.*, 2005). Its sensitivity will be almost 10 times that of EGRET and it will have about twice the field of view. Like EGRET, GLAST is a pair production telescope. The primary γ -ray interacts with the detector and creates an electron-positron pair. The two charged particles are then tracked through the detector volume. The tracks point back towards the incident direction of the primary γ -ray. GLAST will also have a basic ability to detect GRBs. The experiment is described in more detail in Section 6.3.

Though many technological advancements are being made, limits to the physical size of these space-borne detectors, as well as the sources' steep spectra at higher

energies, prevent their being used to detect γ -rays at energies > 300 GeV. To probe higher energy γ -rays, it is necessary to use ground-based detectors.

2.2.2 Ground-based Instruments

The Earth's atmosphere is opaque to γ -rays. However, it is still possible to detect the results of their interactions with the Earth's atmosphere. This process is described more in Chapter 3. Ground-based techniques have proven highly effective in observing and discovering new sources of γ -rays. Čerenkov telescopes in particular have discovered TeV emission from seven blazars, five of which were not detected by EGRET (Horan and Weekes, 2004; Aharonian *et al.*, 2005a).

Imaging Atmospheric Čerenkov Telescopes

Taking over where space-based detectors leave off, Imaging Atmospheric Čerenkov Telescopes (IACTs) operate in the 30 GeV – 30 TeV range. First proposed by Weekes and Turver (1977), this technique is based on detecting flashes of Čerenkov light resulting from interactions as the primary γ -ray passes through Earth's atmosphere. It is discussed further in Section 3.2.

Stand-alone IACTs have been operating for years with optical reflectors ranging from 3 – 17 m in diameter. Examples of early and present telescopes include CAT in France (Barrau *et al.*, 1998), the Whipple 10 m in Arizona, USA (Cawley *et al.*, 1990), and MAGIC in the Canary Islands (Lorenz and Martinez, 2005). An example of this type of telescope can be seen in Figure 2.3.



FIGURE 2.3: Located on Mt. Hopkins in southern Arizona, USA, the Whipple 10 m telescope is an example of an Imaging Atmospheric Čerenkov Telescope.

The current trend in IACTs is to use an array of telescopes all looking at the same source and requiring multiple telescope coincidences for the array to trigger. This method, first pioneered by HEGRA (Pühlhofer *et al.*, 2003), has several advantages over single telescopes. Arrays of IACTs provide a large effective area ($> 100 \text{ m}^2$), excellent suppression of cosmic ray initiated air showers and local muons, lower energy threshold, improved angular resolution, and better flux sensitivity, as well as better energy resolution compared to their single-telescope counterparts.

Recently, most new discoveries have come from the H.E.S.S. (High Energy Stereoscopic System) array in Namibia, Africa (Aharonian *et al.*, 2005d). Shown in Figure 2.4, H.E.S.S. consists of four 12 m telescopes and has been able to detect an astounding number (~ 30) of new sources since coming online in 2003.

Other arrays of IACTs are currently being built around the world. VERITAS, described in Section 3.3, is nearing completion in southern Arizona, USA. The MAGIC Collaboration is also building a second telescope at their current site to create the two-telescope array MAGIC II.

Čerenkov Solar Array Telescopes

Čerenkov light can also be collected by the large mirrors of solar detectors. Originally proposed by Danaher *et al.* (1982), several groups such as STACEE (Gingrich *et al.*, 2005) and CELESTE (Smith *et al.*, 2006) have since implemented the technique. Čerenkov radiation is reflected off the large solar mirrors and focused onto photomultiplier tubes (PMTs). The shower direction is inferred from the arrival



FIGURE 2.4: The four H.E.S.S. telescopes, located in Namibia, Africa, are an example of an array of IACTs.

times of the light from each of the solar panels. Due to their large collection area, these telescopes have lower operating energies than single IACTs.

Particle Air Shower Arrays

Though originally built to study the properties of cosmic rays (Ter Haar, 1950), particle air shower arrays can be used to study γ -rays in the TeV–PeV energy regime. The most successful such detector is MILAGRO, located in New Mexico, USA, which operates at ~ 1 TeV (Dingus *et al.*, 2000). Inside a large pool of water are 723 PMTs used to detect residual particles from air showers. However, this type of detector achieves a limited separation between charged cosmic rays and γ -rays (see, *e.g.*, Catanese and Weekes, 1999).

2.3 TeV γ -ray Sources

Just as there is not one mechanism to detect the whole range of γ -rays, there are also many types of sources from which these rays can originate. The number of sources detected has sharply increased in recent years as well, due mostly to the H.E.S.S. telescopes in the Southern Hemisphere. A similar increase in new sources in the Northern Hemisphere should happen shortly, when VERITAS comes fully online. Figure 2.5 shows a map of the sky in galactic coordinates, with all known TeV sources labeled. These sources are also listed in Table 2.2

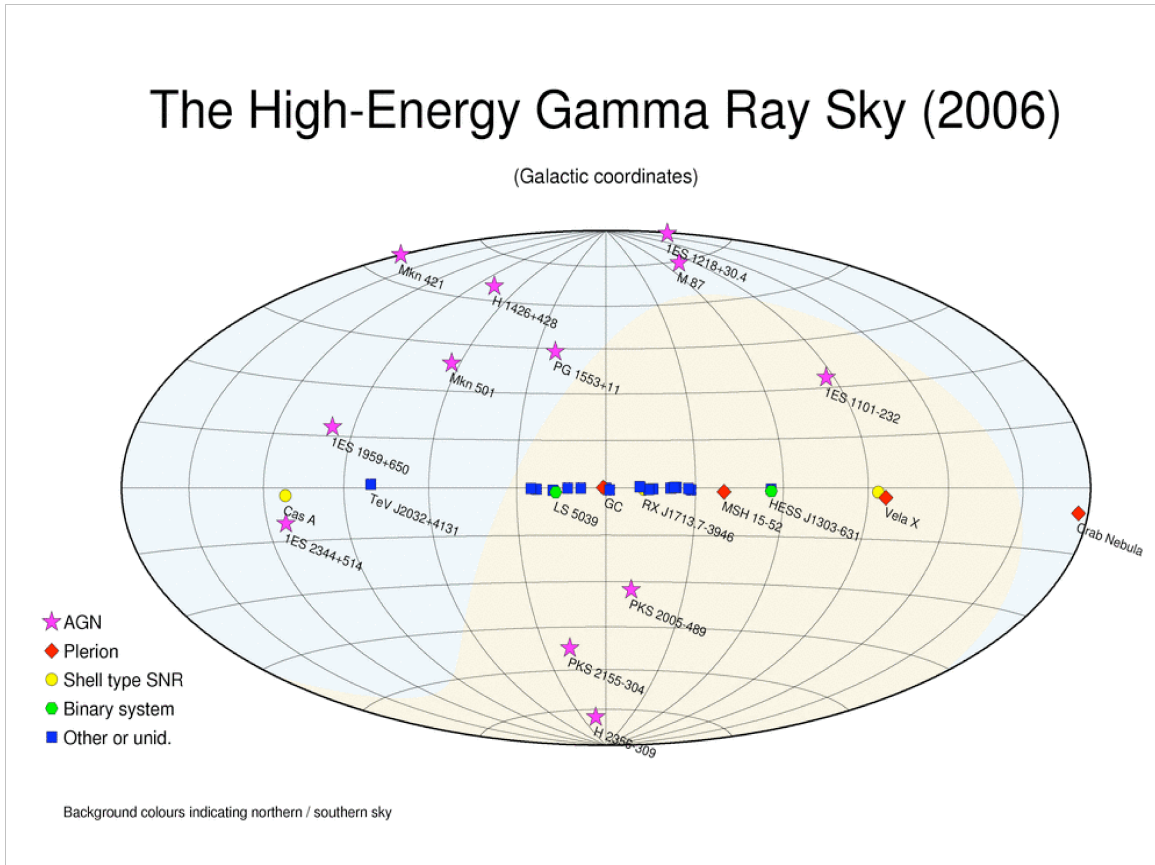


FIGURE 2.5: Map of the sky in galactic coordinates showing TeV γ -ray sources. Figure from Hermann (2006).

TABLE 2.2: Known TeV sources as of July, 2006. Sources are divided by class. Table from Cui (2006).

Name	RA (2000)	Dec (2000)	Notes
<i>Blazar:</i>			
1ES 1101–232	11 03 37.57	–23 29 30.2	
Mrk 421	11 04 27.31	+38 12 31.8	
Mrk 180	11 36 26.41	+70 09 27.3	
1ES 1218+304	12 21 21.94	+30 10 37.1	
H 1426+428	14 28 32.6	+42 40 29	
PG 1553+113	15 55 43.04	+11 11 24.4	
Mrk 501	16 53 52.22	+39 45 36.6	
1ES 1959+650	19 59 59.85	+65 08 54.7	
PKS 2005–489	20 09 25.39	–48 49 53.7	
PKS 2155–304	21 58 52.07	–30 13 32.1	
1ES 2344+514	23 47 04.92	+51 42 17.9	
H 2356–309	23 59 07.8	–30 37 38	
<i>Radio Galaxy:</i>			
M 87	12 30 49.42	+12 23 28.0	
<i>Plerion:</i>			
Crab Nebula	05 34 31.97	+22 00 52.1	PSR B0532+21
Vela X	08 33 32	–45 43 42	PSR B0833–45
G313.3+0.1	14 18 04	–60 58 31	“Rabbit” (R2/Kookaburra)
K3/Kookaburra	14 20 09	–60 48 36	PSR J1420–6048
MSH 15–52	15 14 07	–59 09 27	PSR B1509–58; composite
G18.0–0.7	18 26 03.0	–13 45 44	PSR J1826–1334
<i>Shell-Type SNR:</i>			
RX J0852.0–4622	08 52 00	–46 20 00	“Vela Junior”
RX J1713.7–3946	17 13 00	–39 45 00	G347.3–0.5
G0.9+0.1	17 47 23.2	–28 09 06	composite
G12.82–0.02	18 13 36.6	–17 50 35	
Cas A	23 23 24	+58 48 54	
<i>Pulsar:</i>			
LS 5039	18 26 15	–14 50 53.6	
LS I +61 303	02 40 31.67	+61 13 45.6	also an X-ray binary
<i>X-ray Binary:</i>			
PSR B1259–63	13 02 47.65	–63 50 08.7	
<i>Unidentified:</i>			
HESS J1616–508	16 16 23.6	–50 53 57	PSR J1617–5055
HESS J1632–478	16 32 08.6	–47 49 24	IGR J16320–4751
HESS J1634–472	16 34 57.2	–47 16 02	G337.2+0.1/IGR J16358–4726

Continued on next page...

TABLE 2.2 – Continued

Name	RA (2000)	Dec (2000)	Notes
HESS J1640–465	16 40 44.2	–46 31 44	G338.3–0.0/3EG J1639–4702
HESS J1713–381	17 13 58.0	–38 11 43	G348.7+0.3
HESS J1745–290	17 45 41.3	–29 00 22	G359.95–0.04/SgrA East/SgrA*
HESS J1804–216	18 04 31.6	–21 42 03	G8.7–0.1/PSR J1803–2137
HESS J1834–087	18 34 46.5	–08 45 52	G23.3–0.3
HESS J1837–069	18 37 37.4	–06 56 42	G25.5+0.0/AX J1838–0655
HESS J1303–631	13 03 00.4	–63 11 55	
HESS J1614–518	16 14 19.0	–51 49 07	
HESS J1702–420	17 02 44.6	–42 04 22	
HESS J1708–410	17 08 14.3	–41 04 57	
HESS J1745–303	17 45 02.2	–30 22 14	3EG J1744–3011
TeV J2032+4131	20 31 57	+41 29 56.8	

There are several classes of TeV γ -ray sources, the first of which are supernova remnants (SNRs). The expanding shell of gas from a supernova explosion consists of stellar material altered by the explosion as well as parts of the interstellar medium swept up during expansion. In shell-type SNR, like RX J1713.7–3946, the emission appears to come from an outer shell with no apparent central power source. Plerions, like the Crab Nebula, are thought to be powered by a central pulsar.

The Crab Nebula is a particularly interesting TeV source for many reasons. The supernova that created it exploded in 1054 AD and was observed by Chinese astronomers. It left behind a bright spot in the sky visible in daylight for weeks after. The Crab was the first confirmed TeV γ -ray source, discovered by Weekes *et al.* (1989). It has since become known for its strong, steady signal. Today it is used as the “standard candle” by which all γ -ray observations are measured. A view of the Crab with the Hubble Space Telescope can be seen in Figure 2.6.

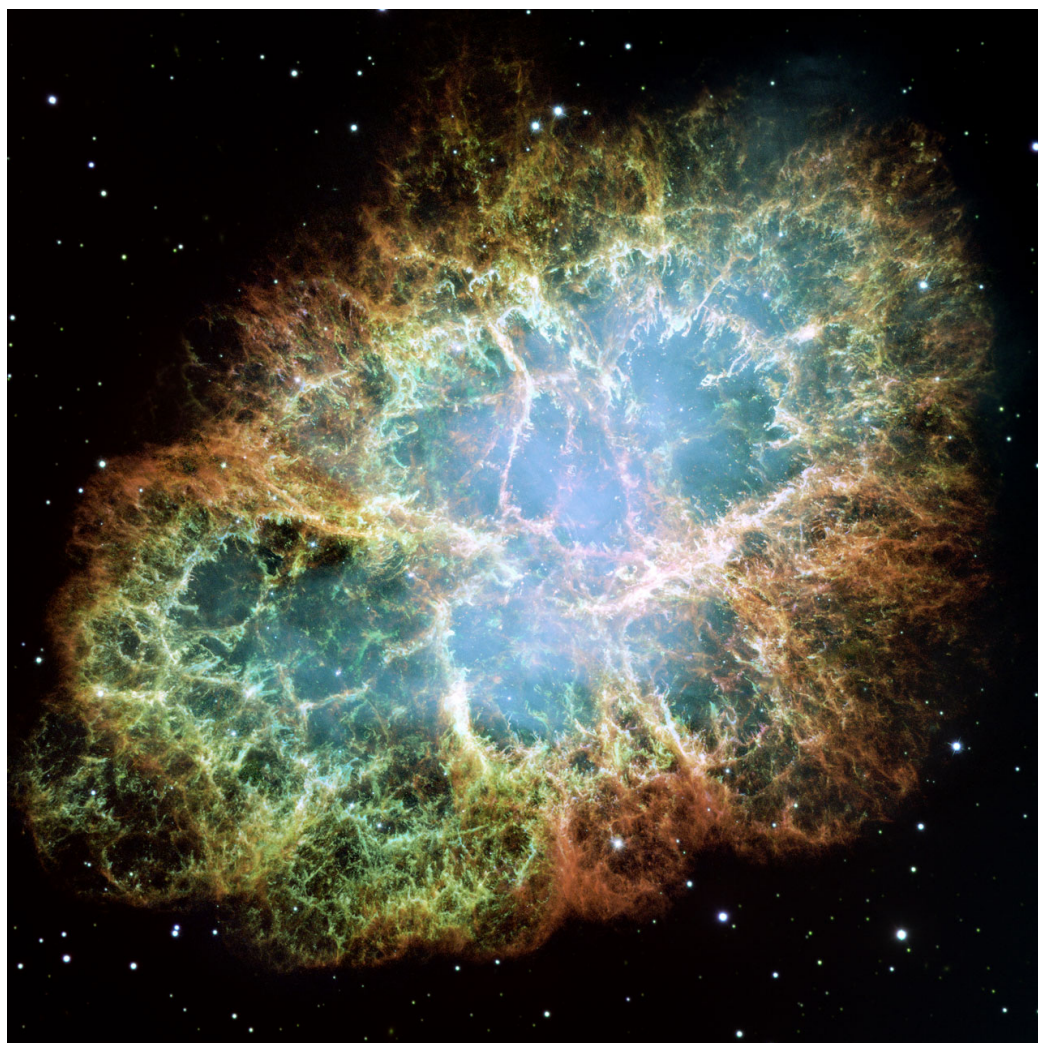


FIGURE 2.6: The Crab Nebula as seen by the Hubble Space Telescope. The image is 6.5 arcmin across, corresponding to 3.4 pc at a distance of ~ 2 kpc.

Another known source class for TeV emission is X-ray binaries (XRBs). Though mainly emitting X-rays, they also have been known to produce sporadic γ -ray emission from the gas accreting onto the compact star in the binary pair. So far only two XRB sources of γ -rays have been detected, PSR B1259–63 (Aharonian *et al.*, 2005b) and LS I +61303, also a pulsar (Albert *et al.*, 2006).

The largest group of sources from which γ -rays have been detected are Active Galactic Nuclei (AGN). These galaxies contain a very compact core emitting an extremely disproportionate amount of energy compared to the rest of the galaxy. This central engine is thought to be a supermassive black hole surrounded by an accretion disk (see Fig. 2.7). The disk is surrounded by fast-moving clouds of dust that, in some cases, obscure the central engine from view, though these clouds can produce Doppler-broadened emission lines. Farther from the nucleus, in the direction perpendicular to the plane of the accretion disk, narrow emission lines are produced through scattering of the slower (less Doppler broadening) and less dense clouds surrounding the galaxy. In some AGN, jets of highly relativistic particles are ejected out the poles of the spinning central nucleus. These jets contain large magnetic fields capable of producing synchrotron radiation up to X-ray wavelengths. Inverse Compton scattering from the jets' relativistic electrons can also produce γ -rays. All but one AGN detected in TeV γ -rays are part of the subclass known as blazars, discussed further in Section 2.4. The one exception is the nearby radio galaxy M87 (Aharonian *et al.*, 2003, 2006). Its jet is believed to be at an angle of $\sim 30^\circ$ to the line of sight.

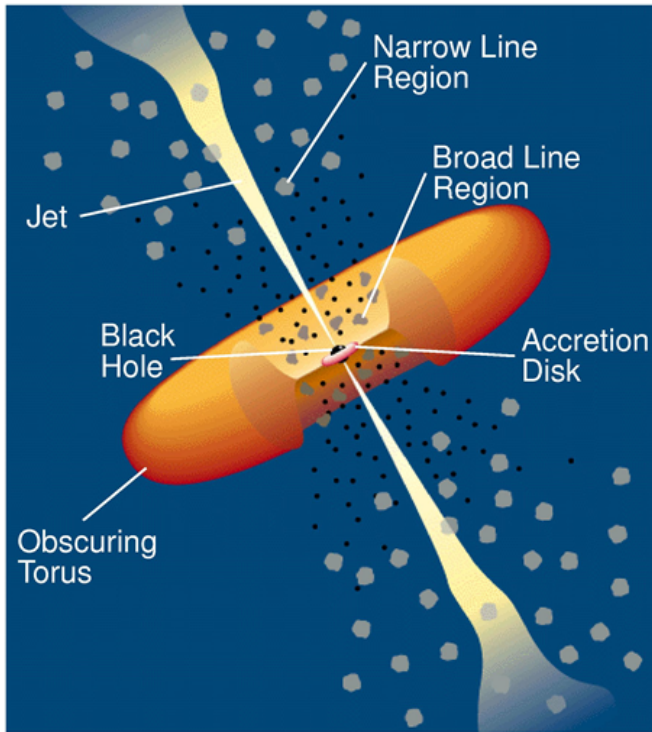


FIGURE 2.7: Model for the structure of an AGN, consisting of a dense, central emitting region and including jets of relativistic particles. The radius of the central black hole is $\sim 10^{-4}$ pc, while the jets can extend from 10^{-2} pc to kpc or even Mpc from the black hole. When the jets point towards the Earth, the source is known as a blazar. Figure from Holt *et al.* (1992).

2.4 Blazars

Blazars are a subclass of AGN, defined in particular by having their jets orientated along the line of sight towards the Earth (see Fig. 2.7). This fact makes blazars especially interesting, in that one can literally see straight down the beam of relativistic particles. Due to relativistic boosting, blazars are the brightest extragalactic sources in γ -rays. They are also characterized by their flux variability on time scales as short as minutes. This variability is strongly correlated across many energy bands.

Continuum emission from blazars is visible over the entire electromagnetic spectrum, from radio all the way through γ -rays. It is characterized by two broad peaks: one in the optical to X-ray band, and the other in MeV–GeV γ -rays (see Sect. 2.4.1). The continuum emission is strongly polarized, with a high variability on short time

scales. It is believed to be produced by non-thermal processes (synchrotron and inverse Compton; see Sect. 2.4.2), most likely coming from the blazar’s jets (Blandford and Rees, 1978).

While technically divided into two subclasses—flat spectrum radio quasars (FS-RQs) and BL Lacertae objects (BL Lacs)—some observations suggest that the distinction may not be so clear-cut (Ghisellini, 1999). Blazars detectable in TeV γ -rays are all BL Lacs, which lack the strong emission lines that distinguish them from FS-RQs. They get their name from BL Lacertae, the first object to be identified with these properties (Schmitt, 1968). They were usually discovered as extragalactic counterparts to strong radio sources. Distances of BL Lac sources are also very difficult to measure, due to their lack of spectral emission lines and the dominance of the nuclear emission over the emission of the host galaxy. BL Lac objects are also rare, which is consistent with the overall small probability that a source of this type has jets within 10° of the line of sight.

2.4.1 Spectral Energy Distributions

The Spectral Energy Distribution (SED) is usually plotted as the power emitted at each frequency per logarithmic energy interval (νF_ν) versus frequency (ν) on a log-log plot. Also called a “power spectrum”, it is an easy and compact way to view information about the frequency distribution of the emitted power across the entire electromagnetic spectrum in one plot.

As mentioned above, the SED of blazars exhibits two broad peaks (see Fig. 2.8).

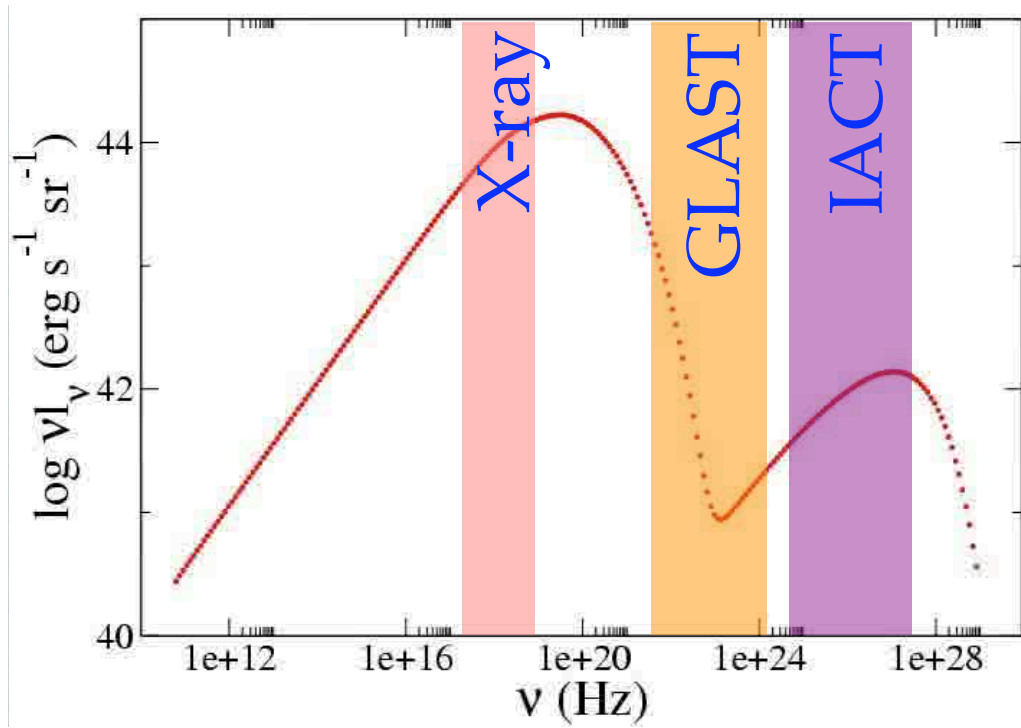


FIGURE 2.8: Typical Spectral Energy Distribution for AGN. There are two distinct peaks: one in the optical to X-ray band and the other in γ -rays. Colored bars represent the ranges over which various detection methods are used: X-ray, the upcoming GLAST satellite, and IACTs.

The first peak is usually in the optical-to-X-ray band, and almost universally attributed to synchrotron emission. The second peak occurs in the MeV-to-GeV band, but there is still much speculation as to what causes this emission. The most accepted mechanism for this second peak is inverse Compton emission. Various theories are discussed further in Section 2.4.2.

Since the flux from blazars varies considerably over time, their SEDs are also changing. When BL Lac sources get brighter, the emission peaks shift to higher energies. Using computer code to model blazar emission developed by Coppi (1992), we have seen the SED peaks evolve over time as the simulated blazar goes through flaring cycles. Such shifts have been also observed, for example, in Mrk 501 (Pian *et al.*, 1998).

2.4.2 Emission Models and Particle Acceleration

Several theories have been presented to account for the unique SED of blazars. More observations, in particular simultaneous observations at many different wavelengths, are necessary to break the model degeneracies and prove the mechanism by which particles are being excited to such extremely high energies.

Synchrotron Self-Compton

The Synchrotron Self-Compton (SSC) model was originally proposed by Ginzburg and Syrovatskii (1969). It has since been expanded for spherically homogeneous sources and evolved to incorporate relativistic jets. It is the simplest explanation for

blazar emission, in that the same population of relativistic electrons is responsible for both the X-ray and γ -ray peaks of the SED. The blazar's strong magnetic field accelerates the electrons in its jets which radiate synchrotron photons in the process, creating the lower SED peak. Inverse Compton processes then cause the upper peak, as these radiated photons collide with the same relativistically accelerated electrons that created them in the first place.

The most basic version of this scenario is the one-zone model, where emission comes from a shock front moving along the jet (Sikora and Madejski, 2001). This emission zone has a homogeneous magnetic field and proceeds relativistically down the jet, as electrons are constantly injected. The resulting spectrum of relativistic electrons can be described by a broken power law with a shoulder at the break frequency ν_B .

External Compton

Similar to SSC, External Compton (EC) models involve the same group of relativistic electrons radiating at lower energies by synchrotron radiation and at higher energies by inverse Compton (IC) radiation. However, the difference lies in the fact that the dominant seed photons for the IC emission come from outside the jet, and are not the same photons already being radiated through synchrotron processes. If the Compton scattering of ambient photons dominates the SSC emission, the energy density of the external radiation (measured in the jet frame) must exceed the energy density of the jet-produced synchrotron radiation. This requires the ambient photons

to be upscattered far from the source of synchrotron radiation ($\geq 10^{17}$ cm), so the newly created γ -rays are not lost to absorption by thermally emitted photons through pair production (Maraschi *et al.*, 1992).

Hadronic Models

This theory involves a population of protons with very high ($> 10^{17}$ eV) energy being created near the core of the AGN that travel down the jets. An intense proton flux near the jet base produces pions, both neutral and charged, which decay into γ -rays and electrons, respectively. These high energy electrons ($> 10^{16}$ eV) produce synchrotron radiation, which becomes a large portion of the γ -rays one observes. In this model, the X-rays, also produced through synchrotron radiation, come from a completely different population of electrons, those generated by the blazar's magnetic fields within the jets, as with the other two models.

Particle Acceleration

To produce any of the above-mentioned emission, the electrons/positrons may be accelerated by shocks in the jet (see review by Kirk and Duffy, 1999). For example, some (Sokolov and Marscher, 2005; Mimica *et al.*, 2004) suggest electrons are accelerated as they pass back and forth across the interface where two relativistic shock fronts collide. Alternatively, the particles may be accelerated by the central engine itself (Levinson, 2005; Katz, 2006; Krawczynski, 2006).

Many authors (Piner and Edwards, 2005; Henri and Saugé, 2006; Tavecchio, 2005)

have investigated the “ Γ problem”, wherein previous simulations of SSC emissions require a bulk Lorentz factor ~ 25 , an order of magnitude higher than what is observed through VLBA (Very Long Baseline Array) observations. Ghisellini *et al.* (2005) get around this need for high Lorentz factors by assuming there is a “layer and spine” structure to the AGN jets. Here, two concentric volumes move at different velocities, and therefore boost the emission seen by a factor of $\sim (\Gamma')^2 = \Gamma_{\text{spine}}^2 \Gamma_{\text{layer}}^2 (1 - \beta_{\text{spine}} \beta_{\text{layer}})^2$. The lower bulk Lorentz factors required by this model are more in line with the radio observations.

2.4.3 Markarian 421

For this study, we looked at the known TeV blazar Markarian (Mrk) 421. This source is a nearby ($z = 0.031$), high-energy peaked BL Lac object. It was the first extragalactic source detected in the TeV γ -ray band (Punch *et al.*, 1992). It is also visible in the Northern Hemisphere in spring, when the data were taken; the Crab Nebula, the standard candle for γ -ray sources, is only visible there in the fall.

Mrk 421 is a very active source, frequently prone to flaring, sometimes to brightness levels exceeding 10 times that of the Crab Nebula. Figure 2.9 shows its light curve in X-rays over several years. Mrk 421 shows loose correlation between the X-ray and TeV γ -ray bands, and has been the subject of many previous multiwavelength campaigns (*e.g.* Błażejowski *et al.*, 2005; Takahashi *et al.*, 2000). The history and volume of knowledge on Mrk 421 make it an appropriate candidate for testing the new VERITAS system.

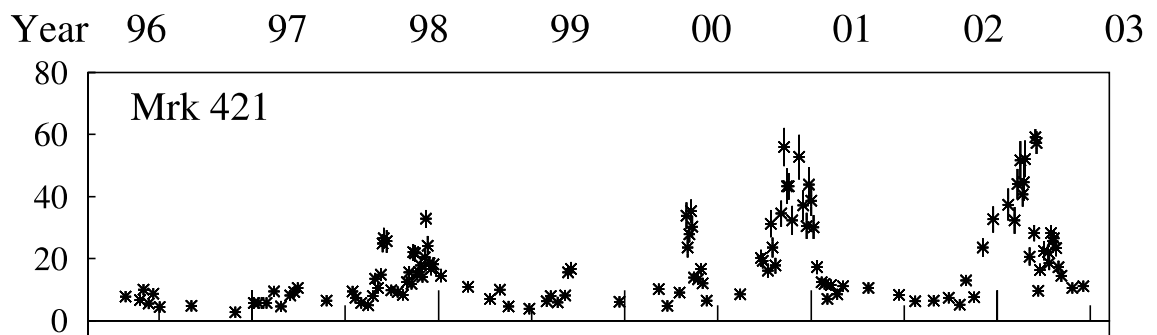


FIGURE 2.9: X-ray lightcurve of Mrk 421 showing extreme flux variability (flares) continuing over several years. The y-axis shows the 2 – 12 keV X-ray flux in mCrab units. Figure from Krawczynski *et al.* (2004).

Chapter 3

γ -ray Detection and VERITAS

3.1 γ -ray Propagation

Very High Energy (VHE) γ -rays ($\sim 10^{11} - 10^{13}$ eV) can come from both galactic and extragalactic sources. Unlike GeV and TeV cosmic rays, which are isotropized by galactic magnetic fields and bombard the Earth from all directions, VHE γ -rays come from particular objects in the sky. Within the galaxy, these sources are mainly pulsars, X-ray binary stars, or supernova remnants, while extragalactic sources are usually blazars. One can easily pinpoint where the γ -rays are coming from because they are uncharged and therefore their trajectories are unaltered by magnetic fields that exist throughout space.

3.1.1 Propagation Through Space

The strength of extragalactic γ -ray signals is reduced by interactions with the intergalactic infrared (IR) background in pair production processes

$$\gamma_{\text{VHE}} + \gamma_{\text{IR}} \rightarrow e^+ + e^-. \quad (3.1)$$

The absorption is strong for a wide range of VHE γ -rays above ~ 20 GeV, due to the broad peak in energy of the absorption cross section. The peak occurs when

$$E_{\text{VHE}} E_{\text{IR}}(1 - \cos \theta) \sim 2(m_e c^2)^2 = 0.52 \text{ (MeV)}^2, \quad (3.2)$$

where E_{VHE} and E_{IR} are the energies of the VHE γ -ray and IR photon respectively, and θ is the angle of the collision between the two particles. The mass of the electron and speed of light in a vacuum are represented by m_e and c . For 1 TeV photons, this peak occurs when colliding head-on with 0.5 eV photons. However, absorption is strong across a wide range of energies due to the spectral features of the extragalactic background (Gould and Schröder, 1967; Stecker *et al.*, 1992).

3.1.2 Air Showers in the Atmosphere

VHE γ -rays > 300 GeV require detector areas much larger than the $\sim 1 \text{ m}^2$ of typical space-borne telescopes in order to have any chance of detection. This is not technically or financially feasible. However, the Earth's atmosphere is completely opaque to such high energy particles. In order to detect γ -rays on the ground, one must use an indirect technique.

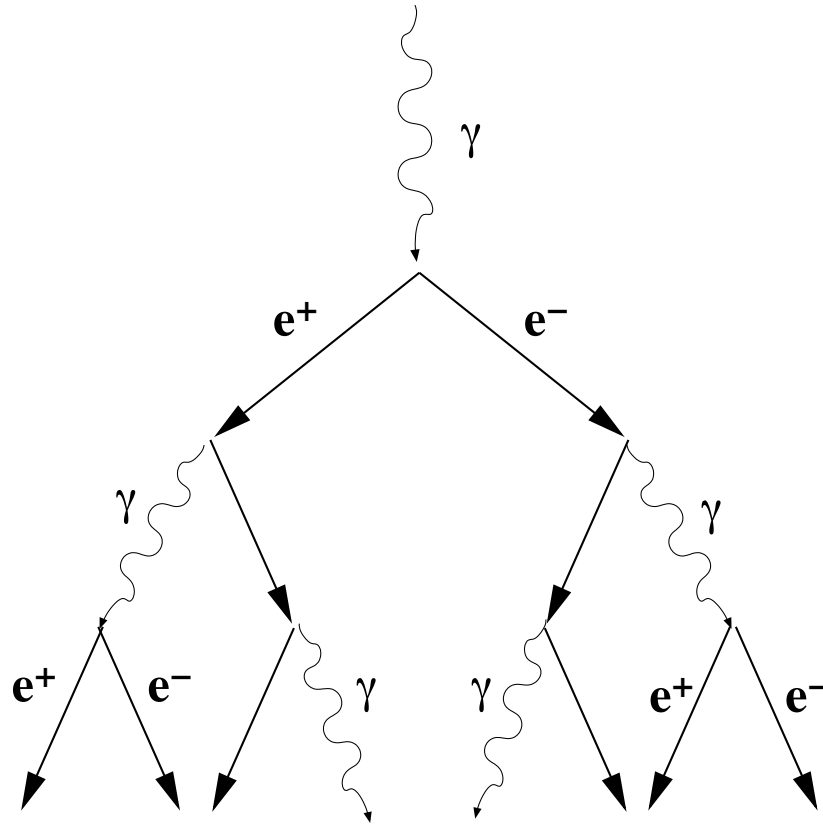


FIGURE 3.1: When a γ -ray interacts with the Earth's atmosphere, it pair-produces and initiates a cascading shower of electrons and positrons.

γ -ray Induced Showers

While impossible in free space due to energy and momentum conservation (Longair, 1992), γ -rays can pair-produce in the Earth's atmosphere, creating a cascading shower of electrons and positrons. These in turn produce another high-energy photon through bremsstrahlung, and the process repeats. Figure 3.1 schematically shows this cascading air shower. The result is a tightly collimated beam of Čerenkov light that eventually hits the ground.

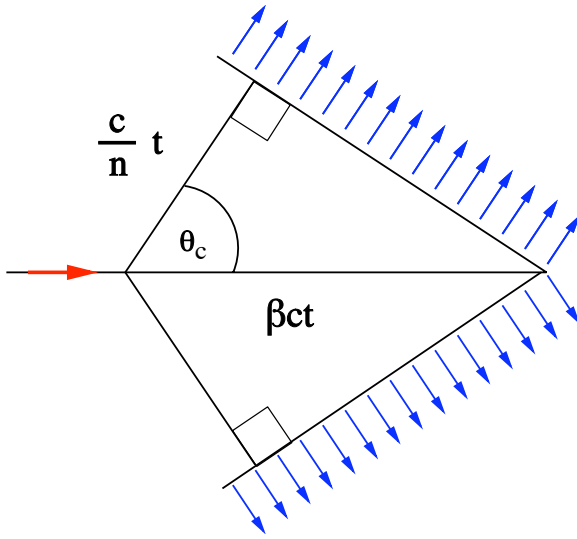


FIGURE 3.2: A particle traveling faster than the speed of light within a medium emits Čerenkov radiation at a specific angle given by Equation 3.3. Figure from <http://wikipedia.org>.

Čerenkov Radiation

When a particle travels through a medium at a velocity v faster than the speed of light in that medium, Čerenkov radiation is produced. A “shock front” is created and the particle radiates away energy. This results in a cone of Čerenkov light, which has a fixed angle θ_C with respect to the direction of particle motion. This angle is found by

$$\theta_C = \cos^{-1} \left(\frac{c_m t}{vt} \right) = \cos^{-1} \left(\frac{1}{\beta n} \right), \quad (3.3)$$

where c_m is the speed of light in the medium, and n is the index of refraction of that medium. As usual, $\beta = v/c$. Figure 3.2 depicts this scenario graphically.

To visualize how this radiation manifests itself, consider first a charged particle (like an electron) moving slowly through a medium. As it moves, the electron polarizes the nearby atoms, pushing the negative charges away from it (see Fig. 3.3a). The atoms relax back to their normal configuration after the electron has passed. Because the speed of the electron is relatively slow, this produces a symmetric disturbance in

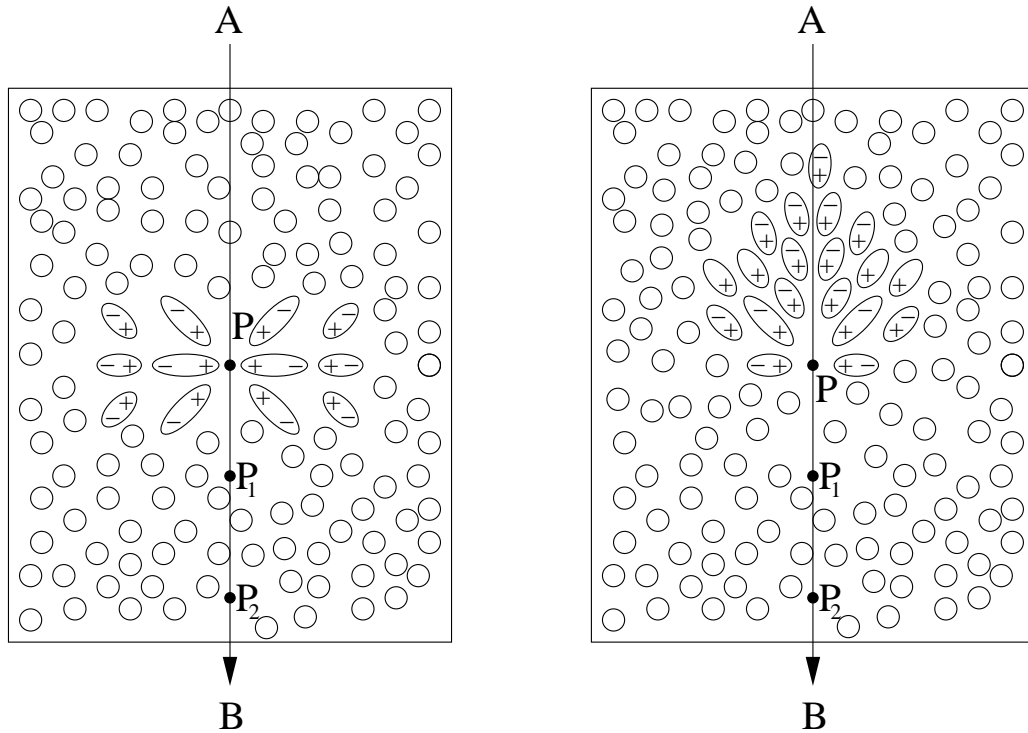


FIGURE 3.3: a) When a charged particle travels slowly through a medium, it polarizes the surrounding atoms. b) When the particle moves faster than the speed of light in the medium, there is a build-up of polarized charge just behind the moving particle. Figure adapted from Jelley (1958).

the medium, so no net polarization is observed.

However, if the charged particle is traveling faster than the speed of light in the medium, the polarization of nuclei is not symmetric (see Fig. 3.3b). The moving particle's charge is not propagated to the atoms of the medium until after the particle has passed, creating a build-up of positive charge just behind the moving electron. The transmittance of the electron's charge is sent out radially, and becomes cohesive along a wavefront at the angle θ_C from the direction it is traveling.

In air, the Čerenkov light reaching the ground has its peak emission in the UV/blue

portion of the spectrum. Telescopes that observe Čerenkov light are designed to have peak efficiency in this range.

Cosmic Ray Induced Showers

Cosmic rays are also constantly bombarding the Earth, and they too produce cascading showers in the atmosphere. This hadronic shower is much different than showers produced by a γ -ray, and includes both pions and muons. Hadronic showers are spread out over much larger areas than electromagnetic showers, owing to the momentum of the nucleons and quarks that give rise to large transverse velocities of the secondaries of hadronic interactions. Figure 3.4 shows schematically how a cosmic ray shower propagates through the atmosphere.

3.2 Detection Using an Imaging Atmospheric Čerenkov Telescope (IACT)

3.2.1 Atmospheric Technique

While the Earth's atmosphere has negative effects on most astronomical observations, with clouds and air currents distorting an astronomer's view of the heavens, it is a very necessary component for ground-based γ -ray observations. In fact, one is using the atmosphere as the detector medium to greatly increase the apparent collection area for such a telescope. The main drawback of using the atmosphere is

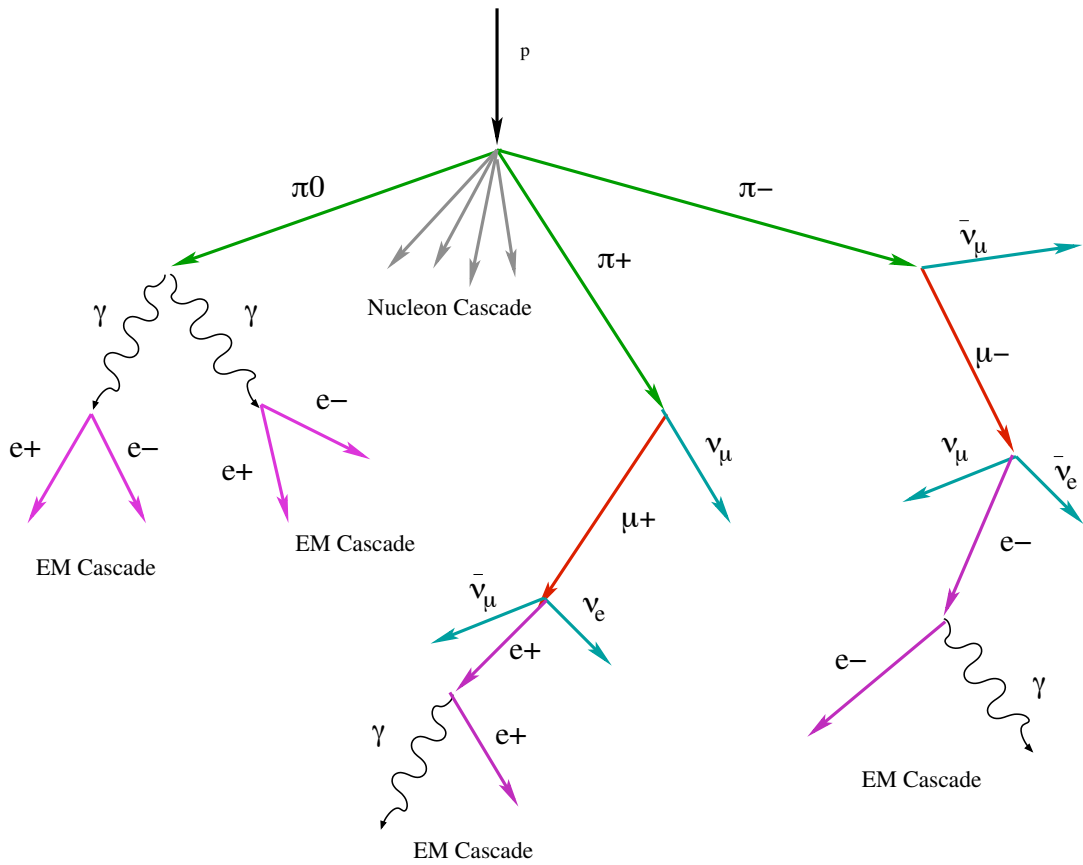


FIGURE 3.4: A cosmic ray induced air shower is much more extended than that of a γ -ray induced shower. Figure adapted from Jelley (1958).

its unpredictability. Its transparency affects the amount and angular distribution of Čerenkov light seen on the ground. Cloud layers can cause errors in the data including a higher detection threshold and inaccurate energy reconstruction. Hence, data must be taken on clear nights to be completely effective.

3.2.2 Imaging Čerenkov Radiation

When trying to observe a γ -ray source in the night sky, most of one's view is dominated by background noise and cosmic ray induced showers. Čerenkov light is only visible as a very weak (~ 50 photons m^{-2}), very short (~ 5 ns) pulse. While the intensity of the shower requires highly sensitive electronics to record, the pulse duration is what allows us to distinguish them from much of the night sky background.

Many methods have been utilized to better discriminate between the γ -ray signal and background. The biggest advancement in this field came with the development of technology to image the individual air showers. A camera with several individual PMT pixels can be used to determine both the size, shape, and intensity of the shower.

Due to the differences in the lateral spread of various air showers, they can lead to quite different looking images when seen from the ground. Figure 3.5 shows the difference between a γ -ray induced shower and a cosmic ray induced shower propagating through the Earth's atmosphere. γ -rays produce a very small, tight, round image on the camera, while hadronic showers produce a larger, broader shape. This difference is caused by the transverse momentum of nucleons and mesons present in cosmic ray showers, but not in γ -ray showers.

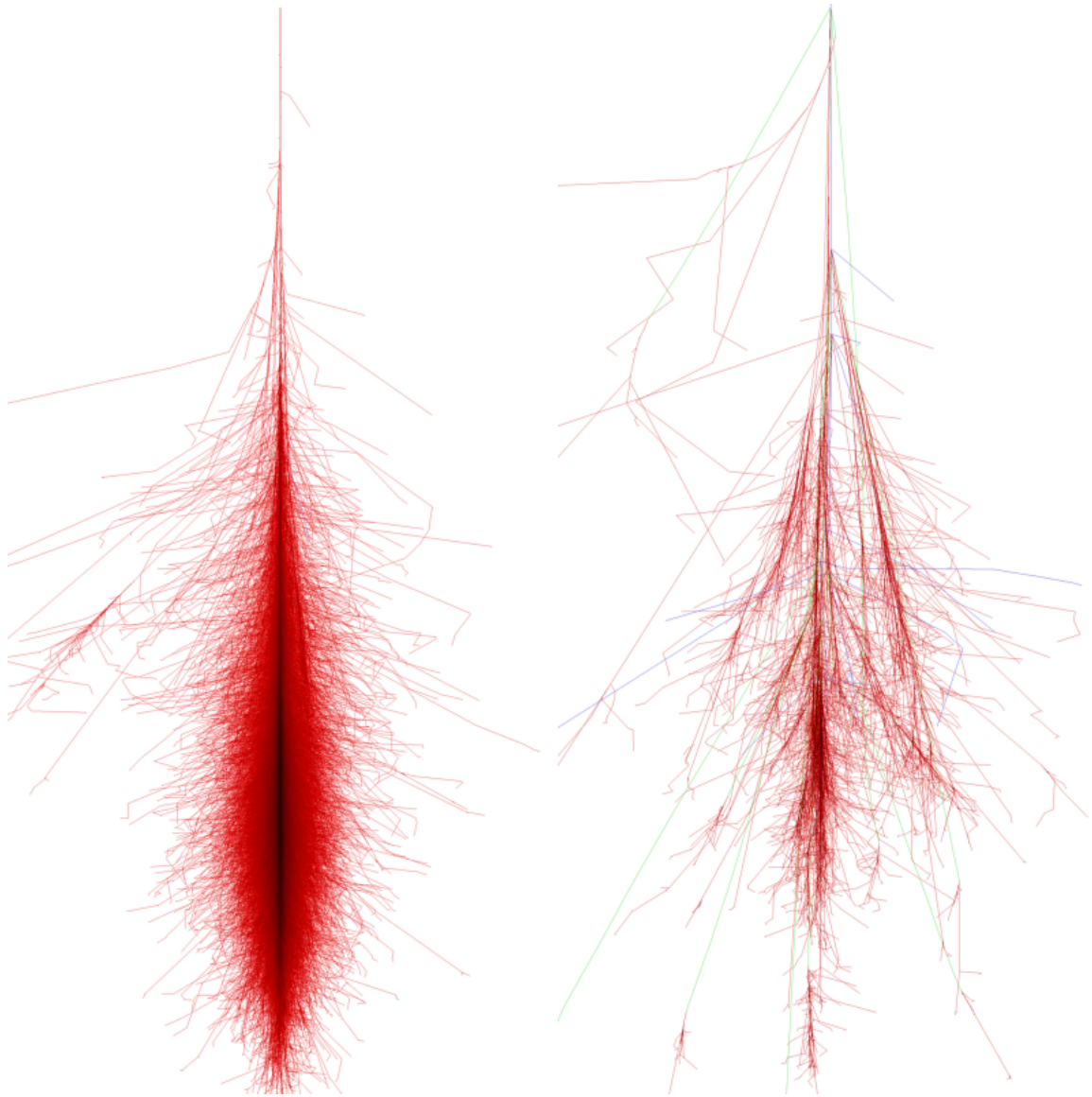


FIGURE 3.5: γ -ray induced air showers are very tight (left), while cosmic ray induced air showers are much broader. Both simulated showers were initiated by a particle of energy 100 GeV. Red lines represent electrons, positrons, and photons, and green and blue lines represent muons and hadrons respectively. Images courtesy of F. Schmidt, “CORSIKA Shower Images”, <http://www.ast.leeds.ac.uk/fs/showerimages.html>.

3.3 VERITAS: Very Energetic Radiation Imaging Telescope Array System

VERITAS, an array of four IACTs, is currently being built at the base camp of the Whipple Observatory in southern Arizona. It is designed as a successor to the previous Whipple 10 m telescope still in operation on Mt. Hopkins. Being a next-generation telescope, VERITAS improves over Whipple in sensitivity and background rejection (Weekes *et al.*, 2002).

3.3.1 Telescope Array

VERITAS is not just one, but several γ -ray telescopes that act together with a single trigger to greatly increase background rejection in the data. Originally planned as a grouping of seven identical telescopes, budget cuts required scaling back to just four.

Due to several factors outside of the control of the VERITAS Collaboration, the telescopes are initially being built on a temporary site at the Whipple Observatory base camp. This put many restrictions on the construction process, so that the optimal telescope configuration could not be obtained. Originally, the four telescope arrangement would have had one telescope in the center, and the other three equidistant from each other in a ring around the central telescope. The current configuration resembles a trapezoid (see Fig. 3.6).

The four telescope array is still being constructed and tested. Telescope 1 began

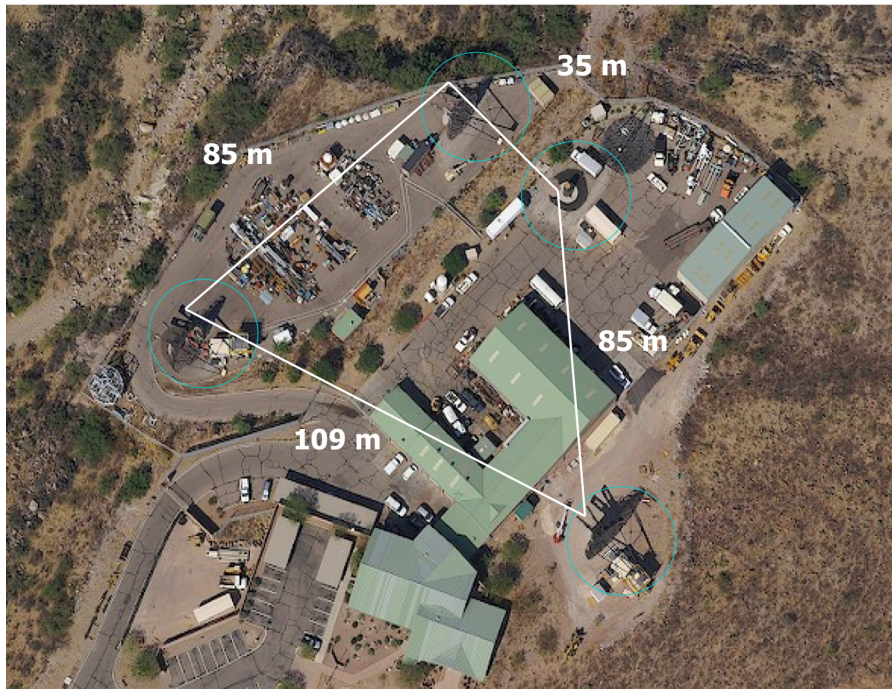


FIGURE 3.6: The current configuration of the four telescopes at the base camp of the Whipple Observatory is as shown. Distances and locations are not optimal due to construction restrictions around the existing structures.

operating as a prototype in 2004 with half of its PMTs and one third of its mirrors, and became fully operational in February, 2005 (Holder *et al.*, 2006). Telescope 2 saw first light in September, 2005. The first two telescopes operated separately for several months. The stereo trigger became active and the two telescopes operated together as one starting in March, 2006. Construction on the other two telescopes has progressed rather quickly, with Telescope 3 coming online in Fall, 2006, and Telescope 4 in January, 2007.

The four telescopes are identical. Each consists of a 12 m diameter support structure holding a segmented reflector made up of 350 hexagonal mirrors of total area $\sim 110\text{m}^2$ arranged in a Davies-Cotton configuration (Davies and Cotton, 1957). These focus incoming light onto the PMT camera, described in Section 3.3.2. Each telescope also has an electronics shed located right next to it. The sheds house the high voltage supplies and controls, the digitizing electronics that convert the camera signal so it can be processed, and the Level 2 trigger system. Figure 3.7 shows one of the VERITAS telescopes and its electronics shed.

These four telescopes send output to a central control hub, which combines the information from all telescopes into the final data stream. This is also the location from which nightly observations are commanded.

3.3.2 Camera

Mounted on each telescope is a camera consisting of 499 individual photo multiplier tubes (PMTs). Each acts as a single pixel to image the air showers. These

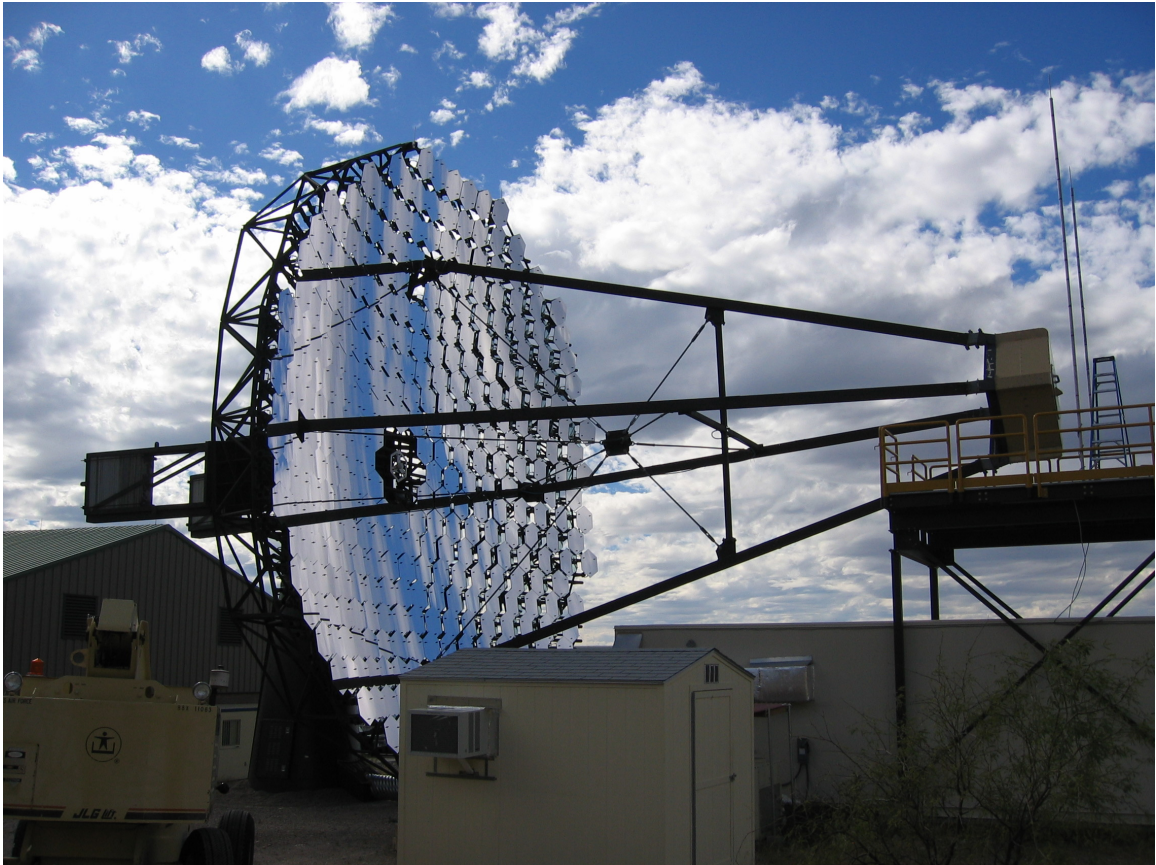


FIGURE 3.7: Pictured here is one of the four VERITAS telescopes in southern Arizona. The support arms extending off the 12 m optical structure hold the PMT camera. When not in use, the camera rests at an access platform directly above the electronics shed.

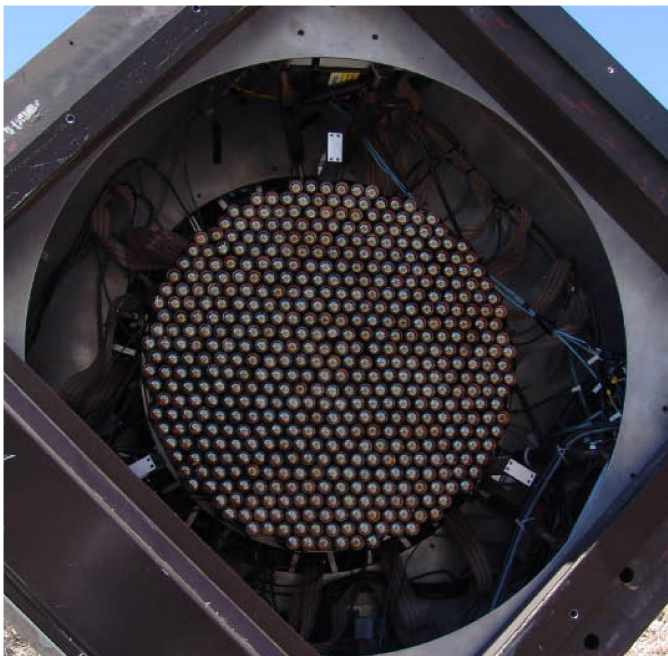


FIGURE 3.8: Each VERITAS camera consists of 499 PMT pixels that cover a 3.5° diameter field of view.

PMTs have their peak sensitivity in the blue/UV to maximize their sensitivity to Čerenkov light. The entire camera housing is 1.8 m square, large enough to allow for future expansion. The camera has a 3.5° diameter field of view. Figure 3.8 illustrates the PMT camera.

Light cones are used to maximize the photon collection efficiency, by focusing light onto the PMTs that would otherwise fall between them. They also shield the camera from stray background photons that do not originate from the source direction. A final design has now been chosen, but at the time the data for this thesis were taken, Telescopes 1 and 2 had light cones of different designs. This fact does not adversely affect this early stereo data.

The PMTs are operated with a gain of $\sim 2 \times 10^5$ electrons/photoelectron, necessary to detect single Čerenkov photons from the air showers. The high voltage system to bias the PMTs is housed in the control shed, next to each telescope.

The pre-amplifier attached to the base of each PMT is set up to allow constant monitoring of the PMT currents, as well as to inject charge pulses into the system for calibration and testing purposes. The current monitoring system allows for the auto- or manual suppression of individual channels with high currents owing to faulty electronics or a star in the field of view.

3.3.3 Trigger

In order for an event to register and be fully processed, it must pass a three-level triggering system. These correspond to triggering on the pixel, telescope, and array levels. The first level (L1) consists of fast constant fraction discriminators (CFDs) processing the analog PMT signals. The CFDs contain a programmable 6 ns delay to compensate for different PMT transit times and cable lengths.

From the CFDs, the L1 triggering signals are sent to the Level 2 (L2) trigger. This is a topological system that uses a programmable look-up table of patterns to determine if a given number of neighboring pixels have triggered. Currently, the coincidence condition requires three neighboring pixels to trigger within 10 ns.

Each telescope L2 trigger is then sent to the Level 3 (L3) trigger. For the two-telescope data used for this thesis, the L3 trigger was set to require both telescopes to record an event within a 100 ns coincidence window. This relatively wide window ensured the array would trigger even if there were some problems with timing between the two telescopes. If an event passes the L3 trigger, it is tagged with the GPS time and the event is then read out from the data acquisition system.

3.3.4 Data Acquisition

One of the technical strengths of VERITAS is the data acquisition system. At its heart is the 500 MHz flash ADC (FADC) system (Buckley, 1999). The signal from each PMT is digitized in 2 ns bins and stored with a total lookback memory of 32 μ s. The FADC system allows for continuous data-taking while the triggering system determines the validity of events, as well as the possibility for advanced timing studies of the individual showers.

The FADC boards record data until they receive a signal from the L3 trigger that an event has occurred. The data acquisition pauses until the relevant data are read out, then continues digitizing data until the next event.

One important feature of the FADC boards is their ability to switch between a high and low gain signal path. If a pulse comes through the FADC that exceeds the dynamic range of the high gain path, a high/low gain switch is flipped, and the signal from the low gain path is digitized. This allows the system to easily handle a wide variety of pulse heights with an 8-bit digitizer.

Chapter 4

Mrk 421 Data Analysis

4.1 Event Reconstruction

The images captured by the VERITAS cameras result from thousands of bremsstrahlung and pair-production interactions in the atmosphere. To gain information about the incident γ -ray, one must “reconstruct” an event and determine a number of parameters characterizing the air shower. The important result of the event reconstruction is the location and orientation of the air shower axis, which points back to the arrival direction of the primary γ -ray. Furthermore, the event reconstruction gives information about the nature of the primary particle, photon or hadron. Last but not least, we want to know the energy of the primary γ -ray. In the following, we describe the methods used in this thesis.

4.1.1 Hillas Parameterization

Čerenkov light reaching the telescopes' cameras is captured by the individual pixel PMTs. The resulting image can then be parameterized. Calculations of the first, second, and third moments of the image distribution are used to fit an ellipse to each event's image. This process is described more fully in Reynolds *et al.* (1993).

The resulting parameters describing the size (*length* and *width*), placement (*distance* and *miss*) and orientation (α) of the ellipse are known as Hillas parameters. Figure 4.1 shows these parameters in detail. Additional parameters used include *size*, the total number of digital counts in the image. This is directly related to the shower's energy.

One great advantage to analyzing images this way is that air showers caused by different particles look dramatically different in the camera. Since more than 99% of the events recorded come from cosmic ray showers, it is beneficial to be able to distinguish them from the more important γ -rays in the data. γ -ray initiated showers create an ellipse with its major axis pointing towards the camera's center. The large transverse momentum associated with the strong hadronic interactions cause cosmic ray showers to create a more rounded concentration of light. Muons, on the other hand, produce a large ring, resulting from the initial interaction occurring relatively close to the camera itself. Any other odd shape is just background noise. Figure 4.2 shows examples of these different types of events for one VERITAS camera. These differences in shape allow for more efficient rejection of background events based on

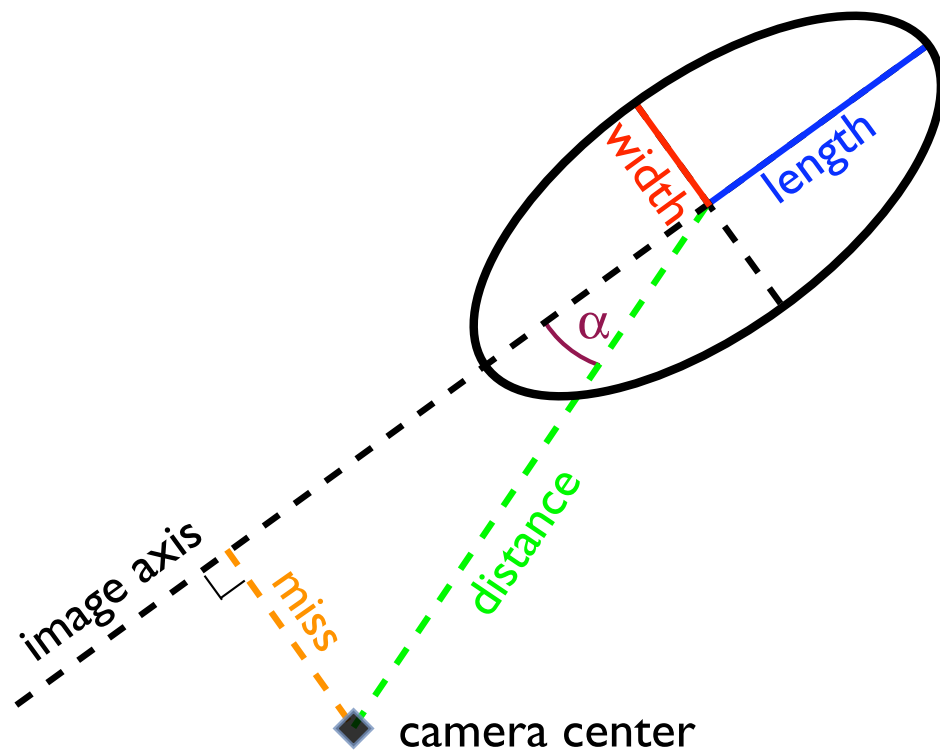


FIGURE 4.1: Illustration of the various Hillas parameters.

values for the different Hillas parameters.

4.1.2 Stereo Reconstruction

After an event has been parameterized for each telescope, the images are combined into one stereo event. This “stereo reconstruction” involves using the intersection of the major axes of the ellipses of all telescopes to find the shower direction and axis (see Fig. 4.3). From this reconstruction, we gain a new parameter, θ^2 , the square of the angular distance of the shower core from the center of the camera. Cutting on this distance is the most reliable way to discard the maximum number of background events while keeping as much signal as possible.

An important parameter we derive from the analyzed data is the mean scaled width ($MSCW$), which also proves to be very useful in separating hadronic from γ -ray showers. $MSCW$ —and its similarly derived cousin, mean scaled length ($MSCL$)—utilize the fact that hadronic showers appear significantly “wider” in an IACT camera, due to the transverse momentum associated with the nucleons and mesons as their interactions cascade through the atmosphere. Using Monte Carlo simulations (see Sect. 4.5), we create a look-up table of expected median $width$ values (w_m) and the 90%-widths of the distributions (w_{90}) as functions of both $size$ and r , the distance of the telescope from the shower axis. From these tables, we calculate a “normalized width”

$$MSCW = \frac{1}{N_{\text{trig}}} \times \left[\sum_i^{N_{\text{trig}}} \frac{width_i - w_m(r_i, size_i)}{w_{90}(r_i, size_i)} \right], \quad (4.1)$$

summing over all N_{trig} telescopes with a trigger, where $width_i$ and $size_i$ are the $width$

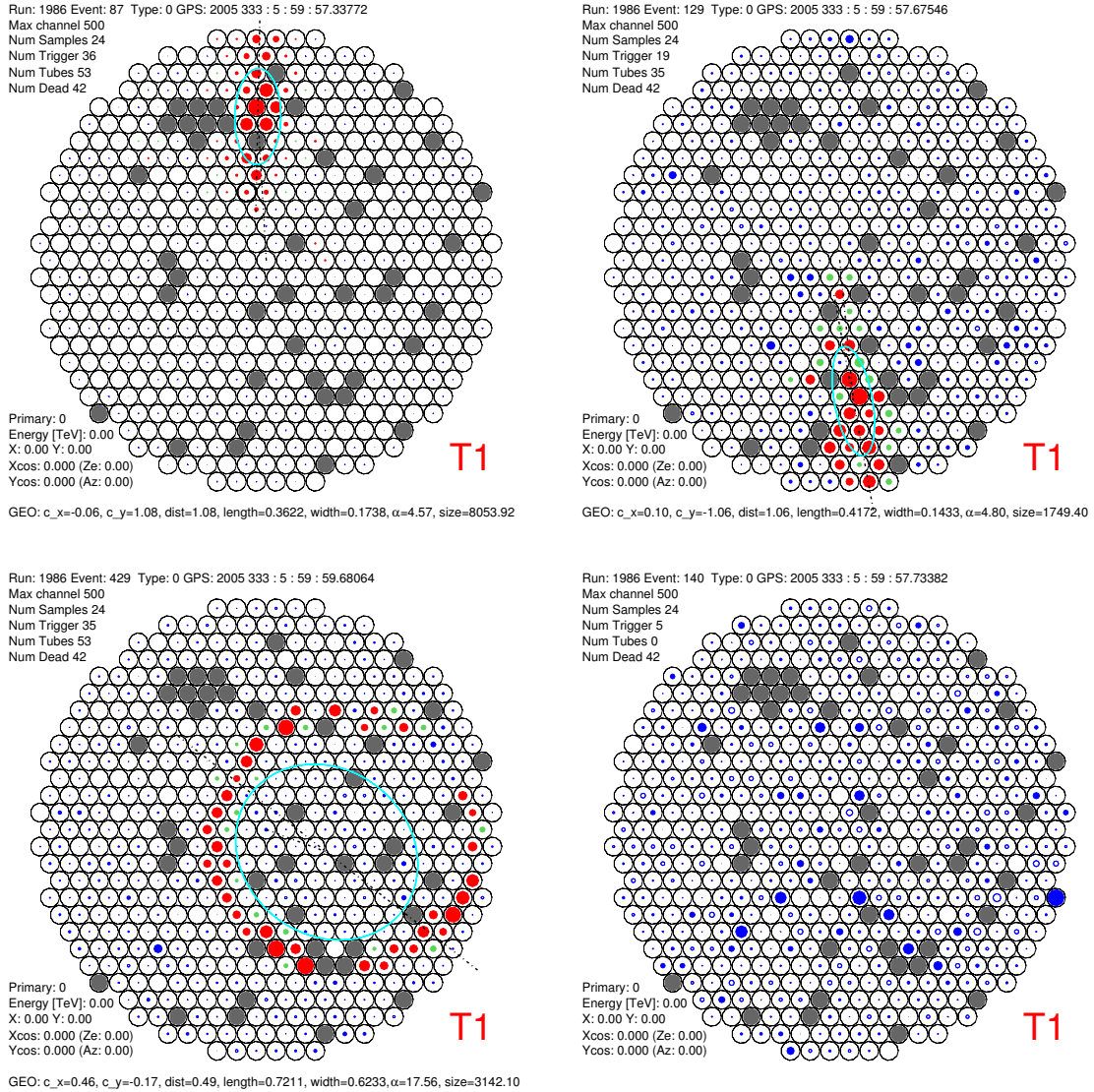


FIGURE 4.2: Examples of actual sky shower images by one VERITAS camera: a γ -ray (top left), a hadron (top right), a muon (bottom left), and a noise event (bottom right). Pixels in grey are marked as “broken” in the camera and are not being read out, the result of poor connections and cabling, among other things. Fixing these pixels is one of the many tasks yet to be done to bring VERITAS into full operational mode.

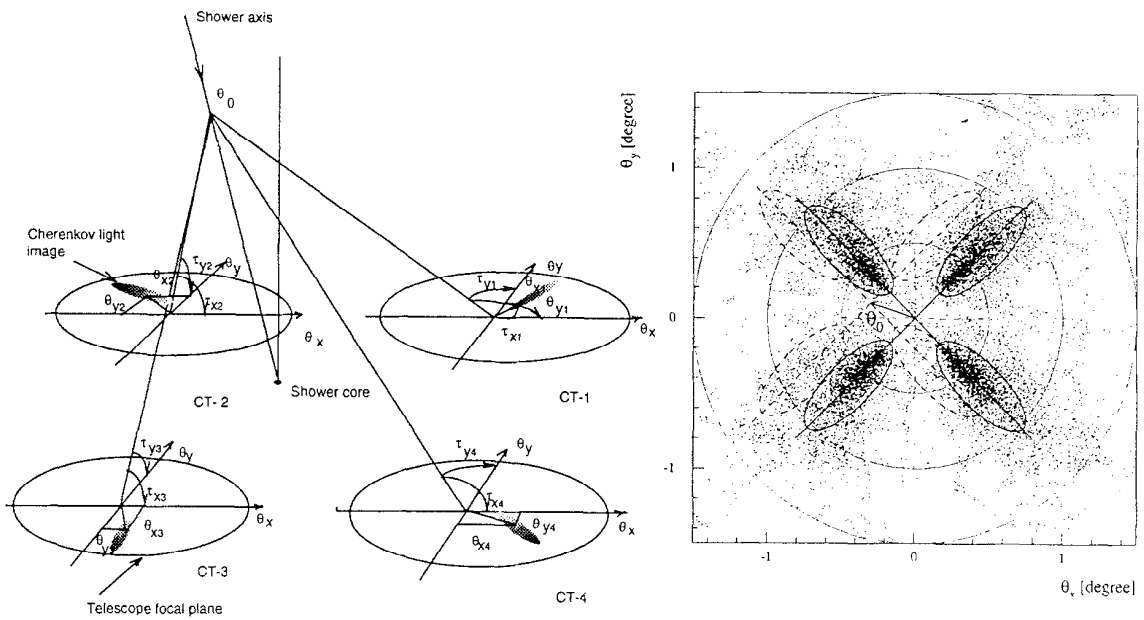


FIGURE 4.3: Reconstructing the arrival direction of stereo showers. The shower impact point and the resulting images in each camera are shown on the left. The images from each camera are then superimposed (right). Solid ellipses portray a shower vertically incident to the telescopes; dotted ellipses correspond to a shower inclined by an angle θ_0 . Figure from Aharonian *et al.* (1997).

and *size* values for the image in the i th telescope, and r_i is that telescope's distance from the shower axis. *MSCW* is more useful than simply looking at *width* distributions for multiple telescopes, because it takes into account the shower's location relative to each of the telescopes, weighting the individual width distributions by the appropriate factor to calculate this normalized parameter.

Monte Carlo simulations are also useful to help reconstruct the energy of the γ -ray shower. We can create a look-up table of energies using the median and 90%-width values of the logarithm of the *size* parameters as a function of the primary shower's energy E . To reconstruct the energy of a shower, we simply invert the table. The shower's reconstructed energy is determined by averaging the energies obtained from each telescope with a trigger.

4.1.3 Analysis Tools

As VERITAS is still fairly new, there is yet no fully established method for data analysis. The official analysis package, *VEGAS* (VERITAS Experiment Gamma-ray Analysis Suite), is still in development and far from fully optimized or simple to use. Using *VEGAS* will soon become standard, but for this work we have relied on other packages that have been more thoroughly tested and are known to produce reliable results for γ -ray data.

To analyze the data, we have used the University of Leeds' *eventdisplay* and *mscw.energy* packages. These packages handle the main aspects of data reduction and analysis for a stereo system. The programs' output files can be imported into

ROOT for further analysis and plotting. The *eventdisplay* package also contains extensive display tools to view individual events on each camera, as well as individual FADC traces and other timing information.

For each night of data, a calibration must be done to correct for minor fluctuations in weather and telescope electronics. This is done through the use of a “laser run”. At the start of each night, a short run is taken where a laser is flashed at the PMT camera. The constant flux of these pulses is used to adjust the analysis program to the subtle differences in how each pixel detects the light intensity as well as timing.

After the calibration is done, each run for the night may be analyzed and parameterized. Hillas parameters are calculated for each telescope, and the stereo data is reconstructed to find the shower axis (see Sect. 4.1.1). Afterwards, the mean scaled width, mean scaled length, and energy are reconstructed.

4.2 Data Cuts and Significances

After the events are fully parameterized, cuts are applied to separate actual γ -rays from background events. Once VERITAS is brought fully online and more data have been acquired and analyzed, a standard set of cuts will become available. Since the standard cuts have yet to be established, we present preliminary work to establish cuts in both $MSCW$ and θ^2 , discussed in Section 4.6.

To determine the excess, one separates the events passing all data cuts into two categories: events from the signal or “ON” region, and events from a comparison

background or “OFF” region (see Sect. 4.4.1 for more on these regions). The number of events in these regions (N_{ON} and N_{OFF} respectively) can be used to calculate the γ -ray rate as well as its associated error:

$$r \pm \Delta r = \frac{N_{\text{ON}} - N_{\text{OFF}}}{\text{time}} \pm \frac{\sqrt{N_{\text{ON}} + N_{\text{OFF}}}}{\text{time}}. \quad (4.2)$$

A large positive excess of at least the 5σ level means the source has been detected.

This statistical significance is calculated as follows:

$$\sigma = \frac{r}{\Delta r} = \frac{N_{\text{ON}} - N_{\text{OFF}}}{\sqrt{N_{\text{ON}} + N_{\text{OFF}}}}. \quad (4.3)$$

4.3 Spectral Reconstruction

Spectral reconstruction of the Mrk 421 data was performed using the forward-folding method of Henric Krawczynski, described fully in Rebillot *et al.* (2006). It has been incorporated into the program *wufit*, part of Washington University’s own data analysis package, *wuparam*.

Energies are reconstructed for every event in both the ON and OFF regions, as well as for all Monte Carlo simulated events, as described above. The energies are histogrammed, and the OFF energy histogram is subtracted from the ON energies to yield the energy excess. The energy spectrum can then be fitted to the excess histogram, with help from the Monte Carlo simulated energy histogram, using the forward-folding approach (see, *e.g.*, Fenimore *et al.*, 1982).

The data are fit using a power-law model:

$$\frac{dN_\gamma}{dE} = N_0 \cdot (E/1 \text{ TeV})^{-\Gamma} \quad (4.4)$$

where N_0 is the flux normalization at 1 TeV and Γ is the photon index. For each trial parameter set (N_0 and Γ), an energy histogram is filled weighing the Monte Carlo events so as to mimic the model of Equation 4.4. Both parameters are then varied in the user-defined parameter space to minimize the χ^2 difference between the data and Monte Carlo histograms. The values of N_0 and Γ with the best fit, along with associated errors, give the source’s energy spectrum.

4.4 Mrk 421 Data from April–May 2006

Data taken during the dark run from April–May 2006 were the first set of true stereo data from the VERITAS telescopes. The data on the known blazar Mrk 421 contain a large number of γ -ray events and can be used for calibration purposes.

4.4.1 Observation Modes

There are a variety of modes in which VERITAS data can be taken. ON–OFF pairs were the standard method in the past, however they require an extremely clear sky to be useful because passing clouds will affect the source and background regions differently. This method can seem wasteful in that half of the observation time is used to examine blank fields in the sky. Tracking runs are useful because they require less time than ON–OFF pairs and can still be effective in less than perfect weather,

due to clouds altering both ON and OFF regions in the same way. The method is somewhat problematic as the sensitivity is not uniform over the entire field of view of the telescopes. We are also trying out an attractive method, Wobble mode, which combines the benefits of both Tracking and ON–OFF pairs into a single method which minimizes both the observation time and the systematic uncertainties.

ON–OFF Pairs

Frequently used on the Whipple 10 m telescope, ON–OFF pairs are good for getting high quality data, but are only accurate and effective on cloudless nights. First, a 28-minute run is taken with the source at the center of the camera. Then, a second OFF run is taken, offset 30 minutes in Right Ascension, and taken 30 minutes after the ON run. This second run sweeps across the exact same portion of the sky as the ON run for more accurate background subtraction that is not affected by the systematics of the telescope itself. Many data from this dark run were taken as ON–OFF pairs, but have been processed as tracking to simplify the analysis procedure.

Tracking Runs

Tracking runs require less time and can be useful in less perfect weather. These runs simply keep the source at the center of the camera at all times. For background subtraction, an OFF region is chosen farther from the center of the camera, so it is not be affected by the source itself. Figure 4.4a depicts visually the ON and OFF regions of the field of view for a Tracking run. The ON region is a circle with given

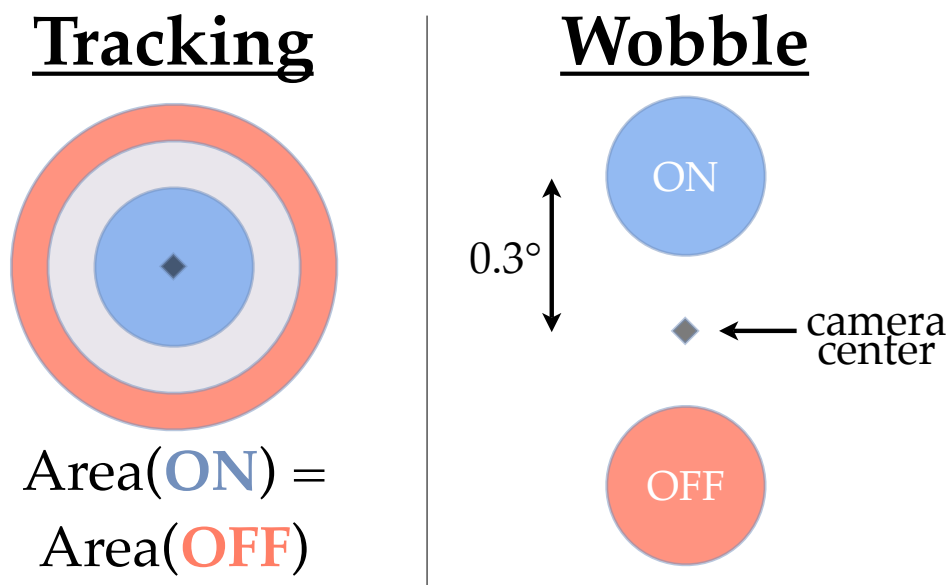


FIGURE 4.4: The different observation modes have different ways in which background is subtracted from OFF regions. For tracking runs (left), the OFF region is an annulus with the same area as the source region, spaced a bit outside of the source region. For wobble runs (right), the OFF region is the same shape and size as the ON region, but offset on the other side of the telescope’s center.

radius at the center of the camera. The OFF region is then an annulus with the same area as the ON region, centered on the source, with a buffer zone of space between the two, so the source does not contaminate the background region.

This method is less reliable than doing ON–OFF pairs for several reasons. Because the OFF region is farther from the camera’s center, the number of events in this region may be less than what one would expect. This could be due, in part, to these events not triggering both telescopes. Also, because the centroids would occur at larger distances from the camera center, the images could be more spread out, introducing a bias in the width distributions. In contrast to ON–OFF pairs, passing clouds would

effect both the ON and OFF regions in the same way, making this behavior a tradeoff between the two methods.

Wobble Runs

Wobble runs have proved an effective observation mode for stereo Čerenkov telescope systems such as HEGRA (Daum *et al.*, 1997) and H.E.S.S. (Aharonian *et al.*, 2005c) as the detection sensitivity is rather uniform over the central part of the field of view. VERITAS is starting to use them as well. This method combines the effectiveness of ON–OFF pairs with the convenience and speed of a Tracking run. Wobbling involves offsetting the source by a given amount in the field of view. The offsets are in varying directions (usually opposite) in order to cancel out systematic inhomogeneities in the camera itself. Figure 4.4b depicts visually the ON and OFF regions for a wobble run. Both regions are the same size and shape, offset on opposite sides of the camera, with the ON region centered on the source. There is space between the two regions, again, to prevent the source from influencing the background region. This method is not as valuable for single telescopes, because their detection rate is more strongly affected by stars in the field of view and faulty pixels.

4.4.2 Final Data Set

Not every data run that was taken is useable. Various problems exist with the data as this new experiment is slowly brought completely online. Issues range from imperfect weather, to rate spikes due to nearby car headlights, to issues with the

hardware and software.

Ground-based γ -ray telescopes usually operate at around a 10% duty cycle. The solar and lunar cycles (especially towards summer, as the number of daylight hours increases) as well as the weather and Arizona’s monsoons severely limit the amount of time it is possible to operate the telescopes.

After disregarding all runs with rate spikes, as well as those with irreparable problems, we were left with the final data set that was used to complete the following analysis. A total of 32 runs over nine separate days, corresponding to 14.3 hrs of observations, were used. Table 4.1 lists the data and laser calibration runs used.

TABLE 4.1: Run information that makes up the final data set from which this thesis is based. Data runs are all of the source Mrk 421 during the April–May 2006 dark run. Associated laser calibration runs are also listed. ON–OFF pairs are denoted as “ON/OFF”, Tracking runs as “Trk”. Wobble runs denoted as the offset distance and direction: “0.3N” implies the source is offset 0.3° to the North of the camera’s center.

Date	Run Number	OFF Run	Laser Run	Run Type	Elevation
2006-04-20	30336	—	—	laser	—
2006-04-20	30328	30329	30336	ON/OFF	83
2006-04-20	30330	30332	30336	ON/OFF	78
2006-04-20	30333	—	30336	Trk	67
2006-04-21	30358	30359	30336	ON/OFF	82
2006-04-21	30365	—	30336	Trk	69
2006-04-23	30404	—	—	laser	—
2006-04-23	30394	30395	30404	ON/OFF	77
2006-04-23	30396	30397	30404	ON/OFF	83
2006-04-23	30398	30399	30404	ON/OFF	75
2006-04-23	30400	30401	30404	ON/OFF	64
2006-04-24	30424	—	30404	Trk	83
2006-04-26	30476	30477	30404	ON/OFF	72
2006-04-26	30478	30479	30404	ON/OFF	62
2006-04-26	30480	—	30404	0.3E	50

Continued on next page. . .

TABLE 4.1 – Continued

Date	Run Number	OFF Run	Laser Run	Run Type	Elevation
2006-04-27	30504	—	—	laser	—
2006-04-27	30492	—	30504	0.3E	82
2006-04-27	30493	—	30504	0.3W	77
2006-04-27	30494	—	30504	0.3N	70
2006-04-27	30495	—	30504	0.3S	64
2006-04-27	30496	—	30504	0.3N	58
2006-04-27	30497	—	30504	0.3S	52
2006-04-29	30540	—	—	laser	—
2006-04-29	30533	—	30540	Trk	83
2006-04-29	30534	—	30540	Trk	81
2006-04-29	30536	—	30540	Trk	69
2006-04-29	30537	—	30540	Trk	63
2006-04-30	30564	—	—	laser	—
2006-04-30	30553	—	30564	Trk	78
2006-04-30	30554	—	30564	Trk	73
2006-04-30	30555	—	30564	Trk	68
2006-04-30	30556	—	30564	Trk	62
2006-04-30	30557	—	30564	Trk	56
2006-04-30	30559	—	30564	Trk	45
2006-04-30	30560	—	30564	Trk	41
2006-05-01	30575	—	—	laser	—
2006-05-01	30570	—	30575	Trk	65
2006-05-01	30572	—	30575	0.3S	52

4.5 Comparison of Experimental and Monte Carlo Data

In order for the energy spectrum or other results relying on Monte Carlo simulations to be reliable, one must first prove that the simulations accurately describe

the system they are intended to model. By comparing the distributions of the various parameters in the simulated data set to those from experimental data, one can test how well the Monte Carlo simulations are performing and how accurate results obtained with them will be. Here we use Mrk 421 as a strong “test beam” of γ -rays.

For this study, Monte Carlo simulations were done on vertically incident γ -rays with energies from 30 GeV to 50 TeV. A total of 2,615,000 events with a Crab-like differential spectral index of $\Gamma = 2.5$ were simulated. The showers were simulated over an area of radius 350 m. While γ -rays behave differently when the telescope is pointed at lower elevations than at higher ones (Kosack *et al.*, 2004), the (generally) low zenith angles of the runs used in this study did not require simulating different zenith angles. Simulations were generated with the Grinnell-ISU (GrISU) package¹ that uses the KASCADE air shower simulation code of Kertzman and Sembroski (1994), followed by the simulation of the Čerenkov light emitted by the air shower and the telescope detector’s response to that light.

Figure 4.5 shows several plots of the various Hillas parameters, comparing the Monte Carlo simulations with real data. Overall, it can be seen that the two agree very well, showing these simulations accurately model the air showers and the detector response. For both simulated and experimental data, only showers within a radius of 200 m from the telescopes were used. Whereas most parameter distributions agree very well over the entire range, the *size* distributions disagree at smaller *size* values. This fact can be linked to both the steep spectrum of Mrk 421 and the difficulty in

¹ See <http://www.physics.utah.edu/gammaray/GrISU>.

4.5 Comparison of Experimental and Monte Carlo Data

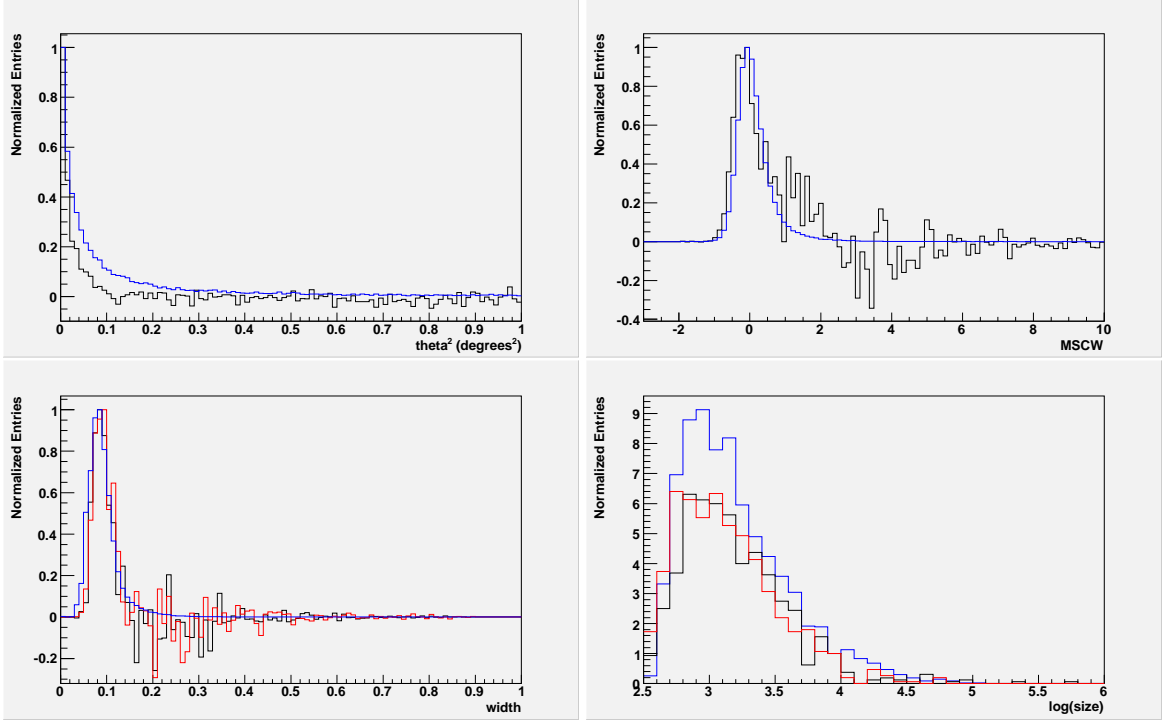


FIGURE 4.5: Several plots showing both Monte Carlo simulated events (blue) as well as real data events. The top two plots show array-level parameters, θ^2 and $MSCW$, with the array data plotted in black. The bottom two plots show telescope-level data, $width$ and $size$, with T1 plotted in black and T2 in red.

modeling the trigger accurately. A cut of $size > 1000$ would eliminate this difference between the two curves. We have also used these Monte Carlo simulations to estimate the energy thresholds, angular, core, and energy resolutions of the two-telescope VERITAS experiment.

The energy threshold is calculated from the energy distributions of the Monte Carlo simulations. Figure 4.6 shows these distributions both before and after the optimized cuts discussed in Section 4.6. Where these histograms peak is commonly referred to as the energy threshold. It is measured as 165 GeV before cuts, and 220 GeV after cuts.

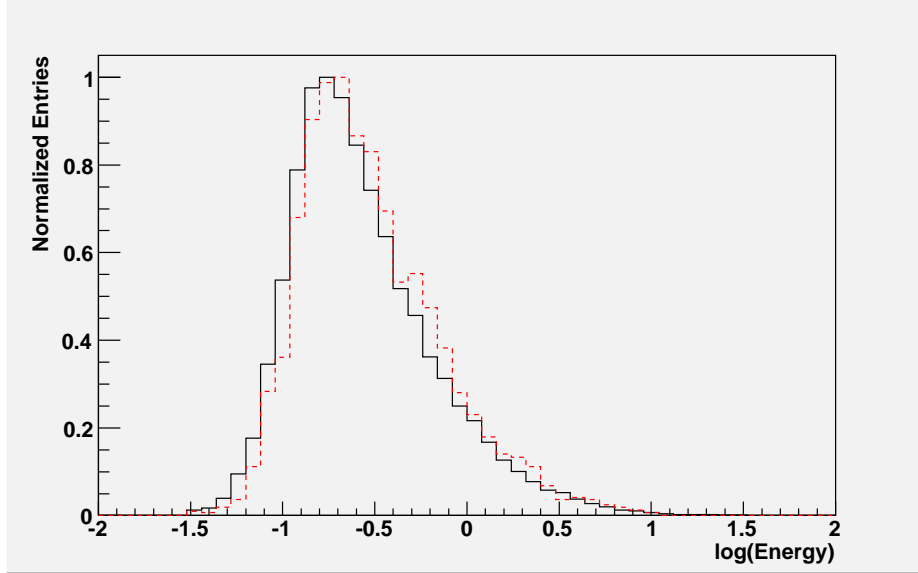


FIGURE 4.6: Plot showing the (log) energy distributions of the Monte Carlo simulations for a Crab-like spectrum of $E^{-2.5}$, both before (black) and after (red) cuts. The energy bin with the most entries is the energy threshold: 165 GeV before cuts and 220 GeV after cuts.

One can also plot how the angular resolution of the simulations vary with energy.

For a given energy bin, the angular resolution is defined as the angular distance θ below which occur 63% of the events. This resolution is plotted in Figure 4.7, and Table 4.2 lists the values as well as the energy bins used. For the entire energy range, the angular resolution is 0.29° in simulations.

Similarly, the core resolution can be plotted. This measures the difference in position of the reconstructed shower core position from the actual position:

$$\mathfrak{R}_{\text{core}} = \sqrt{(x_{\text{core}} - MCx_{\text{core}})^2 + (y_{\text{core}} - MCy_{\text{core}})^2}, \quad (4.5)$$

where $(MCx_{\text{core}}, MCy_{\text{core}})$ is the true shower core and $(x_{\text{core}}, y_{\text{core}})$ is the reconstructed core. *eventdisplay* can calculate the reconstructed core in two different ways:

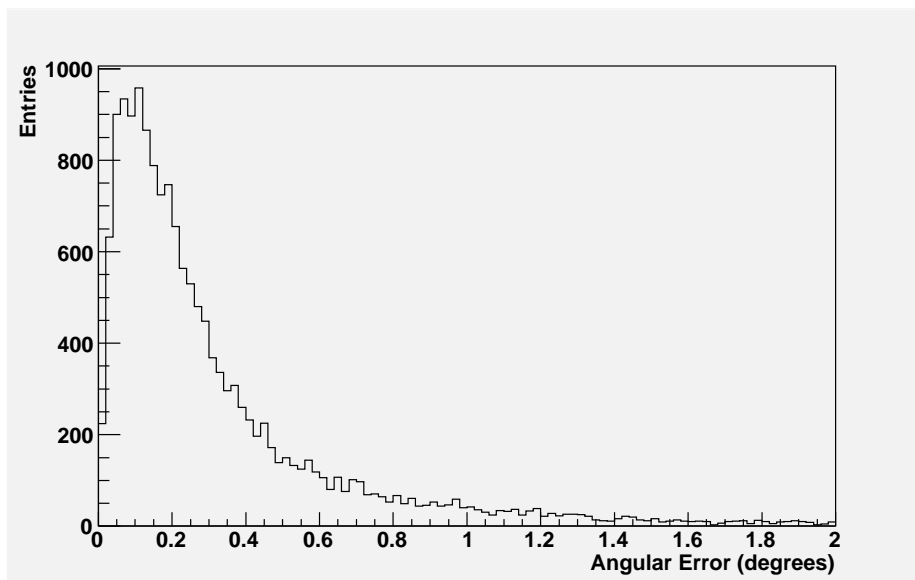


FIGURE 4.7: Plot showing the angular resolution of the Monte Carlo simulations. For all energies, the angle below which 63% of events occur is 0.29° .

TABLE 4.2: Angular Resolution for the Monte Carlo simulations over different energy ranges.

Energy Bin	Angular Resolution
< 100 GeV	0.37
100 GeV – 800 GeV	0.29
800 GeV – 2 TeV	0.22
2 TeV – 10 TeV	0.22
all energies	0.29

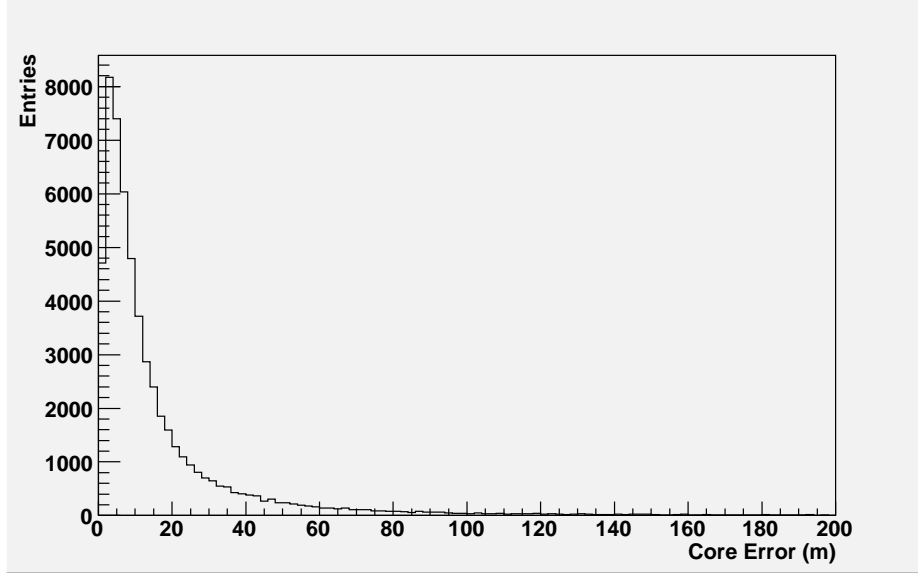


FIGURE 4.8: Plot showing the core resolution of the Monte Carlo simulations of all energies. This data yielded a core resolution of 12.5 m.

Method 1 intersects the major axes of the second moment ellipses, while Method 2 intersects the lines connecting the centers of gravity of the images with the source locations. Method 1 works for all sources, both point sources and extended sources. Method 2 works only for point sources but achieves a better resolution. Since Mrk 421 is a point source, we use only Method 2. Shown in Figure 4.8, we obtain a core resolution of 12.5 m over the full range of simulated energies.

The energy resolution is calculated using the true (E_{true}) and reconstructed (E_{rec}) energies of each Monte Carlo event² as

$$\mathfrak{R}_{\text{energy}} = \frac{E_{\text{rec}} - E_{\text{true}}}{E_{\text{true}}}. \quad (4.6)$$

The value below which 63% of events occur is the energy resolution. For all events,

² *Note:* For this preliminary analysis, we have not attempted to optimize the Energy Estimator function.

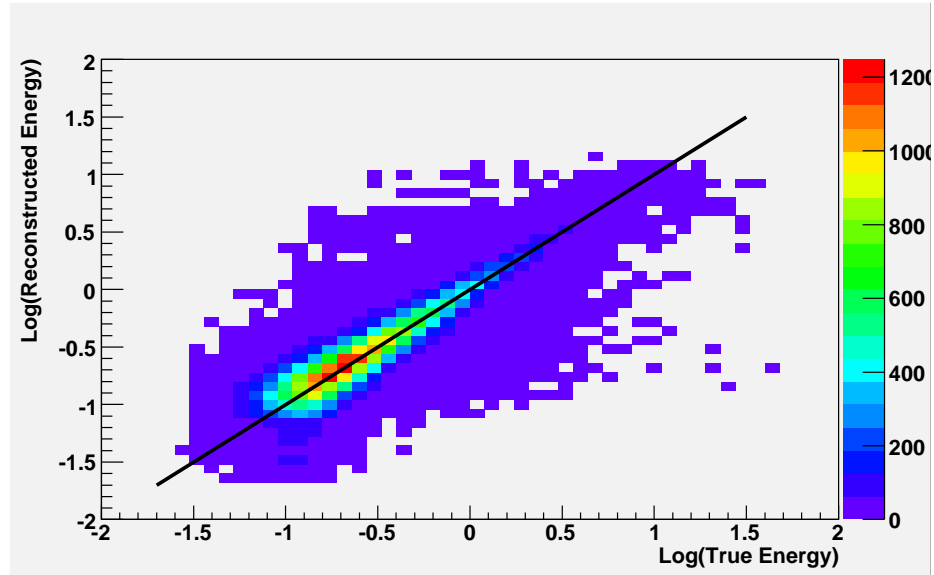


FIGURE 4.9: The logs of the true and reconstructed energies for the Monte Carlo data are plotted against each other. The red line shows the one-to-one relationship of the two values being equal.

the energy resolution is 34%. Figure 4.9 shows the log of the true and reconstructed energies plotted against each other, also demonstrating the accuracy of the energy reconstruction.

4.6 First Stereo Results from VERITAS

All the runs listed in Table 4.1 were analyzed using the *eventdisplay* package with the standard default values. These output files were then processed with *mscw_energy*, also with the default values. The runs were then evaluated by a custom *ROOT* script to determine γ -ray rates and significances.

One purpose of the custom *ROOT* script was to optimize cuts on θ^2 and *MSCW*

for this data set. The optimization aims at maximizing the Q-factor, defined as the γ -ray acceptance divided by the square root of the background acceptance for a particular cut:

$$Q = \frac{A_\gamma}{\sqrt{A_{\text{bg}}}}. \quad (4.7)$$

It scales with the statistical significance of weak signals obtained with a certain cut. For the cut optimization, all runs are treated as tracking runs.

As this is the first data taken with the new stereo VERITAS system, many aspects—pointing, point spread function of the optics, trigger nonuniformity and biases, etc.—are not well understood. Despite this fact, the two-telescope data on Mrk 421 are very good.

4.6.1 Cutting on θ^2

The first cut to be optimized was θ^2 , the square of the angular distance of the reconstructed arrival directions of the primary γ -rays from the source direction. This is the most important cut for stereo data, and is very powerful at removing background events from the source signal.

Initially, a histogram is made of the θ^2 values for all events passing a very weak cut of $MSCW < 1.0$. This removes the most obvious background events, to make the cut optimization cleaner. The resulting histogram shows a prominent peak close to $\theta^2 = 0$, with a tail that decreases linearly as a function of θ^2 . Since there should be no excess at values $\theta^2 > 0.4 \text{ deg}^2$, one can assume all contributions there are from background events. We then fit a line to the histogram for $0.4 \text{ deg}^2 \leq \theta^2 \leq 1.0 \text{ deg}^2$,

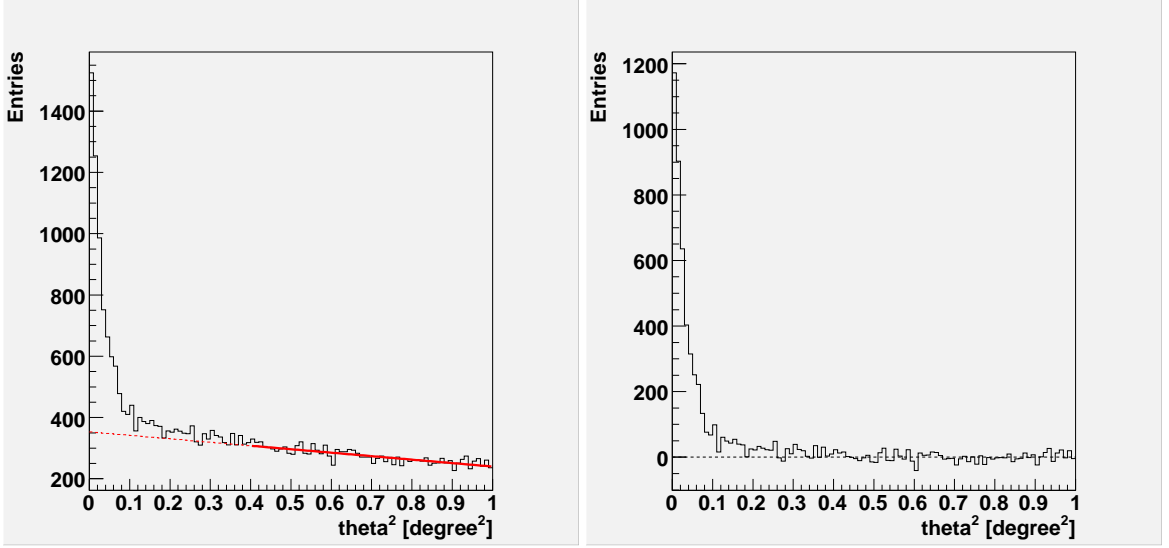


FIGURE 4.10: Plots of θ^2 , the square of the angular distance of the events from the source position, for the Mrk 421 data. On the left, θ^2 for all data (solid line) and OFF data (dotted line). The line for OFF data was fit from the dark solid line, assuming no excess for large θ^2 . The right shows the residual excess in the θ^2 distribution. Here, a loose cut of $MSCW < 1.0$ was used.

and extrapolated it to small values of θ^2 to represent all background events. This fit is shown in Figure 4.10a, along with the total θ^2 histogram. The “OFF line” was subtracted from the full histogram, leaving behind the ON excess histogram, seen in Figure 4.10b.

The Q-factor is then calculated for this residual histogram. Figure 4.11 plots the Q-factor, as well as signal and background acceptances, versus the cut in θ^2 . This gives a maximum Q-factor $Q_{MAX} = 2.87$, with a signal acceptance of 54%, and a background rejection of 97%. This equates to an optimal cut of $\theta^2 < 0.025 \text{deg}^2$, corresponding to an angular resolution of the two-telescope VERITAS system of $\theta = 0.16^\circ$. As evident in Section 4.5, our simulations appear to overestimate the angular errors, as they yield a resolution of 0.29° . In these early observations with a new system,

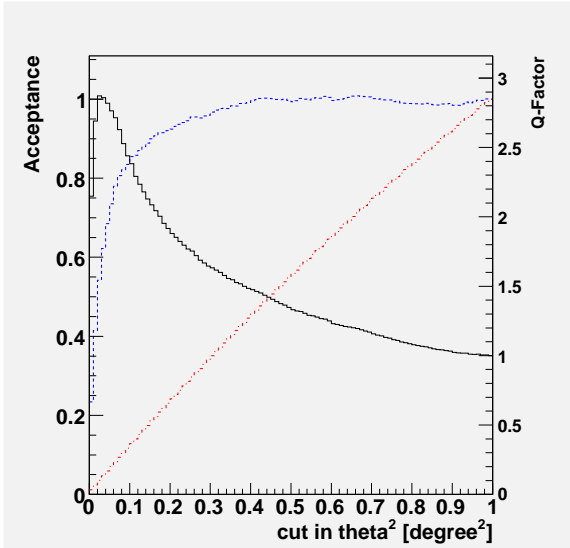


FIGURE 4.11: Plot of the Q-factor as a function of the applied θ^2 cut (solid black line, right axis). Also plotted are the signal acceptance (blue dashed line) and background acceptance (red dot-dashed line).

much about the telescopes, including quality of pointing and mirror alignment, remains uncertain. Further study will allow us to understand these behaviors and improve future simulations.

4.6.2 Cutting on Mean Scaled Width

The data are now processed through the custom *ROOT* script again. From here we can optimize the cut on *MSCW*. Data that pass the θ^2 -cut will be placed into two separate histograms (ON and OFF), based on the reconstructed origin of the primary γ -ray.

For this study, the ON region is a circle of radius 0.22° centered on the source. The OFF region is an annulus of inner radius 0.4° . The complete histograms of *MSCW* for both the ON and OFF regions are shown in Figure 4.12.

The Q-factor is then calculated on the residual histogram. Figure 4.13 plots the Q-factor, as well as signal and background acceptances, versus the *MSCW* cut. This

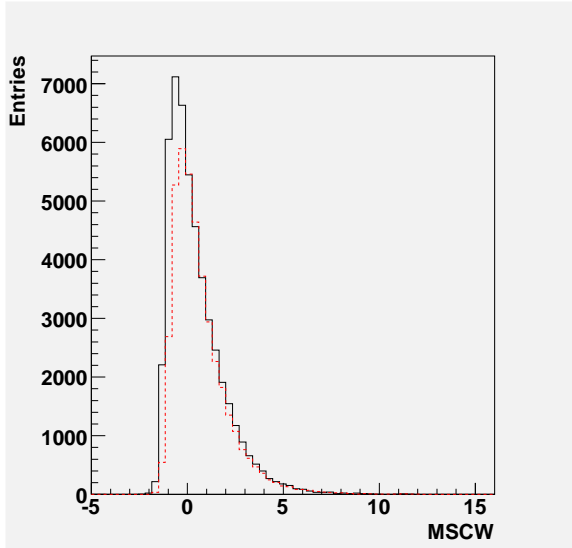


FIGURE 4.12: Plots of $MSCW$ for the Mrk 421 data for ON data (solid line) and OFF data (dotted line). Here, a loose cut of $\theta^2 < (0.22)^2$ was used.

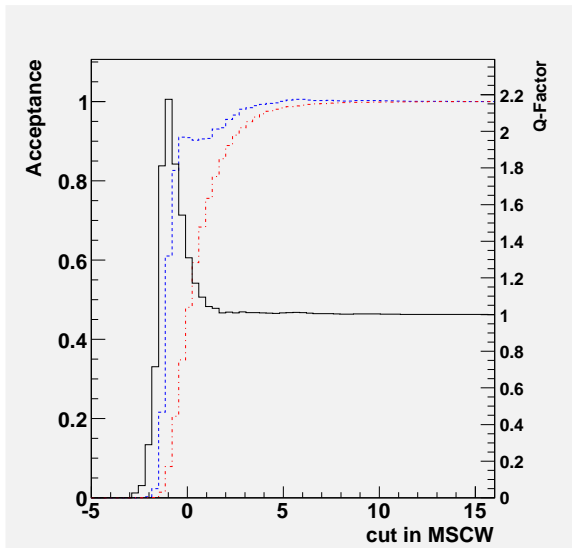


FIGURE 4.13: Plot of the Q-factor as a function of the applied $MSCW$ cut (solid line, right axis). Also plotted are the signal acceptance (blue dashed line) and background acceptance (red dot-dashed line).

gives a maximum Q-factor $Q_{MAX} = 2.15$, with a signal acceptance of 61%, and a background rejection of 92% for the cut of $MSCW < -0.21$.

4.6.3 Mrk 421 Light Curve

After the cuts on θ^2 and $MSCW$ were established, the data were processed again using these cuts. This yielded an average γ -ray rate of $2.91 \pm 0.07 \gamma \text{ min}^{-1}$ after

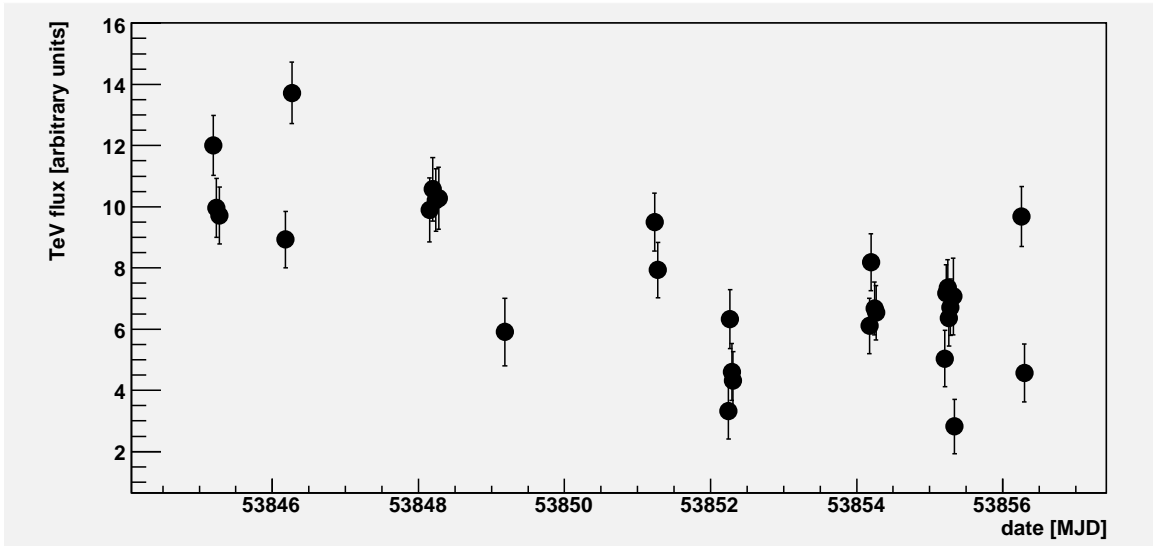


FIGURE 4.14: Light curve from the April–May 2006 dark run for Mrk 421. Each data run is represented by one point on the graph. Error bars are on the one-sigma confidence level.

cuts. Correcting for the cut efficiencies, the true rate inferred from these data is $8.83 \pm 0.21 \gamma \text{ min}^{-1}$. The total significance was found to be 39σ for 14.3 hours of data.

The flux measured for each of these runs was used to produce a preliminary light curve of Mrk 421, seen in Figure 4.14. Absolute flux calibration has yet to be done, but by comparison to the Crab rate of $\sim 6 \gamma \text{ min}^{-1}$ derived by Celik (2007), we estimate a variable flux for Mrk 421 on the order of 1/2 that of the Crab. This high variability can be seen between runs taken on the same night, even though Mrk 421 was not in its most active state. Such variability over short time scales was evident in numerous observations in the past with the Whipple 10 m telescope. The improved sensitivity of VERITAS will ultimately provide much better measurements of this variability on all time scales.

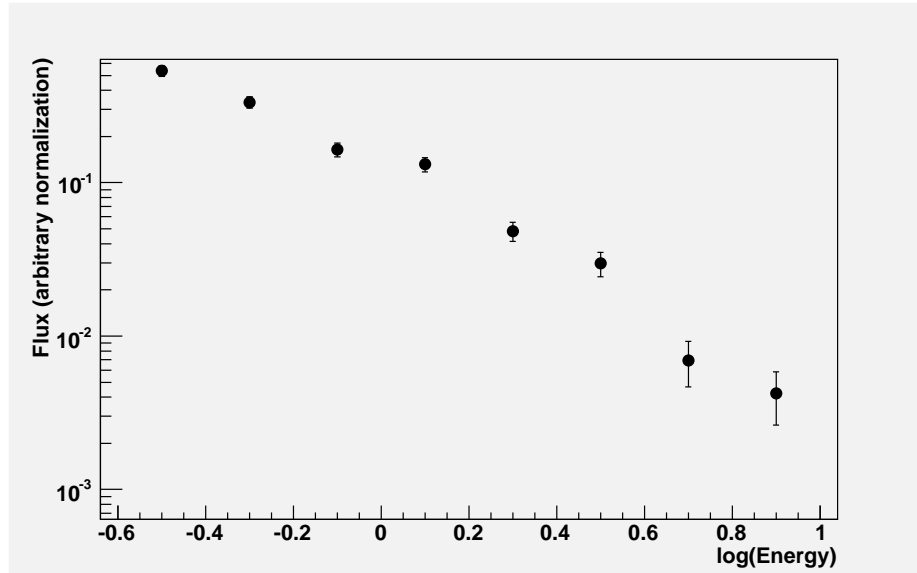


FIGURE 4.15: Reconstructed energy spectrum of the blazar Mrk 421 from the first VERITAS stereo data.

4.6.4 Energy Spectrum

In order to get a more accurate energy spectrum, only ON–OFF pairs were used in this process; Wobble and Tracking mode data were ignored. Due to the high significance of these runs, the nine pairs of data during this dark run were enough to generate a spectrum with small statistical errors. Data were fit to the Monte Carlo energy histogram as described in Section 4.3. This resulted in the energy spectrum shown in Figure 4.15. Based on our preliminary analysis, we get a spectral index of $\Gamma = 2.26 \pm 0.06$. For the Crab Nebula, the Whipple 10 m telescope gives $\Gamma = 2.5 \pm 0.1$ (Rebillot *et al.*, 2006). The results on Γ are comparable to previous results from earlier experiments where Mrk 421 was in a high state, *e.g.* the Whipple 10 m (Krennrich *et al.*, 2002), HEGRA (Aharonian *et al.*, 1999), and H.E.S.S. (Aharonian *et al.*, 2005c).

Chapter 5

SSC Modeling of Blazar Emission

5.1 Rationale

The previous chapter describes the analysis of VERITAS observations of the blazar Mrk 421. Extracting astrophysical results will require one to observe the source with good observational coverage over the entire electromagnetic spectrum. Such intensive multiwavelength observation campaigns are planned for the years 2007 and 2008. In this chapter, we present a theoretical study relevant for such multiwavelength studies. We explore whether X-ray measurements alone can be used to constrain the magnetic field in jets. If this were possible, the combined X-ray and γ -ray measurements could be used to break additional model degeneracies.

5.2 Measurement of the Jet Magnetic Field

During the last decade, time resolved multiwavelength observations of blazars have emerged as a powerful tool to study AGN jets. The most detailed data so far comes from joint observations of satellite-borne X-ray telescopes (ASCA, BeppoSAX, *RXTE*, XMM) and ground-based TeV γ -ray telescopes (CAT, HEGRA, Whipple); see Krawczynski (2004), Krawczynski (2005), Tavecchio (2005), and references therein.

The tight correlation between the X-ray and TeV γ -ray fluxes found for the blazars Mrk 421 and Mrk 501 (Buckley *et al.*, 1996; Takahashi *et al.*, 1996; Krawczynski *et al.*, 2000; Sambruna *et al.*, 2000) is commonly taken as strong evidence for synchrotron-Compton models in which a single population of electrons emits X-rays as synchrotron emission and γ -rays as inverse Compton emission off synchrotron target photons. Since the X-ray and γ -ray observations give complementary information about the same high-energy electron population, it becomes possible, in principle, to break model degeneracies.

A major goal of blazar observations is to determine the key parameters describing the jet plasma, such as the bulk Lorentz factor Γ , the jet Doppler factor¹ δ_j , the energy densities of the magnetic field, the thermal particle component, and the relativistic particle component. X-ray and TeV γ -ray observations reveal flux variability on time scales of minutes, indicating that the emission originates very close ($\sim 10^{16}$ cm) to

¹ The jet Doppler factor is defined by $\delta_j^{-1} = \Gamma(1 - \beta \cos(\theta))$ with Γ the bulk Lorentz factor of the emitting plasma, β its bulk velocity in units of the speed of light, and θ , the angle between jet axis and the line of sight in the observer frame.

the central engine (Gaidos *et al.*, 1996; Catanese and Sambruna, 2000; Krawczynski *et al.*, 2001). A measurement of the the jet properties at the jet-base would constrain the processes of matter accretion and jet formation, and would establish a crucial link between violent processes near a black hole of $10^{-5} (M_{\text{BH}}/10^8 M_{\odot})$ pc radius and the kpc-scale radio and X-ray jets.

While snapshots of the Spectral Energy Distribution (SED) constrain the parameters of emission models, there is no single source for which the model parameters have been determined unambiguously. In the case of “red” blazars (MeV/GeV blazars), the intensity of “external” radiation fields which supply the target photons for inverse Compton processes is not well constrained (see, *e.g.*, Tavecchio *et al.*, 1998, for a summary of constraints that can be derived from the broadband SED). In the case of “blue” blazars (TeV blazars), models are simpler as external radiation fields are thought to be weak. However, a highly uncertain amount of extragalactic extinction owing to pair-production processes of TeV γ -rays interacting with intergalactic infrared photons (Gould and Schröder, 1967; Stecker *et al.*, 1992) renders the interpretation ambiguous.

Additional constraints can be derived from the temporal evolution of the broadband energy spectra that reflect the evolution of the electron energy spectra owing to various physical processes. If synchrotron-Compton models do indeed apply, and if synchrotron cooling dominates the energy losses of electrons, high energy electrons will lose their energy more rapidly than low energy electrons. The flux variability at higher energies should lead the variability at lower energies, and a measurement of the

“time lag” between the flux variability observed in different bands should constrain the magnetic field inside the jet plasma.

With this aim, various authors have used the Discrete Correlation Function (DCF) of Edelson and Krolik (1988) to search for a time lag between fluxes measured in different X-ray bands and to constrain the jet magnetic field. Unfortunately, the measurements have not produced a clear verification of the basic picture. Based on a four-day uninterrupted observation of the blazar Mrk 421 with the ASCA satellite, Takahashi *et al.* (2000) used the DCF formalism to determine a time lag between the 0.5 – 1 keV and 3 – 7.5 keV fluxes. Rather than revealing a constant time lag indicative of synchrotron cooling of electrons in a certain magnetic field, the analysis showed that the time lag changed constantly in its value and its sign.

Based on four XMM observations of ~ 10 hrs duration, Sembay *et al.* (2002) performed a DCF analysis and derived an upper limit on the time lag between the soft (0.1 – 0.75 keV) and hard (2 – 10 keV) emission of 300 sec. This upper limit translates into a lower limit on the magnetic field of $2 (\delta_j/10)^{-1/3}$ G, uncomfortably high for synchrotron-Compton models.

5.3 Synchrotron Self-Compton Simulations

We use the time dependent SSC code of Coppi (1992) to create artificial data sets. The code assumes a spherical emission region of radius R that approaches the observer with a bulk Lorentz factor Γ . The emission volume is filled with an isotropic

electron population and a tangled magnetic field of mean strength B .

We create a light curve by changing the rate of freshly accelerated electrons $N_0(t)$.

We assume an electron acceleration spectrum following

$$dN_e/d\gamma = N_0(t) \times \gamma^{-p} \times \exp(-\gamma/\gamma_{\max}) \quad (5.1)$$

with a spectral index $p = 2$, and a high-energy cutoff γ_{\max} that is constant for each single simulation. The code self-consistently evolves the coupled partial differential equations describing the energy spectra of the non-thermal electrons and photons, taking into account synchrotron emission and self-absorption, as well as continuous and non-continuous energy losses owing to inverse Compton processes in the Thomson and Klein-Nishina regimes, respectively. The photon density evolves as

$$\frac{\partial n_\gamma}{\partial t} = q_\gamma - p_\gamma - \frac{c}{R(1 + \kappa)} n_\gamma, \quad (5.2)$$

where $q_\gamma d\epsilon$ and $p_\gamma d\epsilon$ are the rate of photons being produced inside and outside the energy interval $[\epsilon, \epsilon + d\epsilon]$, while the last term represents photons escaping from the emission region. The electron density evolves as

$$\frac{\partial n_e}{\partial t} = Q_e - \frac{\partial}{\partial \gamma} [\dot{\gamma}_{\text{cont}} n_e] + q_e - p_e - \frac{n_e}{t_{e,\text{esc}}}, \quad (5.3)$$

where $Q_e(\gamma, t)$ is the rate of freshly accelerated electrons, $\dot{\gamma}_{\text{cont}}$ is the decrease in an electron's Lorentz factor and $q_e d\gamma$ and $p_e d\gamma$ are the rates of particles being produced or scattered inside and outside the Lorentz factor interval $[\gamma, \gamma + d\gamma]$ (Krawczynski *et al.*, 2002). The SSC code assumes that the synchrotron emission provides the dominant target photon field.

Mimicking the duration of a typical multiwavelength observation campaign, we generated artificial data sets of 30 days duration (observer frame). The first 10 days were discarded from subsequent analysis so that the target photon fields and low-energy electron distributions could reach a steady level. We created each artificial data set by a series of N triangle bursts of accelerated particles:

$$N_0(t) = \sum_{i=1}^N A_i h(t - T_i). \quad (5.4)$$

Here, the function $h(t - T_i)$ represents triangle pulses of constant width, centered on the times T_i randomly chosen between 0 and the duration of the flaring period; the heights A_i of the triangle pulses were chosen to vary by a factor of 4, with a preference toward smaller values. Choosing triangle flares of $t_{\text{flare}} = 10$ hrs duration and $N = 30$, this method produced light curves that closely resemble observed ones. A sample of the output can be seen in Figure 5.1.

5.4 Generating Data Sets

We use six different sets of model parameters with magnetic field values ranging from 0.005 G to 0.2 G. In the following, we refer to the six parameter configurations as configuration “A” through “F”. The magnetic field values have been chosen such that the electrons emitting synchrotron radiation at 10 keV (observer frame) have synchrotron cooling times ranging from the flare duration t_{flare} to much longer than the flaring time. The six parameter combinations are listed in Table 5.1. They are similar to those inferred from detailed modeling of observation campaigns of the

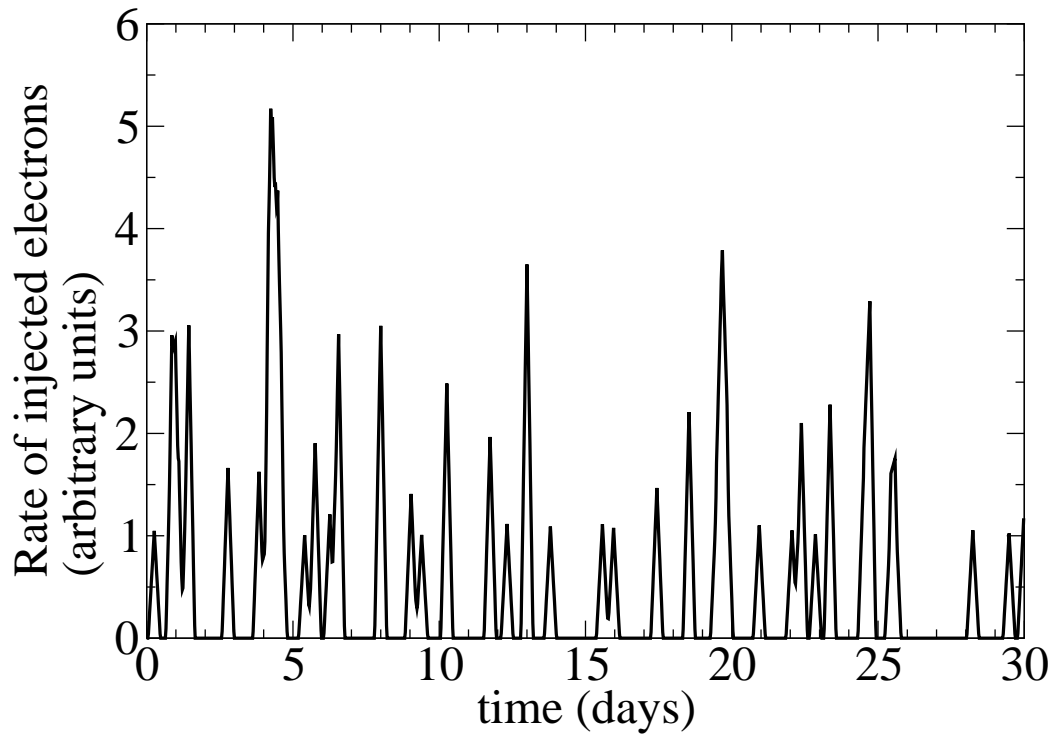


FIGURE 5.1: The figure shows a sample of an artificially generated electron acceleration history $N_0(t)$. The curve was generated by superimposing a random succession of 30 triangle pulses, each 10 hrs wide. The first ten days are a transient period used to get the system going; data is only taken from the last 20 simulated days. The electron acceleration history is shown in the stationary observer frame. Data shown are from input file 14.

TABLE 5.1: Magnetic field values and calculated cooling times for each set, as well as other important initial conditions. Also, the relation of each cooling time to the flaring time (10 h).

Set	B (G)	R (10^{16} cm)	$\delta_j^{-1}(R/c)$ (h)	γ_{\max}	$t_{\text{cool}}(10 \text{ keV})$ (h)	$t_{\text{cool}}/t_{\text{flare}}$
A	0.20179	1.30	2.7	0.04	10.9	1
B	0.07063	2.17	4.4	0.7	52.7	5
C	0.04708	2.61	5.3	0.8	96.8	10
D	0.01412	4.34	8.9	0.7	589	60
E	0.00614	4.78	9.8	0.4	2056	200
F	0.00562	4.34	8.9	0.1	2346	234

blazars Mrk 421 and Mrk 501 (Krawczynski *et al.*, 2000, 2001, 2002).

We use $\delta_j = 45$ throughout this analysis, which agrees well with Mrk 501 and Mrk 421 data and which assures that the internal electron densities are sufficiently low such that internal pair production processes are negligible.

Figure 5.2 shows sample SEDs for each parameter combination. These specific combinations were chosen so that the resulting SEDs would resemble the known blazars Mrk 421 and Mrk 501. To keep the results generic, we give results in rest-frame luminosities per solid angle, and we do not apply extragalactic extinction.

Figure 5.3 shows sample 3 keV, 25 keV and 1 TeV light curves for one of the parameter combinations. Close examination shows that the 25 keV fluxes indeed lead the 3 keV fluxes, as expected in the case of dominant synchrotron cooling.

The 1 TeV flux lags the 25 keV flux, owing to the fact that the TeV flux traces the evolution of the electron densities convoluted with the evolution of the synchrotron target photons. Our code mimics the effect that it takes approximately a light crossing time until a change in the target photon density has reached all the electrons inside

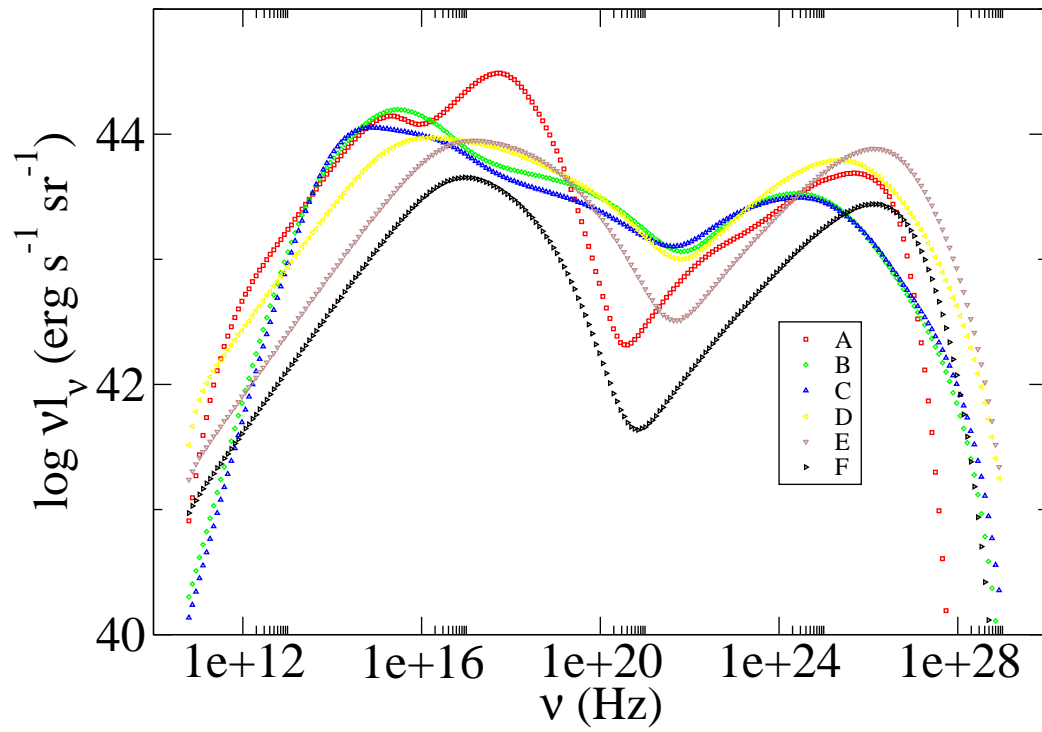


FIGURE 5.2: Representative SED plots of each of the six parameter combinations listed in Table 5.1. The SEDs are shown in the observer frame.

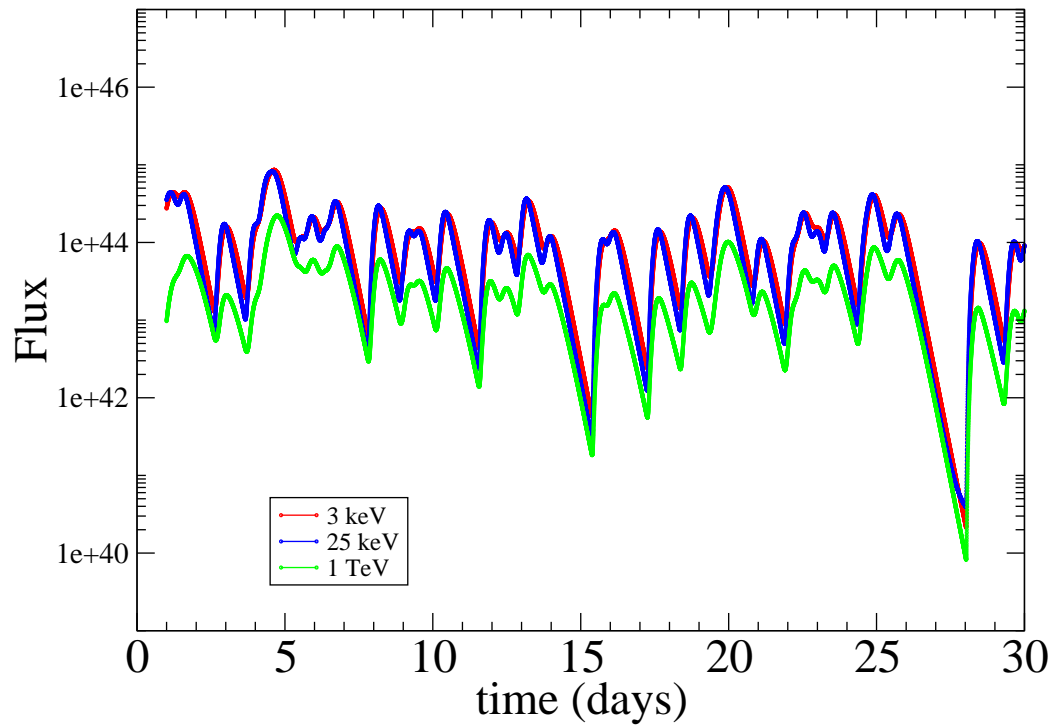


FIGURE 5.3: Sample light curves (3 keV, 25 keV, and 1 TeV) from “run 14” of the model parameter set “D”. Close examination shows that the 25 keV fluxes lead the 3 keV fluxes and the 1 TeV fluxes. The light curves are shown in the observer frame.

the emission volume. In the following, we will discuss the “time lag” behavior more quantitatively.

For each of the six different magnetic field values, we simulate 20 different artificial data sets. We apply a DCF analysis to each of the 20 data sets, allowing us to study the statistical distribution of the derived parameters.

5.5 Analysis Procedure

For each simulation we bin the 3 keV and 25 keV lightcurves into 15 min bins (observer frame). Based on the binned flux values $f_3(t_i)$ and $f_{25}(t_i)$ we compute the DCF as a function of time lags τ that are multiples of 1 hr:

$$DCF(\tau) = \frac{1}{M(\tau)} \sum DCF_i(\tau), \quad (5.5)$$

where the sum runs over all $M(\tau)$ pairs of binned flux values f_3 and f_{25} that are separated in time by τ . Here, $DCF_i(\tau)$ is an “estimate” of the DCF derived from a single pair of fluxes:

$$DCF_i(\tau) = \frac{(f_3(t_i) - \bar{f}_3)(f_{25}(t_i + \tau) - \bar{f}_{25})}{\sigma_3 \sigma_{25}}, \quad (5.6)$$

with σ_3 and σ_{25} being the standard deviation of the 3 keV and 25 keV fluxes, respectively. If experimental measurement errors are non-negligible, Equation 5.5 has to be modified as described by Edelson and Krolik (1988). In the sample DCF shown below, we plot “error bars” which represent the “error on the mean DCF value”:

$$\sigma_{\text{DCF}}(\tau) = \frac{1}{M-1} \left\{ \sum_i \text{DCF}_i(\tau) - \text{DCF}(\tau) \right\}^{1/2}. \quad (5.7)$$

For each simulated data set, we determine the “time offset” τ_{DCF} at which the DCF reaches its maximum value. For each of the six parameter combinations we use all of the 20 simulated data sets to compute the arithmetic mean of the observed time lags as well as the RMS of the distribution.

Further below, we will compare the DCF time offsets with the differences in synchrotron cooling times. Considering the effect of synchrotron cooling alone, the latter are calculated in the following way. Assuming a delta-functional approach to the synchrotron emissivity, electrons of Lorentz factor γ emit synchrotron photons of energy

$$E = \frac{3}{4\pi} h e B \gamma^2 \overline{\sin \alpha}, \quad (5.8)$$

with $\overline{\sin \alpha} = \sqrt{\frac{2}{3}}$ for an isotropic pitch angle distribution. Photon energies E are Doppler boosted to energies

$$E' = \delta_j E \quad (5.9)$$

in the observer frame. Based on Equations 5.8 and 5.9, the Lorentz factors γ_1 and γ_2 responsible for the radiation observed at energies E'_1 and E'_2 can be determined.

In the jet reference frame, the synchrotron cooling time of electrons of Lorentz factor γ is given by Rybicki and Lightman (1979) as

$$t_{\text{cool}}(\gamma) = \left[\frac{4}{3} \sigma_{\text{T}} c \left(\frac{B^2}{8\pi m_e c^2} \right) \gamma \right]^{-1}, \quad (5.10)$$

with the Thomson cross section $\sigma_{\text{T}} = 6.652 \times 10^{-25} \text{ cm}^2$, and $B^2/8\pi$ the magnetic

field energy density. Jet frame times transform into observer frame times according to

$$t' = \frac{1}{\delta_j} t. \quad (5.11)$$

From Equations 5.10 and 5.11 we can derive the difference in synchrotron cooling times of the electrons with Lorentz factors γ_1 and γ_2 responsible for the radiation observed at energies E'_1 and E'_2 :

$$\Delta t'_{\text{synch}} = \frac{1}{\delta_j} (t_{\text{cool}}(\gamma_1) - t_{\text{cool}}(\gamma_2)) \quad (5.12)$$

$$= \left[\frac{4}{3} \sigma_{\text{T}} c \delta_j \left(\frac{B^2}{8\pi m_e c^2} \right) \right]^{-1} \left(\frac{1}{\gamma_1} - \frac{1}{\gamma_2} \right). \quad (5.13)$$

Inverting the equation, one can compute the jet magnetic field (in the jet frame), from the “time lag” $\Delta t'_{\text{synch}}$:

$$B = 3 \left(\frac{\pi h \cdot e \cdot m_e c \cdot \sin \alpha}{\sigma_{\text{T}}^2 \delta_j (\Delta t'_{\text{synch}})^2} \right)^{1/3} \left(\frac{1}{E'_2} + \frac{1}{E'_1} - \frac{2}{\sqrt{E'_2 \cdot E'_1}} \right)^{1/3} \quad (5.14)$$

$$\simeq (\Delta t'_{\text{synch}}/4.8)^{-2/3} \times (\delta_j/45)^{-1/3} \times 0.045 \text{ G}. \quad (5.15)$$

Various authors have used τ_{DCF} , the time offset that maximizes the DCF, as an estimator of $\Delta t'_{\text{synch}}$, and have used Equation 5.15 to estimate the jet magnetic field.

As we will show below, this procedure can produce incorrect results.

5.6 Measuring Time Lags with the Discrete Correlation Function (DCF)

For each of the six different parameter combinations, we simulate 20 independent artificial data sets to estimate the statistical accuracy to which we can determine τ_{DCF} . As an example of our procedure, Figure 5.4 summarizes the DCF results for parameter combination “D”. The points with error bars show the DCF computed for one of the 20 “runs”. For this particular run, the DCF peaks at a time offset of $\tau_{\text{DCF}} = -4.1$ hrs. The negative sign shows that the 25 keV flux indeed leads the 3 keV flux. The shaded band shows the range of DCF values obtained for the entire set of 20 runs.

One sees that the DCF values vary considerably, especially at larger time offsets. The fact that the DCF varies much more than suggested by the error bars originates from the correlation between different pairs of measurements and was discussed already by Edelson and Krolik (1988). Averaged over all 20 simulated runs, the mean time offset at which the DCFs peak was found to be $\tau_{\text{DCF}} = -4.8$ hrs. The minimum and maximum τ_{DCF} values found in the 20 runs were 4 hrs and 6 hrs, respectively. These τ_{DCF} values on the order of ~ 5 hrs are substantially shorter than the corresponding difference in cooling times of 16 hrs.

Figure 5.5 shows τ_{DCF} versus $\Delta t'_{\text{synch}}$ for all six models. The numerical values are also given in Table 5.2. Most interesting is that the two times are clearly correlated, but that τ_{DCF} is always shorter than $\Delta t'_{\text{synch}}$. The discrepancy varies between a fac-

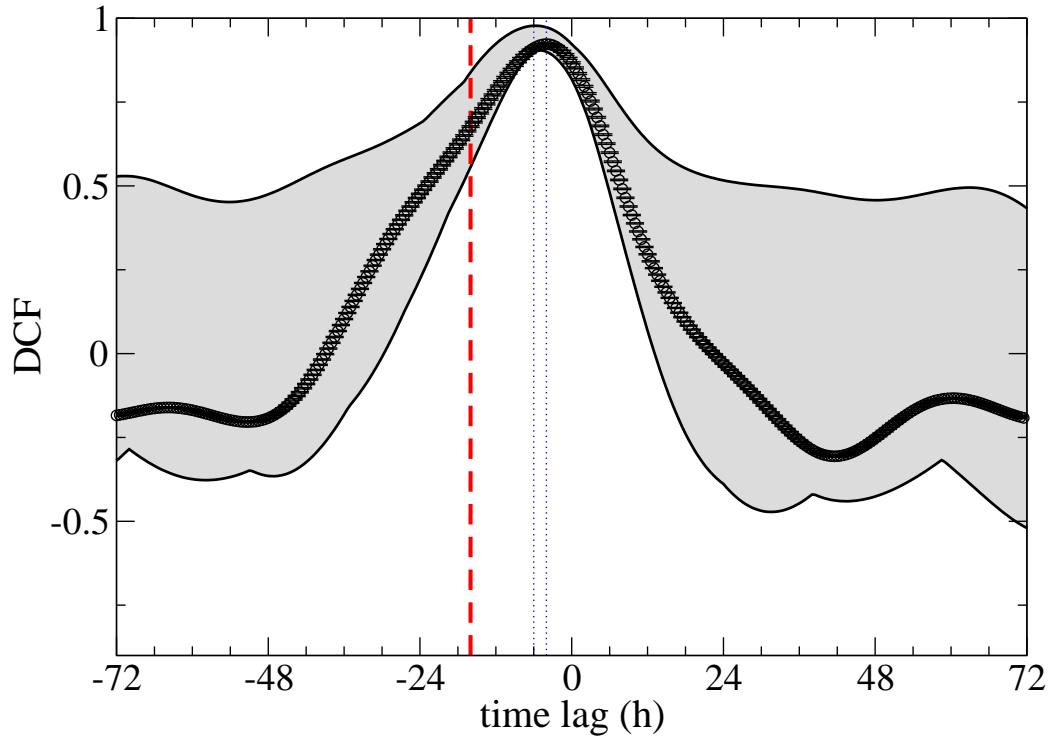


FIGURE 5.4: Sample plot of DCF for 3 keV vs. 25 keV. The time lags are shown in the observer’s frame. A binning of 15 minutes has been used. This DCF peaks at a negative lag of -4.1 hrs, corresponding to the 25 keV flux variability leading the 3 keV flux variability. This is the plot from “set D”, “run 14”. The bounding curves represent the range over which all 20 runs’ DCFs occurred. The dotted vertical lines represent the range over which the maximum DCF occurs for the 20 runs. The average observed lag of 4.8 hours is much shorter than the one computed from the synchrotron cooling times for this data set of 16 hours (thick dashed line).

TABLE 5.2: Time lags for each set. Errors on DCF values are root mean square values, calculated from averaging 20 runs per set. The first two DCFs are for 3 keV vs. 25 keV. The final DCF is for 25 keV vs. 1 TeV, scaled by the appropriate factor.

Set	τ_{DCF} with IC (h)	τ_{DCF} without IC (h)	$\tau_{\text{DCF}}/\delta_j^{-1}(R/c)$	$\Delta t_{\text{synch}}'$ (h)
A	-0.25 ± 0.01	-0.25 ± 0.01	0.55 ± 0.02	0.29
B	-1.00 ± 0.01	-1.25 ± 0.01	0.49 ± 0.09	1.4
C	-1.74 ± 0.05	-1.97 ± 0.07	0.45 ± 0.10	2.6
D	-4.79 ± 0.70	-5.72 ± 0.82	0.67 ± 0.30	16
E	-7.34 ± 2.70	-17.1 ± 12.0	1.3 ± 1.9	55
F	-6.94 ± 2.73	-16.5 ± 12.5	1.6 ± 2.2	62

tor of 1 and a factor of 9 for the strongest (A) and weakest (F) simulated magnetic field values, respectively. For all but the smallest magnetic fields, the spread of the τ_{DCF} -values derived from different runs is rather small. Thus, assuming an observation campaign of 20 days, the precision to which the maximum of the DCF can be determined will exclusively be limited by the accuracy of the experimental flux measurements and the observational coverage. Figure 5.6 compares the magnetic field values inferred from τ_{DCF} and Equation 5.15 with those used to simulate the data sets. As can be seen from the figure and the values listed in Table 5.3, the magnetic field values are overestimated by factors of between 1.5 and 6 for the strongest and weakest simulated magnetic field values, respectively.

We have investigated if the inverse Compton cooling of the electrons produces the short DCF time offsets. For this purpose we ran the SSC code again, this time suppressing the inverse Compton processes. The τ_{DCF} -values calculated for these simulations are also given in Table 5.2. For all sets of model parameters but those with the smallest B field, the mean τ_{DCF} -values computed with and without inverse

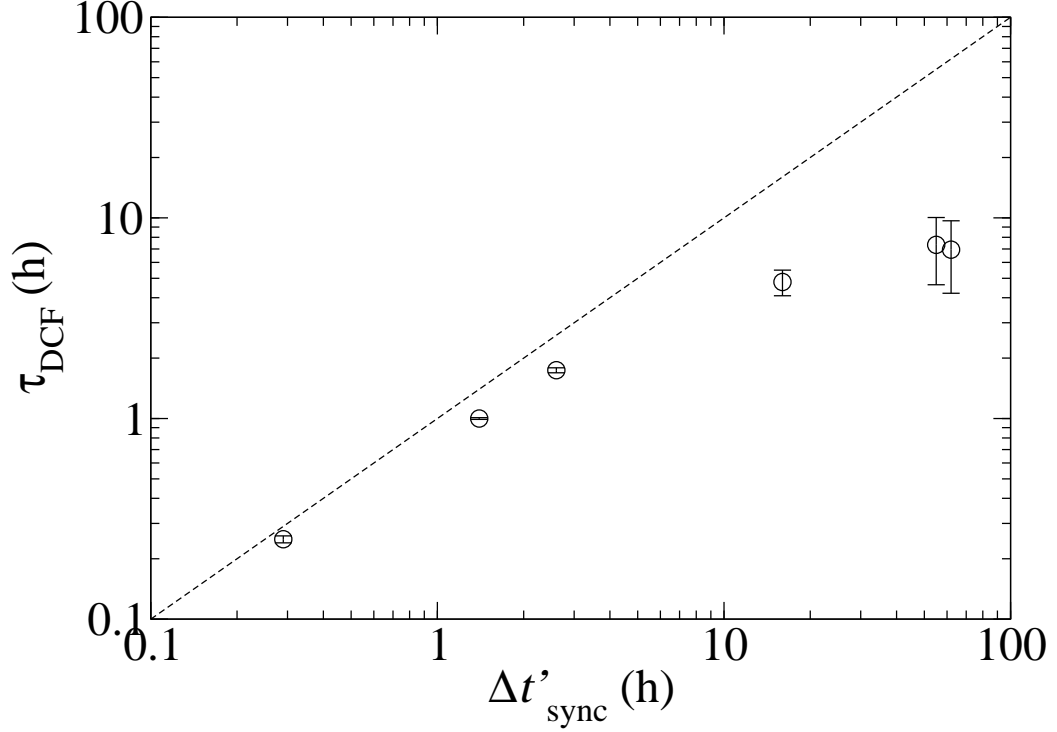


FIGURE 5.5: The computed time lag from the discrete correlation function (τ_{DCF}) plotted against the expected time lag from Equation 5.13 ($\Delta t_{\text{synch}}'$). See Table 5.2 for specific values. Error bars are RMS-values from averaging over 20 runs. The dotted line represents the two values being equal.

TABLE 5.3: Actual B used in each set and those calculated from the DCF for each set using Eq. 5.14. Errors here are propagated from the errors on the DCF times.

Set	B_{true} (G)	B_{DCF} (G)
A	0.20179	0.32 ± 0.01
B	0.07063	0.127 ± 0.001
C	0.04708	0.088 ± 0.002
D	0.01412	0.045 ± 0.005
E	0.00614	0.034 ± 0.012
F	0.00562	0.035 ± 0.014

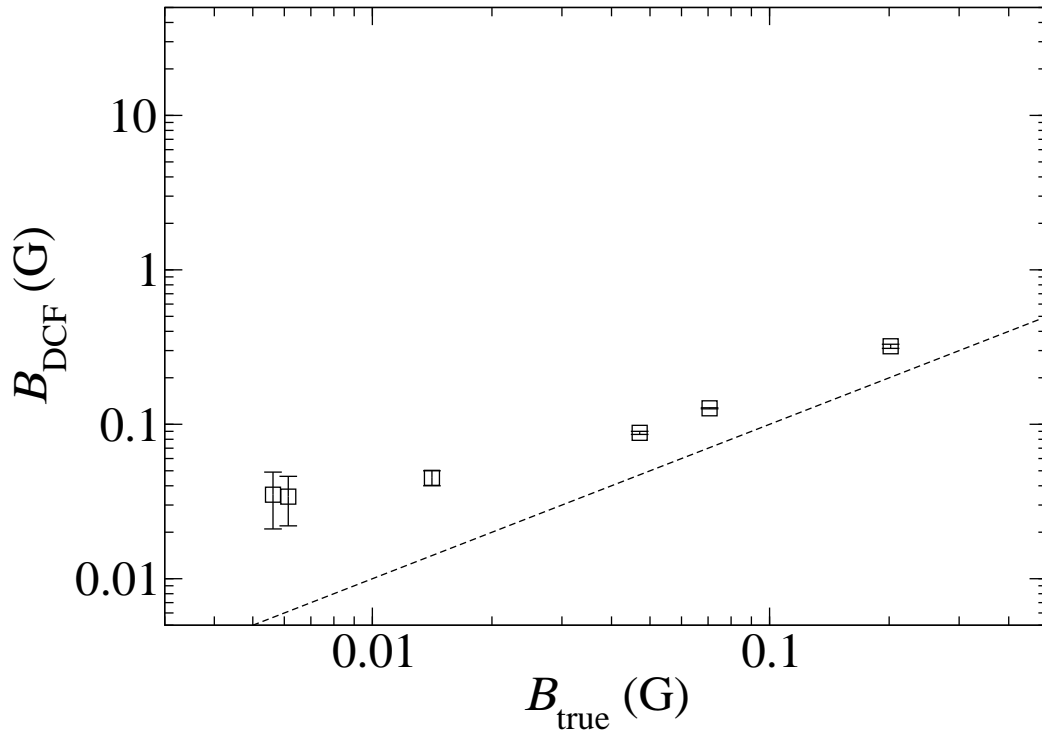


FIGURE 5.6: The magnetic field values calculated from the DCF lags plotted against the actual values used in the simulations. RMS-values are propagated from the RMS-values on the DCF time lags. The dotted line represents the two values being equal. See Table 5.3 for specific values.

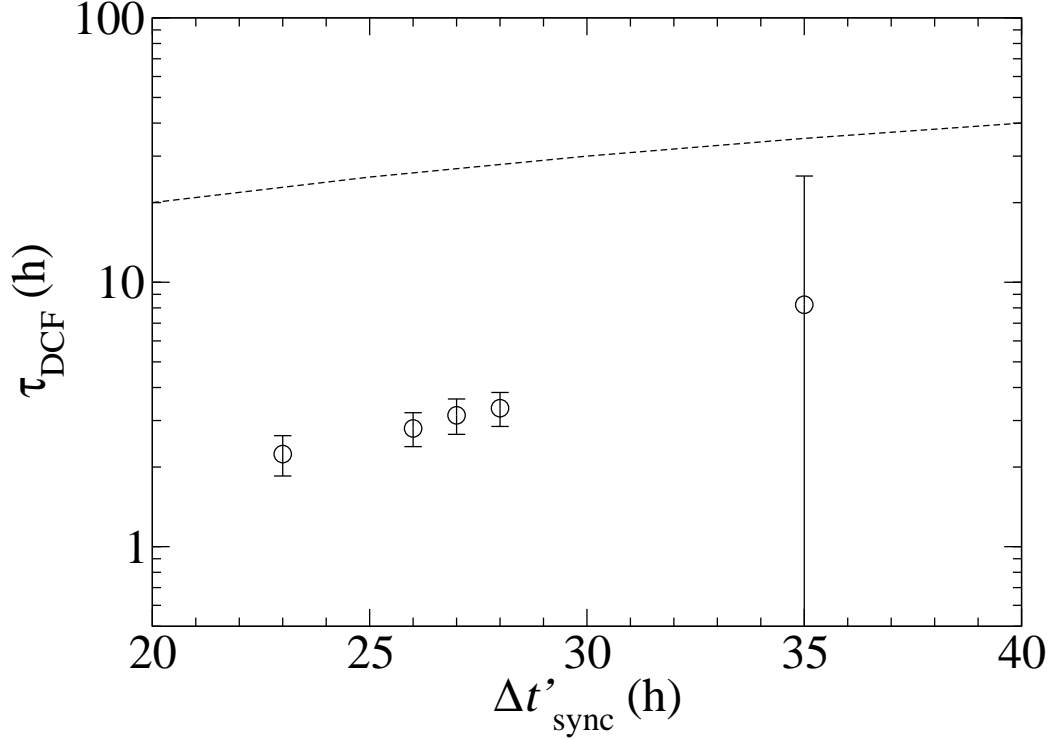


FIGURE 5.7: The DCF times were calculated between 3 keV and (left to right) each of 25 keV, 50 keV, 75 keV, 100 keV, and 1 TeV. The comparison to the expected lag time is shown. The dotted line represents the two values being equal.

Compton cooling are almost identical. We explain this finding with two factors. First, synchrotron emission is the dominant cooling mechanism for all considered parameter combinations. Second, the energy dependence of the inverse Compton cooling times is weaker ($\propto \sqrt{\gamma}$) than the energy dependence of the synchrotron cooling time ($\propto 1/\gamma$).

To see if our chosen range of 3 keV – 25 keV could be causing problems, additional energy ranges were considered. For one data set, we calculated the DCF between 3 keV and each of 25 keV, 50 keV, 75 keV, 100 keV, and 1 TeV. The results comparing the calculated time lag and that predicted by Equation 5.14 are shown in Figure 5.7.

We next considered flares of varying lengths. The data sets were rerun using flares

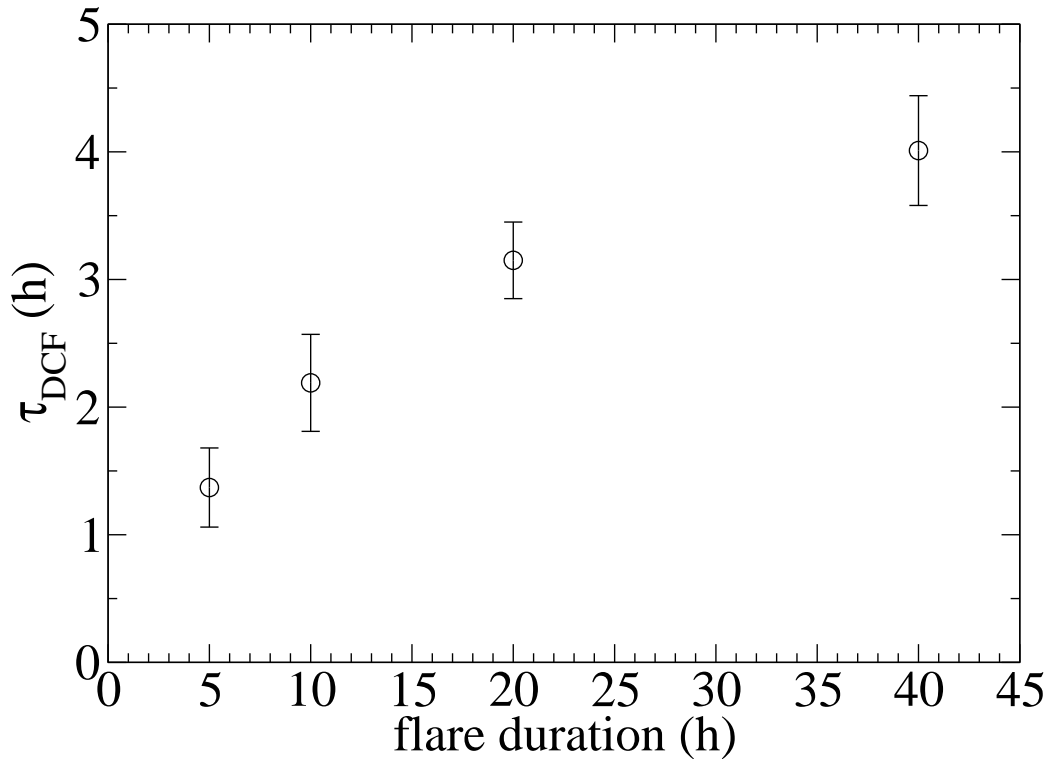


FIGURE 5.8: The DCF times were calculated from runs with flares of 5 h, 10 h, 20 h, and 40 h durations. There is an obvious correlation with flare duration and DCF lag times.

of 5, 10, 20, and 40 hr durations. As Figure 5.8 shows, there is a strong dependence on flare duration of the DCF lag times.

Another case we examined was that of a single flare. Using these light curves, we calculated the DCF as before. We also did so using just the peak of the light curve generated by the single flare. Then we hand calculated the time difference between the maxima of the curves for 3 keV and 25 keV. We also tried fitting an exponential to the decaying light curve to find a cooling time. None of the methods yielded similar values.

We also examined other possibilities, but none yielded better results. These other

variables included using different bin sizes for the DCF, changing the escape times of particles in the SSC code, using different doppler factors, and assuming that the peak emission comes from various fractions of the peak frequency ν_c . Using just the peaks from the lightcurves to calculate the DCF instead of using the entire curve yielded larger DCF values, but also a much larger spread in those values over the 20 runs.

5.7 Comparing of DCF Time Lags to Expected Results

Various authors have used the maximum of the soft/hard X-ray DCF to constrain the magnetic field (Chiappetti *et al.*, 1999; Krawczynski *et al.*, 2000; Takahashi *et al.*, 2000; Sembay *et al.*, 2002). We have used a Synchrotron Self-Compton code to check the validity of the standard equation used in this analysis. In the framework of our simple model (flares are produced by a variation of the rate of accelerated electrons alone), the standard approach overestimates the magnetic field by factors of between 1.5 and 6.

The DCF searches for a linear correlation between two lightcurves with a constant time offset. However, differences in cooling times do not produce a constant time offset between the fluxes observed in different bands. This has two important effects. First, as we assume instantaneous electron acceleration up to the highest electron energies, phases of rising fluxes do not exhibit any interband time lag behavior. A more realistic modeling of electron acceleration by the second order Fermi process

would even result in a lag of opposite sign, *i.e.* the soft X-rays leading the hard X-rays (Kirk and Mastichiadis, 1999). Second, even phases of falling fluxes do not exhibit a consistent time lag behavior. At the beginning of the decaying phase of a flare, softening of the X-ray energy spectrum produces a time lag behavior. However, once the decaying phase is long enough that the peak of the synchrotron SED shifts to energies below those sampled by the low-energy X-ray observations, the high and low energy fluxes decrease with the same decay constant. As the DCF is calculated from data of the full light curves, the net effect is a time lag τ_{DCF} shorter than $\Delta t'_{\text{sync}}$.

Application of the method to real astrophysical data may even be more problematic as current models may underestimate the complexity of flares. Each flare might be produced by a different emission region with a different magnetic field. The emission plasma may expand or compress during individual flares, which would result in a change of the magnetic field and in adiabatic cooling or heating of the non-thermal particles (Coppi and Aharonian, 1999). High energy particles may escape diffusively from the emission region with an energy dependent “electron escape time.” The angle between the bulk motion of the emitting plasma and the observer may change with time. If the magnetic field is not randomly oriented, the mean angle between the magnetic field and the line of sight might also change with time.

Our two main conclusions from our study and these arguments are the following: (i) the determination of the magnetic field from the DCF peak is more complicated than previously thought, and (ii) the results of a more detailed analysis will depend on the assumptions underlying the calculations. Reliable estimates of the plasma

5.7 Comparing of DCF Time Lags to Expected Results

parameters can not be derived from a timing analysis alone, but should take advantage of as many observational constraints as possible.

Chapter 6

Discussion

6.1 Summary of Thesis Results

In this thesis we have shown first results from the VERITAS two-telescope system. The experiment behaves as expected with no surprises in the performance of major hardware components. The comparison of Mrk 421 γ -ray data with Monte Carlo simulations shows excellent agreement overall. Simulation of the two-telescope system achieves an energy threshold of 220 GeV, and angular, core, and energy resolutions of 0.29° , 12.5 m, and 34% respectively. Performance of the three- and four-telescope system will improve over these two-telescope values.

The analysis presented here gives Mrk 421 fluxes and energy spectra similar to those observed in earlier campaigns. Future blazar studies will aim at intensive multiwavelength observations. In this thesis, a theoretical study is described illuminating the possibility of using the X-ray data of such campaigns to constrain the jet mag-

netic field. The study has shown that simple methods used by other authors do not perform as expected.

6.2 VERITAS Performance

Single-telescope comparisons in Holder *et al.* (2006) show that even T1 by itself shows significant advances over the Whipple 10 m telescope. The stereo set-up already greatly reduces the number of background events causing the telescope to trigger; average trigger rates are down from ~ 160 Hz for T1 data to ~ 90 Hz for stereo data. This rate decrease is also in spite of the fact that the telescope trigger levels have been lowered as well, capitalizing on the increased background rejection to ensure events are not dominated by noise.

The agreement between the Monte Carlo simulations and data taken on Mrk 421 demonstrates that the telescopes are behaving as planned. The simulations take into account how the electronics of the system are supposed to behave. The distributions of the parameters examined in this study are very similar.

Unfortunately for this calibration, Mrk 421 is a very active source, with its flux varying constantly. One needs to study a more steady source, such as the Crab Nebula, to further solidify the extent of the improvement of VERITAS over previous generations of IACTs. As its energy spectrum is well known, Crab observations can be used to determine the sensitivity of the new system and to test the absolute flux calibration.

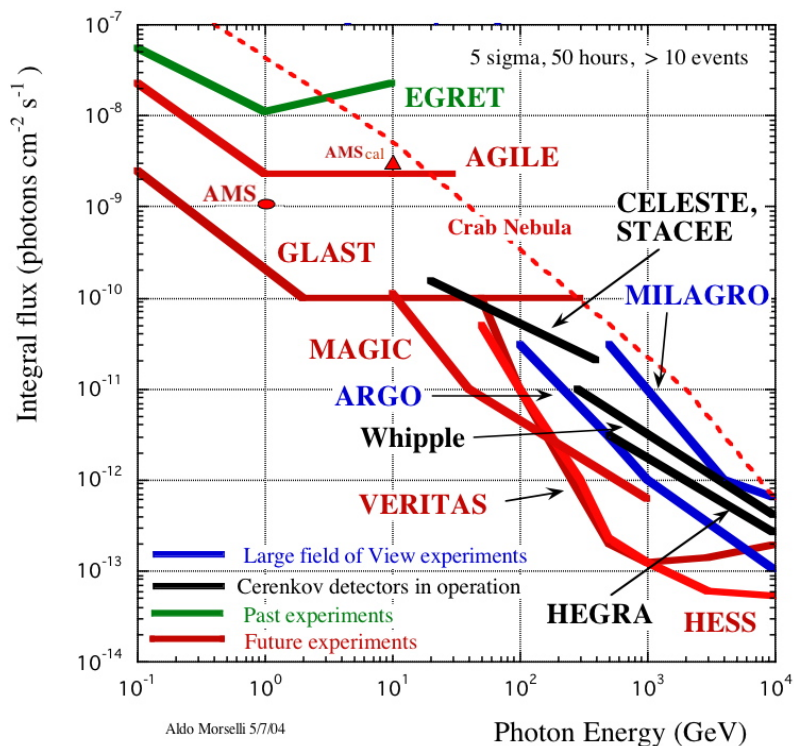


FIGURE 6.1: Sensitivity of major experiments in high energy astrophysics. Figure from Morselli (2003).

The success of the two-telescope VERITAS system paves the way for the full array of four telescopes, set to come online by January, 2007. The addition of two more telescopes, along with requiring three or even four telescopes triggering to record an event, will increase the array's sensitivity by an additional factor of ~ 2 . Figure 6.1 shows how the planned full VERITAS sensitivity compares with other high energy experiments. The number of sources detected in the Northern Hemisphere as a result should be similar to the overwhelming success of the H.E.S.S. array in the Southern Hemisphere. This multitude of γ -ray sources to study should reveal new and interesting physics as well as expand our current knowledge of existing sources.

6.3 The Future of γ -ray Astrophysics

This is a very exciting time in γ -ray astrophysics. Several new telescopes are poised to come online in 2007. If the past is any indicator, these new experiments will set off an explosion of new learning in the field. Not just extensions to older projects, many of these telescopes utilize new ideas and technologies.

GLAST (Gamma-ray Large Area Space Telescope), a new space-borne γ -ray telescope, will use solid-state detectors in place of the spark chambers of the past, reducing the required space while increasing efficiency. Scheduled to launch in 2007, GLAST will detect γ -rays from 20 MeV – 300 GeV with an effective collection area of $> 8000 \text{ cm}^2$. It will have a much higher angular resolution and an order of magnitude better sensitivity than EGRET (Ritz *et al.*, 2005).

On the ground, new telescopes are being built in addition to VERITAS. The MAGIC Collaboration is building a second 17 m IACT at their site in La Palma, and MAGIC II should be completed in 2007 (Baixeras and *et al.*, 2005). The H.E.S.S. Collaboration is building a new telescope at their site in Namibia. This new IACT will have a 28 m diameter mirror. Placed in the center of the existing H.E.S.S. array, the new telescope will work with the existing array as H.E.S.S. II, achieving even lower energy thresholds than before (Vincent, 2005).

These new telescopes will allow us to simultaneously monitor blazars at MeV to TeV energies. Observing blazars with radio, IR, optical, X-ray, and γ -ray telescopes will enable us to test the models with unprecedented spectral coverage and sensitivity.

We hope that the observations will make it possible to identify unambiguously the nature of the accelerated particles (protons or electrons/positrons). Once the emission mechanism is interpreted, the observations will give information about the jet parameters (magnetic field, particle to magnetic field energy density, etc.), and thus contribute to our understanding of the structure of AGN jets.

Appendix A

X-ray Data Analysis of 1ES 1959+650 and Mrk 421

A.1 Multiwavelength Campaign Overview

Observing blazars in TeV γ -rays reveals only a small portion of the information that can be gained from them. Blazars emit energy over a wide range of energies. To truly understand how they work, one must look at data from more than one energy band. To this end, multiwavelength campaigns have been mounted on several known blazars. Through these, many telescopes working at different energies observe the same source at the same time, to reveal a wealth of information not available to a lone observer.

Looking at the SED for blazars, it is obvious where one should probe besides γ -rays for information. The first peak of the SED occurs in X-rays. Monitoring this

highly active energy band will then yield more insight into the complex processes inside these interesting sources.

This data analysis was a part of two separate multiwavelength campaigns. The first looked at the TeV blazar 1ES 1959+650 in Summer, 2002 (Krawczynski *et al.*, 2004). The second involved Mrk 421 in December, 2002 and January, 2003 (Rebillot *et al.*, 2006). Both campaigns combined data from the radio, optical, X-ray and γ -ray bands. In particular, analysis of the X-ray data is discussed in Section A.2. Section A.3 covers the phenomenon of “orphan” flares, discovered for both sources during their campaigns.

A.2 RXTE Data

Launched in 1995, the *Rossi X-Ray Timing Explorer* (*RXTE*) is a satellite designed to observe fast-moving X-rays passing near Earth. It consists of three individual instruments: the All Sky Monitor (ASM; Levine *et al.*, 1996), the Proportional Counter Array (PCA; Jahoda *et al.*, 2006), and the High-Energy X-Ray Timing Experiment (HEXTE; Rothschild *et al.*, 1998). While some data from the ASM were used, the analysis concentrated on data from the PCA. The 15 – 250 keV HEXTE data were not used due to their poor signal to noise ratio. Due to their close proximity in time, analysis of data for both multiwavelength campaigns were nearly identical.

The X-ray analyses was based on the 3 – 25 keV data from the PCA. Standard-2 mode PCA data gathered with the top layer of the operational proportional counter

units (PCUs) were analyzed. The number of PCUs operational during a pointing varied between two and four.

After applying the standard screening criteria and removing by hand abnormal data spikes, the net exposure in each Good Time Interval (GTI) ranged from 160 s to 4.43 ks for 1ES 1959+650, and from 168 s to 9.01 ks for Mrk 421. Spectra and light curves were extracted with FTOOLS. For Mrk 421, spectral analysis was restricted to the 4 – 15 keV energy range. Analysis of earlier *RXTE* data showed corrupted behavior (exceptionally high or low count rates of individual bins not compatible with the energy resolution of the instrument) below 4 keV. Above 15 keV, the data of most pointings were dominated by background.

Background models were generated with the tool *pcabackest*, based on the *RXTE* Guest Observatory Facility (GOF) calibration files for a “bright” source with more than 40 counts s⁻¹ PCU⁻¹. Comparison of the background models and the data at energies above 30 keV showed that the model underestimated the background by 10%. We corrected for this shortcoming by scaling the background model with a correction factor of 1.1. Response matrices for the PCA data were created with the script *pcarsp*.

The spectral analysis was performed with the Sherpa package. A Galactic neutral hydrogen column density of $1.027 \times 10^{21} \text{ cm}^{-2}$ was used for all observations of 1ES 1959+650, while a value of $1.31 \times 10^{20} \text{ cm}^{-2}$ was used for Mrk 421. Since the analysis is restricted to the energy region above 3 keV, the hydrogen column density has only a very minor influence on the estimated model parameters. Single-power-

law models resulted in statistically acceptable fits for all data sets. Data for Mrk 421 were complemented by data from the ASM. Fluxes were derived by averaging the “summed band intensities” acquired during one day.

A.3 “Orphan” Flares

Overall, observations during both multiwavelength campaigns showed an extremely high confidence level for X-ray and TeV γ -ray flux correlation, $\sim 97\%$ for Mrk 421. However, when they were not correlated, the difference was extreme (widely different TeV γ -ray fluxes for a single X-ray flux and vice versa).

The most extreme example of this uncorrelated flux is the so-called “orphan” flare. Most often regarding X-ray/TeV γ -ray correlation, this occurs when the intensity in one band increases without a noticeable counterpart in the other. Mrk 421 saw an orphan X-ray flare on January 13, 2003 (Rebillot *et al.*, 2006), while 1ES 1959+650 saw an orphan γ -ray flare on June 4, 2002 (Krawczynski *et al.*, 2004). Figure A.1 shows a light curve of 1ES 1959+650 in various energy bands, clearly showing this orphan TeV flare.

The existence of these orphan flares goes against the results of previous one-zone SSC models of blazar emission. Many groups have modeled the X-ray and TeV γ -ray emission from Mrk 421 data (Inoue and Takahara, 1996; Bednarek, 1997; Bednarek and Protheroe, 1999; Boettcher *et al.*, 1997; Mastichiadis and Kirk, 1997; Tanihata *et al.*, 2001; Krawczynski *et al.*, 2001; Konopelko *et al.*, 2003; Kino *et al.*, 2002;

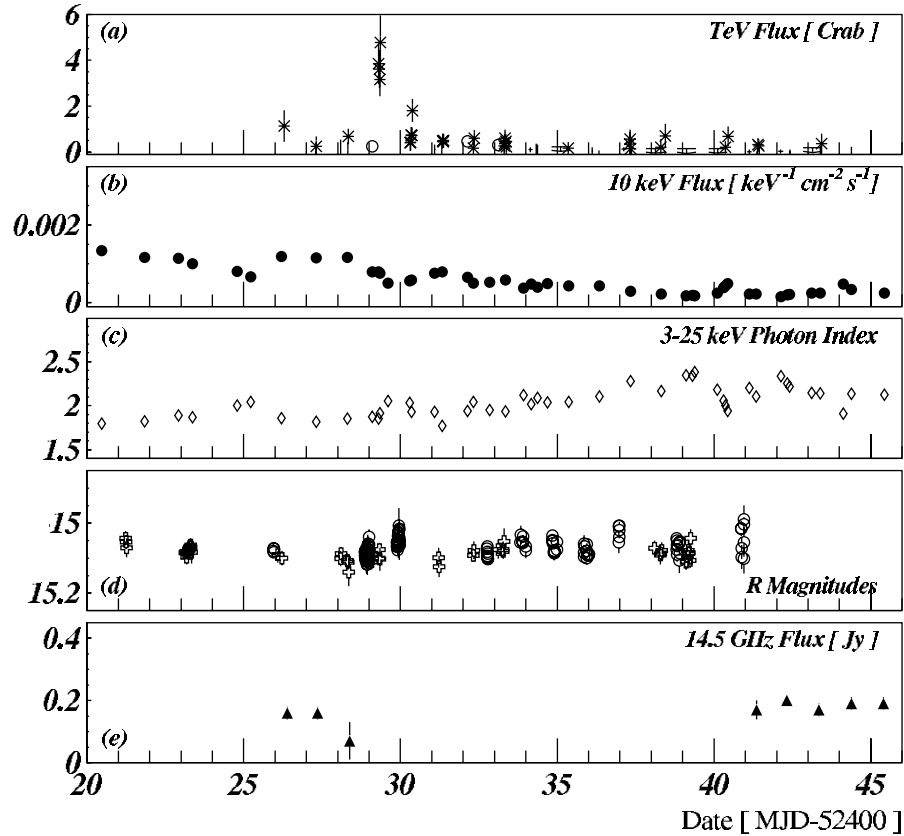


FIGURE A.1: Light curve of 1ES 1959+650 from 2002 multiwavelength campaign. (a) Whipple (*stars*) and HEGREA (*circles*) integral TeV γ -ray fluxes in Crab units above 600 GeV and 2 TeV respectively. The Whipple data are binned in 20 minute bins; the HEGRA data are in diurnal bins. (b) *RXTE* X-ray flux at 10 keV. (c) *RXTE* 3 – 25 keV X-ray photon index. (d) Absolute *R* magnitudes. (e) The 14.5 GHz flux density. Figure from Krawczynski *et al.* (2004).

Błażejowski *et al.*, 2005), and early results indicated this one-zone model could satisfactorily describe a wealth of data. However, as Krawczynski *et al.* (2002) showed, this method fails even for the blazar Mrk 501. Clearly, a one-zone SSC model is too simple to account for the full complexity of a blazar’s inner workings. Further investigations into the phenomenon of orphan flares are necessary to better understand these processes.

Appendix B

Daily VERITAS Data Quality Monitoring

B.1 Motivation and Procedure

In order to ensure the VERITAS telescopes are performing as expected during this intense and crucial period where many systems are unstable and constantly evolving, some sort of sanity check must be instituted to make sure weeks of data are not completely lost because no one caught the fact that something wasn't working properly.

Starting January, 2006, we began to look at each night's data for any inconsistencies or blatant instances of data errors. Not knowing in advance what to really look for, the tools and plots used evolved over the second half of the season. When problems arose, we found ways to better detect issues automatically. However, some

visual inspection of runs was still necessary to confidently determine data reliability.

Each morning, a few runs were chosen to be analyzed. These were selected to include the various observing modes of the previous night, as well as those runs with known issues (such as rate spikes) to get the best overview of the general data quality. The runs were first analyzed using the *eventdisplay* package. Then, *ROOT* was used to run a custom script that generated a set of plots, as well as printed out errors and other useful information about the runs to help determine if there were major data issues.

B.2 Analysis and Results

Initially, the night's laser run is looked at by hand, event by event, using the *eventdisplay* package. If something is wrong with the laser run, all data from the night are affected, since they are analyzed against this laser run. Laser events should light up the entire camera. It is very easy to tell if something is definitely wrong by flipping through a few of these events.

The custom *ROOT* script was used to analyze the data every morning. For each analyzed data run, it produced a series of plots used to determine at a glance if something major was wrong with the data. The various histograms displayed include pedestals and pedestal variances, gains, time offsets, the many Hillas parameters (see Sect. 4.1.1), number of tubes per event, tube with the maximum value, a rate plot, time between consecutive events (dt), and centroid distributions.

Figure B.1 shows an example of the data output. The plot distributions are representative of how things look when (most) everything is working as it should. Many histograms show tight groupings in the data, while others show a smooth decaying curve or a flat horizontal line. The “max pixel” distribution, however, is not ideal. It shows that one pixel is firing far more often than any other. This could simply be the result of a star in the field of view, or it could be a more important problem with faulty high voltage on that pixel. While not obvious at first, after a few days of daily analysis, one learns to quickly recognize these shapes as good signs.

Figure B.2 shows an example of data when the telescopes are not working as they should. Notice the differences in the plots compared to those of Figure B.1. For example, the time plot is not flat, corroborating the note of a rate spike by the observers. The Hillas parameter distributions are also decidedly skewed. The two telescopes are also behaving very differently, as the black and red histogram lines rarely overlap. After a night like this, the telescopes seriously need to be debugged.

The *ROOT* script also prints out diagnostic information, useful in determining how well the telescopes are performing. It will display a list of channels whose pedestals, pedestal variances, gains, or time offsets vary more than 4σ from the mean. It will list the number of events that have no maximum pixel, as well as the number of pixels that never have the maximum value. It will also list when an abnormally long (> 1 sec) time passes between consecutive events. All these pieces of information are useful in determining the quality of the data taken the previous night.

B.3 The dt Bump

During the early course of daily data quality monitoring, it was noticed that there was a slight bump in the plot of dt , the time between consecutive events. This curve should be zero at very short times, spiking to its peak at the deadtime for the system, currently $\sim 500 \mu\text{s}$. The curve should then exponentially decay out to longer values of dt . This is because, ignoring the deadtime, detectable events occur randomly in time, meaning a gaussian distribution of the time between events. Any deviation from this distribution means there is some bias within the system causing events to be detected at more regular intervals.

The dt bump, shown in Figure B.3, was noticed to occur at different sizes relative to the surrounding curve. It became a much more prominent effect when runs with very high data rates were analyzed. Here, the dt curve decayed to zero at a value less than 0.04 s. This left the bump standing alone (see Fig. B.3b).

Much speculation surrounded what could be causing this bump. Physically, it corresponds to many events occurring with the same amount of time between them. This means we had a fairly consistent ~ 25 Hz signal on top of our real data.

Eventually, the problem was traced down to the EventBuilder. When its event buffer fills, it must be flushed, sending all the events further up the data chain. This transfer time acts as a secondary deadtime, putting the telescope on hold until the transfer is complete. Since the data buffers are always the same size, it takes roughly the same amount of time for each transfer. This periodic disruption in the data flow

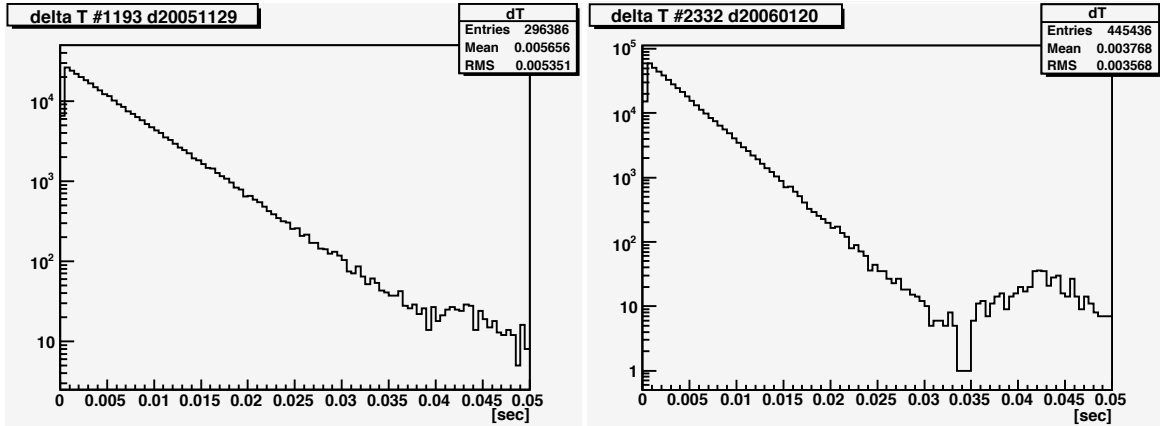


FIGURE B.3: Plots of dt , the time between consecutive events, for a run with a) low and b) high rates. The bump—which always occurs at ~ 0.04 sec, corresponding to ~ 25 Hz—is more prominent in the high-rate data. It blends more into the normal exponential decay of dt times for the lower-rate data.

is minimal, especially for the normal data rate, which is currently relatively low and for the most part masks the dt bump under the normal decay of times.

While in the end not determined to be a major problem, the issue of the dt bump is an example of how daily data quality monitoring noticed characteristics of the data that would not otherwise have been detected. This simply emphasizes the importance of this task in bringing a new, complicated system such as VERITAS online.

Appendix C

VAC: VERITAS Array Control

GUI

The *VAC* GUI was designed as a user-friendly way to interact with the VERITAS array control system. Its current incarnation can support the full array of four telescopes. It allows observers to interact with many subsystems, control all aspects of run definition and management, and displays status information and plots while the telescopes are taking data. The program was written in C++ using the QT development environment and consists of approximately 13,000 lines of code.

Below is the User's Manual for *VAC* v3.168.

C.1 Starting VAC

The graphical user interface for the array control system is located on the `arrayctl` computer. Through this program, you can gain access to various subsystems for debugging purposes, as well as accomplish all tasks needed for a night of observing (define and start runs, etc.). This program is a work in progress and will be evolving in look and functionality over time. This version has recently been expanded to handle the full four-telescope VERITAS system.

The array control and telescope control programs (`arrayctl` and `telectl`) are started automatically at system startup, they should not be started manually. Nor should any version of these programs be started on any other computer. This causes problems with the system's normal operation.

However, multiple versions of VAC may be running at once. Also, versions of the text based `simple-ui` may be running as well (though it is no longer recommended that you even try using this program under normal circumstances). Commands from each of these interfaces will be handled, in turn, by `arrayctl`, and each version of the interface programs will update with the results of these actions. This allows for simultaneous debugging from multiple locations.

Currently, VAC requires some subsystems to be started independently. Once the CORBA connection with these systems are better established and the programs are able to handle remote starts (or are daemonized and come up when their computers are powered on), VAC will be able to take over more aspects of their functionality.

C.1.1 Normal Operation

The following steps are taken to use the VAC to take data on a normal night, when the entire telescope array is functioning properly. This process involves defining individual runs for the telescope to take and initiating them. Data taking is done automatically.

1. Start the VAC program on the `arrayctl` computer:

```
> VAC
```

It has been noticed that the program can hang if there is no connection to the database. Be sure to check this if things are not working properly.

2. Start up the necessary subsystems using the **Start Subsystems** option in the **Observer** menu. Check which subsystems have established contact by looking in the status portion of the main window. Take the appropriate steps to initialize systems with which there is no contact, as outlined in the related wiki pages.
3. Initialize the night by choosing **Start Night** from the **Observer** menu. This takes care of calling the initialization routines for all the connected subsystems.

4. Define a new run by clicking the **Define Run** button. You will be prompted to enter all information pertaining to that run (run type, source, etc.). When you are done, click **Define + Prepare**.
5. Start the run by clicking the **Start Run** button. After being defined, the run should've automatically been selected in the Run Information Table. If it was not, you need to select the run in the table before starting the run.

The run will last for the duration specified when it was defined, or until manually terminated by the user by clicking the **End Run** button. If the speakers are properly connected to the computer, a sound will also play to alert you to the ending of the run. At this point, a new run may be defined and started.

If you would like to take an ON-OFF run pair, *VAC* can easily handle that for you. See Section C.2.1 for more info on taking pairs and other automatically started runs. The modifications to the Define Run sequence are as follows:

4. Click **Define Run** from the main window, and fill out the run information as normal, but do not define the run quite yet.
5. Under **Start Run...**, click **Automatically; start run in...**. Make sure **ON-OFF** is selected under **Auto Run Type**. This sets up the automatic runs.
6. Click **Define**. Two runs are automatically created. The first will start as soon as it is defined and prepared, which happens automatically. The second run will begin two minutes after the completion of the first run.
7. Kick back and relax while *arrayctl* automatically defines and starts the run. Don't forget to move the telescope in between runs!

The program may safely be quit by choosing **Exit** from the **File** menu, or by just closing the main window.

C.1.2 Debugging Systems

The following steps are taken to use the *VAC* before the telescopes have been brought into full operation, or to debug systems at any time. This process involves going to the individual subsystems' menus and accessing them directly.

1. Start the *VAC* program on the *arrayctl* computer:
> **VAC**

The following commandline options may also be used:

- **-f <filename>**: specify a different configuration file to use.
- **-n <nameserver>**: specify a different CORBA nameserver to use.

- **-q <host>**: specify a different host to provide QuickLook data.
 - **-t**: disable reading of temperatures of FADC boards.
 - **-s**: disable automatic “Update Status” calls.
 - **-d**: disable automatic checking for Free Disk Space remaining.
2. Start up the necessary subsystems using the **Start Subsystems** option in the **Observer** menu. Check which subsystems have established contact by looking in the status portion of the main window. Take the appropriate steps to initialize systems with which there is no contact, as outlined in the related wiki pages.
 3. Choose the appropriate item from the **Subsystem** menu (see Sect. C.2.4). This will bring up a separate dialog from which you can access the debugging commands for that system. The options are as follows:
 - **L3 (Ctrl+L)**
 - **Harvester (Ctrl+H)**
 - **EventBuilder (Ctrl+E)**
 - **L2 (Ctrl+X)**
 - **L1 (Ctrl+Y)** (display L1 rates, currently unsupported)
 - **DB (Ctrl+D)** (access items in the database)
 - **QI** (charge injection, currently unsupported)

C.2 Using the VAC

C.2.1 Main Window

The main window of *VAC* is shown in Figure C.1.

System Status

- **Harvester/QuickLook/L3/DB/PCS**

Displays the status of array-specific systems: the Harvester, QuickLook, L3, the Database, and the Positioning System. Information is updated automatically. A checked box means the CORBA connection is present; unchecked means there is a problem. While the current indicator system allows the user to click and change the status of the systems, it will be overwritten with the correct status automatically the next time the system does its automatic checking. Following L3 is a string showing the currently reported subsystem status. The positioner currently does not have a CORBA interface, so it will never be checked.

Quicklook is an exception to the CORBA connection. Though done on the harvester, it involves a direct connection and not the normal CORBA connection.

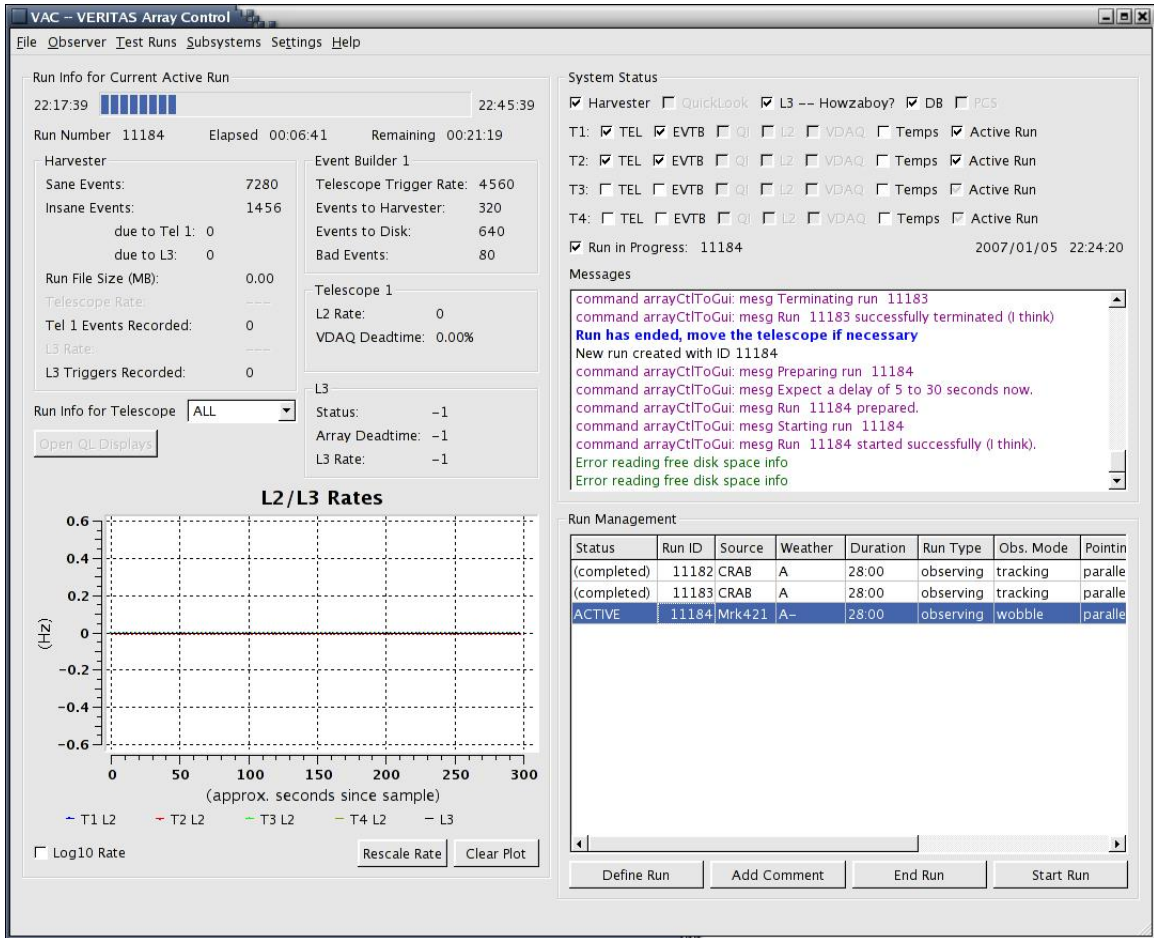


FIGURE C.1: Layout of the main VAC window.

Currently, the connection is checked only once, at program startup. If there is a problem, make sure the harvester is running, and restart *VAC*.

- **T1–T4: TEL/EVTB/QI/L2/VDAQ/Temps**

Displays the status of telescope-specific systems: *telectl*, *eventbuilder*, Charge Injection, L2, VDAQ, and FADC Temperature readings for Telescopes 1–4 respectively. Information is updated automatically. A checked box means the CORBA connection is present; unchecked means there is a problem. While the current indicator system allows the user to click and change the status of the systems, it will be overwritten with the correct status automatically the next time the system does its automatic checking. Currently, QI, L2, and VDAQ do not have properly functioning CORBA connections. They will not be checked, even when they are running properly.

Regarding FADC Temperatures: if the crate temperatures get too high (usually over 55° C), a warning message is printed. Try reading the temperatures again, because the fluctuation is so high, the state may pass. A further warning is printed when a board exceeds 60° C. In this case, they should be immediately shut down until the temperature decreases. If there is a problem in this process, or if more information is needed, the **Observer**→**Read FADC Temperatures** menu option may be used to display all temperature values. Temperatures are read every few minutes. An OK statement will appear if none of the boards show excessively high temperatures. If the Temps indicators are greyed out, automatic temperature readings have been disabled.

- **T1–T4: Active Run**

For convenience, this box displays whether a run is active on a particular telescope. Status is updated automatically. This status tells whether *eventbuilder* for each telescope is currently processing a run, or even if the run has just been prepared, and therefore a new run cannot yet be defined for that telescope. If the box shows the indeterminate “–” value, status cannot be determined because the connection to that telescope’s *eventbuilder* cannot be established.

- **Run in Progress**

When a run is active, this indicator is checked, and the active run number(s) listed following it. Information is updated automatically, though it doesn’t always coincide with when *arrayctl* commands are sent; it may take a couple seconds to read accurately.

- **Date and Time**

This information is taken from the database, and is updated automatically. It is in the form *yyyy/mm/dd hh:mm:ss*.

- **Messages window**

All information regarding what the system is up to, exceptions caught, etc.,

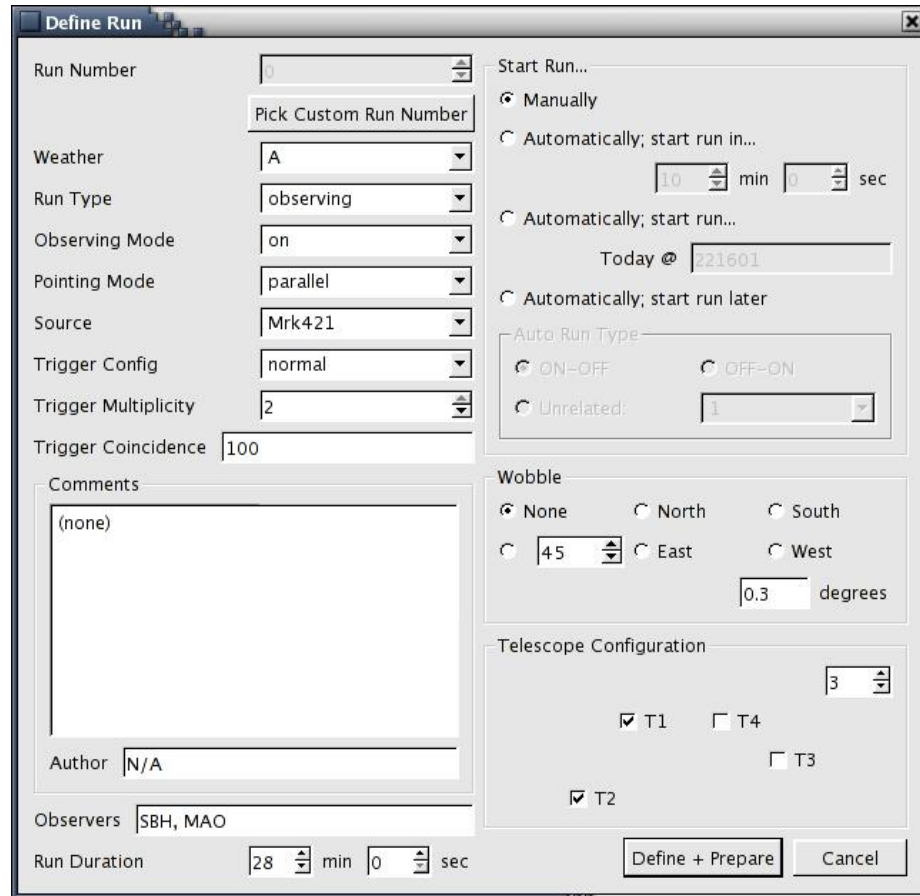


FIGURE C.2: Layout of the Define Run window.

is displayed in the message window. Most information of major importance is printed to the console as well, so it can be reached in case the GUI itself crashes. On startup, various system information is listed, including the program version number, CORBA nameserver being used, and program ID info. Messages appear in different colors to try and gain the observer's attention when necessary.

Run Management

- **Run Information Table**

Displays information for all runs currently on the *arrayctl* internal run list. This includes completed, active, prepared, and pending runs, as well as auto-runs that are counting down to their start. For each run, a variety of information is displayed in the different columns. More detailed information is available through **Run Info**, under the **Observer** menu (**Ctrl+I**). The columns currently displayed are run status (pending/prepared/active/completed/auto run

countdown to start, different than the run status from the database), run number, source, weather, duration, run type, observing mode, pointing mode, trigger method, config. mask, multiplicity, coincidence, and observers. The run list in the table is constantly updated, so a run defined using another client (or *simple-ui*) will appear in the table within a few seconds. The run status is also updated automatically.

- **Define Run**

Before a run can be started, it must be defined. Choosing this option prompts the user for all information necessary to create a run (see Figure C.2).

The required fields are as follows:

1. **Run Number:** usually automatically chosen by the database. If the field is left to zero, this will still happen. If you wish to suggest your own run number for the new run, you must first click on the **Pick Custom Run Number** button. A dialog will ask you to confirm overriding the automatic selection process, and the run number may now be changed. You will be asked a second time to confirm your choice of selecting a custom run number when you change the current run number from 0. Any unused run number is a valid choice. If you change your mind, simply click **Use Default Run Number** and the database will select the run number for you.
2. **Weather:** A+ to C-; rating the current conditions. Options appear in a pop-up list. Additional info can be supplied in the comments below.
3. **Run Type:** observing/chargeInjection/laser/pedestal/bias_curve/other/test; describing the type of run to be taken so the proper analysis can later be done on it. Options appear in a pop-up list. The additional options for defining chargeInjection runs are not supported, but the identifier should still be used to tag these runs, and parameters chosen from the separate QI GUI. Also, the “other” option should never be used, it confuses L3.
4. **Observing Mode:** on/off/tracking/survey/parked/drift/engineering/calibration/other; describes what specific type of run is being taken, so the analysis programs handle the data properly. Options appear in a pop-up list. For Observing runs, the only options are on/off/tracking/survey/parked/drift/other. For all other runs, the only options are engineering/calibration/other.
5. **Pointing Mode:** parallel/convergent/NA/other; describes where the telescope is pointing for the given run. Options appear in a pop-up list. For Observing runs, the only options are parallel/convergent/other. For all other runs, the only options are NA/other.
6. **Source:** source name from the known sources list. Options appear in a pop-up list. The source list can be edited by accessing the Database

subsystem.

7. **Trigger Config:** normal/external/muon/other; defines the current condition for the telescope to trigger. Options appear in a pop-up list.
8. **Trigger Multiplicity:** Number of telescopes needed for an array trigger.
9. **Trigger Coincidence:** Window width, in ns, to look for coincident events. Currently, for multiplicity 1, this is 0; for multiplicity > 1 , it is 100.
10. **Comments:** any number of comments can be added to each run to describe situations not covered in any other field. Comments may also be added later, during the run, or after its completion. This is done through the main window.
11. **Author:** author of the above comment. Each comment has an associated author, and must be added with the addition of each comment.
12. **Observers:** the observers for the new run. These must be entered as a comma-separated list (*i.e.* “SBH, MAO, KPK”, etc.) for the database to handle them properly. You are required to enter at least one observer before the run can be defined. A pop-up window will remind you of this fact if you try to declare the run without doing so.
13. **Duration:** length of the desired run. Separate minute and second fields allow for easier entry.
14. **Wobble:** Defines whether this is a wobble run or not. Sets appropriate offsetRA and offsetDEC in the run information, based on the source’s true RA and Dec, as well as offsetAngle and offsetDistance. Wobbles can be done in the default NSEW directions, or any arbitrary direction by entering any angle next to the radio button. The offset degrees should always be POSITIVE. If the previously defined run was a wobble run, the next time the Define Run panel is opened, the wobble offset will automatically be set to the same angle but opposite direction.
15. **Telescope Configuration:** Selects which telescopes will be a part of the new run. This is a graphical representation of the Config Mask Type. The number in the upper right is the mask value to be used and represents the scheme currently displayed graphically. Checked boxes mean the telescope is included.
16. **Start Run...:** Runs can be defined as either manual runs or auto runs. Manual runs are completely handled by the observer; auto runs are defined and started by *arrayctl*. When an auto run option is selected from the list, **Auto Run Type** is enabled, and the **Define + Prepare** option becomes **Define**. Auto runs are defined and prepared starting 1 minute before the requested start time. This allows the required initializations to complete and still begin the run on time.

- **Manually:** A manual run behaves as normal. It is defined and prepared immediately, and the user is left to start it when he/she sees fit.
- **Automatically; start run in...:** Runs can be started automatically a certain amount of time in the future. This is currently the best way to handle on/off runs (having the second run start 2 minutes after the first run finishes). The minimum offset time is 1 minute (to accommodate the necessary run preparations). However, setting the offset to 0 minutes (seconds are then ignored) will start the first auto run immediately after it is defined. When defining multiple auto runs, be advised the offsets are all relative to the time the runs are DEFINED and not relative to when the previous run finishes. Be sure to factor in the time needed to prepare the run into this offset time. It is recommended to have the offset times be at least 2 minutes longer than the previous run’s offset time plus run duration. If you are defining an ON/OFF pair, you don’t have to worry about these specifics.
- **Automatically; start run Today @:** You can request the run to start at a specific (UTC) time. The format for this time is hhmmss, and refers to the current day only. You cannot currently use the VAC to define runs for the following (or other future) UTC day. The time refers to the time on the `arrayctl` computer, so the observer should make sure that it is accurate.
- **Automatically; start run Later:** This option is useful for setting up ON–OFF or other auto run pairs without giving them a specific start time. The runs will be set up when you click Define, but the run timers will not start until you Activate the runs in the main window.
- **Auto Run Type:** For ease of observing, ON–OFF pairs can be auto-defined automatically. An unrelated series of runs can also be auto-defined automatically. This section determines which is the case, and how the auto runs are set up.
 - * **ON–OFF & OFF–ON:** An ON–OFF (or OFF–ON) run pair can now be automatically defined at once. The runs are offset in time by two minutes plus the duration chosen (a 28 minute duration yields two runs offset by 30 minutes, etc). The sequence starts according to the time offset or absolute time defined above. The second run will then be properly spaced in time to follow. The off run is given the correct RA offset in the database. The two runs are also grouped in the database as an “on/off” pair.
 - * **Unrelated:** Many auto runs can be defined simultaneously, and have no relation to ON–OFF pairs. This pop-up allows the user to review/change aspects of the many runs before the block is

defined as a whole. Selecting **Add new...** adds another auto run to the list, retaining by default all the run parameters currently displayed. If the “start set in...” offset times are used, each new run added will be given the minimum value required for it to not overlap with the previous run. It is not recommended that you decrease this value; the 2 minute time between runs is necessary to guarantee they do not cause conflict.

17. **Define** (auto runs only): Initializes the auto runs. The timers to auto-start the run(s) are initiated, and the runs are defined as necessary. If the run was not set to start immediately, it is defined and prepared 1 minute before it is scheduled to start.
18. **Define + Prepare** (manual runs only): Defines the currently described run in the database, and carries out the steps needed to prepare the run to be started. Preparing takes care of various tasks in the subsystems, to ensure the run will be ready to start when the **Start Run** button is clicked.

Once a run has been defined using the *VAC*, the next time you try to define a run, it will default to the values of the previous run. This makes it easier to do multiple identical runs, and so you don't have to reenter the observers each time you define a new run. However, if the GUI crashes or quits, the default run info is lost, and all information must be reentered for the next run defined. Also, auto-run information is not saved. Only the most recent run is listed individually, and auto-start options must be reselected.

- **Add Comment** Any number of comments may be added to each run, with an author associated with each comment. This can be done any time before, during, or after completion of the run. A run must be selected in the Run Information Table before you can add a comment; the selected run is the one to which the new comment is added.
- **End/Cancel Run** If circumstances require a run to be terminated before it has executed for its full duration, it can be ended manually. A run must be selected in the Run Information Table before you can do this; the selected run is the one ended. The user is asked for confirmation before the run actually ended. Auto runs can also be cancelled by clicking this button. If the auto run has already been defined, you must also click **End Run** for that run as well. Canceling the auto-run only disables the auto-starting of the run, not the run itself, if the run has already been defined.
- **Start/Activate Run** Tells *arrayctl* to start a given run. A run must be selected in the Run Information Table before you can do this; the selected run is the one started. The run will then execute for the prescribed duration, or until cancelled. While active, its status information will be automatically updated

in the Current Active Run section. Auto runs can be started early by choosing to Activate them at any point before they have automatically started.

Run Info for Current Active Run

When a run is in progress, its status is updated automatically and the results displayed in the Current Active Run section of the main window. Through the telescope listing, the observer can select which of multiple active runs they wish to view information for. When no run is in progress, all fields display “-1” and no times are listed on the progress bar.

Information is sampled every few seconds, and doesn’t always sync with *arrayctl* commands. Hence, when a run is started/stopped, it may take a couple seconds for the Run Info to reflect this. For an immediate update of status, choose **Update Status** button under **Observer** menu.

The error message like “updateRunTimes: arrayctlException: Statusmon exception: No status for run: Thrown in ac.cpp line 1041” is nothing to worry about. It just signifies that the *VAC* is trying to get the status of the run before enough events have been processed for the status to exist.

Eventually, QuickLook will be incorporated into this display and even more run information will be available.

- **Progress Bar**

The start and end times for the current run are displayed, along with a progress bar indicating how much of the run has completed. Listed below are the time elapsed and time remaining in the run, as well as the current run number.

- **Harvester**

Displays values for some aspects of Harvester activity. Currently, this includes the number of sane and insane events (as well as why if it was the telescope or L3 that caused them to be insane), the current size of the data file being written (in MB), the number of telescope events and L3 triggers recorded, and the telescope and L3 event rates (from QuickLook). The final two are an average over the last 10 bins of their respective rate vs. time histograms, and should start updating as soon as a run is PREPARED. The number in the name of the telescope-specific fields tells which telescope the statistics are for.

- **Event Builder**

Displays values for various aspects of Event Builder activity. These include telescope trigger rate, number of events to the harvester, number of events to disk, and number of bad events. The number following “Event Builder” tells which telescope the statistics are for.

- **Telescope**

Displays values from L2, acquired by L3. These include the L2 Rate and VDAQ Deadtime. The Deadtime is displayed as a percent; 100% means totally dead.

The number following “Telescope” tells which telescope the statistics are for. Information should appear as soon as a run is prepared.

- **L3**

Displays values from L3, including a string describing its status, the Array Deadtime, and L3 Rate. Deadtime is displayed as a percent; 100% means totally dead. Information should appear as soon as a run is prepared.

- **Run Info for Telescope...**

More than one run can currently be active in the system, yet *VAC* can only display info about one of them at a time. This pop-up list allows the user to select which run has its information displayed.

Since each telescope can only have one active run at a time, telescope number is used as a screening process for the active runs. In this way also, initial testing of operating two telescopes separately will not be overly confusing to the users. Selecting a telescope number from the list means that only runs in which that telescope is participating will be displayed in the Current Active Run panel. If **ALL** is selected, info will be displayed for the first run in the *arrayctl* internal run list only, and will change to the next one when that run has finished.

- **Open QL Displays**

Runs a script to open various QuickLook tools for the current run. This includes *ql_display* and *ql_monitor*. It is not yet available.

L2/L3 Rate Plot

This plot is a composite of individual telescope L2 rates and the L3 rate. All rate information comes from L3. Each curve appears as a separate color. Modifications will need to be made to handle multiple runs active at the same time.

Current issues are as follows:

1. The x-axis is only approximate time since the data was sampled.
2. The rate plot only updates when a run is active; the x-axis times become very inaccurate when the plot spans two runs.
3. Rate spikes can overwhelm autoscaling, making the plot useless until the spike is cleared.

- **Log10 Rate Axis**

Clicking this check box will change the scale on the y-axis to/from logarithmic. This makes the L3 rate easier to see when the L2 rate is very high.

- **Rescale Rates**

This button temporarily rescales the y-axis based on the most recent values added. It corrects the autoscaling that includes the rate spike. However, the

plot is autoscaled again on its next update. Soon there should be a more long-lasting way to rescale the axis.

- **Clear Plot**

This button zeros out the entire plot. Though annoying, it will at least remove rate spikes and make the plot easier to read.

C.2.2 Observer Menu

- **Start Subsystems**

Opens a separate window that can run various start-up scripts to handle many of the subsystems. You can choose a specific script from the pop-up menu, or click **Skip** to skip over a script you do not need to do. Clicking **Run Script** executes the current script. Items in the list such as “====Move to Desktop DACQ-T1====” require the observer to drag the scripts window to the specified desktop before continuing running the scripts. The button changes to **Changed Desktop** in this case so as not to confuse the observer into thinking this action will be completed for them.

The scripts list should be executed completely in order. The current tasks are as follows:

- T2_power_on_fadc_crates
- T3_power_on_fadc_crates
- T4_power_on_fadc_crates
- ====Move to Desktop DACQ-T1====
- start_fadc_vdaq 1
- make_evtbuilder_data_dir 1
- start_evtbuilder 1
- ====Move to Desktop DACQ-T2====
- start_fadc_vdaq 2
- make_evtbuilder_data_dir 2
- start_evtbuilder 2
- ====Move to Desktop DACQ-T3====
- start_fadc_vdaq 3
- make_evtbuilder_data_dir 3
- start_evtbuilder 3
- ====Move to Desktop DACQ-T4====
- start_fadc_vdaq 4

- `make_evtbuilder_data_dir` 4
 - `start_evtbuilder` 4
- **Start Night**

Should be called at the start of each observing night. Takes care of initializations needed for many of the subsystems (currently L3, Array Control, and EventBuilder). In the future, it will start more of the subsystems automatically.
- **End Night**

Should be called at the end of each observing night. Currently, it does a clean halt of L3, and lets Array Control do any nightly clean-up it needs to.
- **Read FADC Temperatures**

Temperature information is read automatically every few minutes. If instead you would like the temperatures immediately, selecting this item will do so and display all temperatures read. This can also be accomplished by pressing `Ctrl+T`.
- **Check Free Disk Space**

The Harvester, L3, Archive, and VDAQ machines are queried automatically for the total available disk space for data. Currently, results are simply listed in the main message window. If you would like to check the disk status immediately, you can select this item. This can also be accomplished by pressing `Ctrl+S`.
- **Update Status**

Choosing this item manually calls the update of all status information. This is usually handled automatically by a separate thread and shouldn't have to be called on its own. The update includes all System Status information, as well as info for the Current Active Run. This can also be accomplished by pressing `Ctrl+U`.
- **Define Run**

Opens the Define Run panel, same as the Define Run Button.
- **Prepare Run**

Runs must be both defined and prepared before they can be started. Preparing runs usually takes place automatically. If there is a problem with this, you may select this option to manually prepare a run. A run must be selected in the Run Information Table in order to do this; the selected run is the one that will be prepared.
- **Start/Activate Run**

Allows the observer to Start a prepared run or Activate an auto run. Same as the Start/Activate Run button. This can also be accomplished by pressing `Ctrl+A`.

- **End/Cancel Run**

Allows the observer to End an active run or Cancel an auto run. Same as the End/Cancel Run button. This can also be accomplished by pressing **Ctrl+K**.

- **Kill All Open Runs**

If you run into problems defining new runs and can't seem to figure out why, select this option. It goes through a variety of methods to try and clear ALL runs from ALL telescopes in the system, allowing you to start fresh again. The current methods it tries are: ending all active runs, ending all defined runs, ending all prepared runs and aborting those runs in L3, canceling all auto-runs, and manually entering the DB End Time for any remaining orphan active runs, as well as any active runs *arrayctl* no longer knows about.

- **Load Run List**

Loads the *arrayctl* internal run list and fills the Run Information Table below. If the table contains any runs (the list has already been loaded), this function will do nothing. Updates to the run list are done automatically, there should be no need to choose this item.

- **RE-load Run List**

Empties and reloads the Run Information Table. All runs listed are reloaded from the database to ensure their displayed parameters are accurate and up to date. This command does NOT clear the *arrayctl* internal run list.

- **Clear Old Runs**

Clears the *arrayctl* internal run list. Used when there are too many completed runs in the table for it to be useful. Should be called at the start of each night. While the internal run list is immediately cleared, it may take a second for the table to empty.

- **Run Information**

Brings up a new window showing all information in the database for a specific run (see Fig. C.3).

A run must be selected in the Run Information Table before you can do this; the selected run is the one whose information is displayed. Information for runs no longer in the Table can be accessed by changing the Run Number displayed here or through the Database Subsystem. The user can also add comments and observers to a given run through this window. This window can also be brought up by pressing **Ctrl+I**.

Through the Run Information window, the observer can alter aspects of a run in the database.

- **Add Comment**

As with the button in the main window, this allows the observer to add

The screenshot shows a window titled "Run Info" with a close button in the top right corner. The window contains several input fields and dropdown menus arranged in a grid-like fashion. The fields are as follows:

Run Number	11184	Run Status	manually_ended		
Weather	A-	Point Mode	parallel		
Run Type	observing	Observing Mode	wobble		
Trigger Config	normal	Source	Mrk421		
Trigger Multiplicity	2	RA Offset	0		
Trigger Coincidence	100	DEC Offset	0.00523599		
Config Mask Type	3	Wobble Angle	0	Distance	0.3

Below these fields is a large empty text area labeled "Comments". At the bottom of the window, there are several more fields and buttons:

Author		Observers	MAO, SBH,
DB Start Time	2007/01/05 22:17:19	Data Start Time	2007/01/05 22:17:39
DB End Time	2007/01/05 22:24:35	Data End Time	2007/01/05 22:24:33
Run Duration	28:00		

At the very bottom, there are four buttons: "Add Comment", "Add Observer", "Save New Info", and "Close".

FIGURE C.3: Layout of the Run Info window.

any number of comments (each with an associated author) to the run. This can be done any time before, during, or after completion of the run.

– **Add Observer**

Any number of observers may be added to each run. This can be done any time before, during, or after completion of the run. Defining a new run requires at least one observer to be listed. You should add only one observer at a time here for it to be properly entered into the database.

– **Save New Info**

The observer is allowed to change some other aspects of a run's information in the database, in case an error was made in defining that run. Weather, run type, pointing mode, trigger config, source, RA/DEC offsets, wobble offset, and wobble angle can all be changed. Clicking this button commits those changes to the database. If changes are made to any run, it is updated in the Run Information Table in the main window.

• **Add Comment**

Allows observers to add comments to any run in the Run Info Table without having to first open the Run Info window.

C.2.3 Test Runs Menu

For debugging and when things just won't work correctly, these shortcuts can be used to start a run without having to define all the necessary info. When chosen, a run is automatically defined, prepared and immediately started. It is tagged as a 5 minute chargeInjection engineering run, parked, with C- weather, and a default observer. Which telescopes are involved depends on which option is chosen. Options appear as separate menu items to make starting a test run as effortless as possible.

• **Make Test Run (ALL)**

Configures and starts a test run on ALL telescopes in the current system. As a shortcut, use **Ctrl+M**.

• **Make Test Run T1**

Configures and starts a test run on Telescope 1. As a shortcut, use **Ctrl+1**.

• **Make Test Run T2**

Configures and starts a test run on Telescope 2. As a shortcut, use **Ctrl+2**.

• **Make Test Run T3**

Configures and starts a test run on Telescope 3. As a shortcut, use **Ctrl+3**.

• **Make Test Run T4**

Configures and starts a test run on Telescope 4. As a shortcut, use **Ctrl+4**.

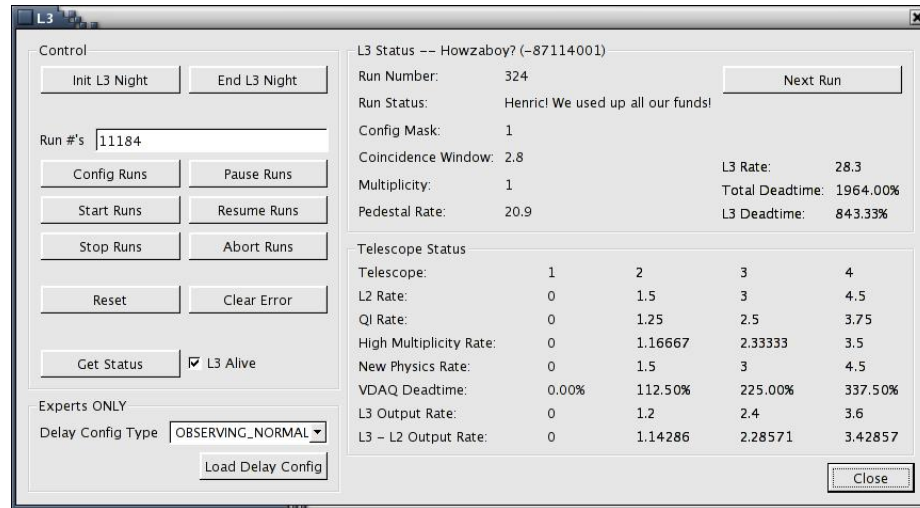


FIGURE C.4: Layout of the L3 subsystem window.

C.2.4 Subsystems Menu

L3 Subsystem

The L3 subsystem window is shown in Figure C.4.

- **Init L3 Night**

Initializes the night for L3. This is called as part of **Start Night** from the main window, but is here for when it must be called separately, when L3 is brought back online after a problem, for example.

- **End L3 Night**

Concludes the night for L3. This is called as part of **End Night** from the main window, but is here for when it must be called separately, when L3 is brought back online after a problem, for example.

- **Run #'s**

The run number used when a run-specific command is selected. If a run is selected in the main Run Information Table, it becomes the default run number. Multiple runs can be entered, as long as they are separated by a space. No other punctuation is allowed.

- **Config Runs**

Configures specific runs within L3. The run number(s) listed above the button is used.

- **Start Runs**
Start specific runs within L3. The run number(s) listed above the button is used.
- **End Runs**
Terminate specific runs within L3. The run number(s) listed above the button is used.
- **Pause Runs**
Pauses specific runs within L3. The run number(s) listed above the button is used.
- **Resume Runs**
Resumes specific runs within L3. The run number(s) listed above the button is used.
- **Abort Runs**
Aborts specific runs within L3. The run number(s) listed above the button is used.
- **Reset**
Does a soft reset of L3.
- **Clear Error**
Clears L3 of error status.
- **Get Status**
Displays the status of L3. The status items are described below.
- **L3 Alive**
Identical to the indicator in the main window, it tells if L3 is connected to *arrayctl*. It is only updated when the user clicks **Get Status**.
- **L3 Status**
The box's title contains both a string describing the current L3 Status, and a number referring to the L3 Status Bits.
The other items in the box are self-explanatory: run number, run status, config. mask, coincidence window, multiplicity, pedestal rate, L3 rate, Total deadtime, and L3 deadtime.
Clicking the **Next Run** button displays the information for the a different run currently known to L3. The button is greyed when there are less than two runs present. If no runs are present, all values are -1 .
- **Telescope Status**
The status items displayed are as follows: telescope ID, L2 rate, QI rate, high multiplicity rate, new physics rate, VDAQ deadtime, L3 output rate, and L3-L2 output rate.



FIGURE C.5: Layout of the Harvester subsystem window.

- **Close**
Closes the L3 dialog box and returns to the main window.

Harvester Subsystem

The Harvester subsystem window is shown in Figure C.5.

- **Run #**
The run number used when a run-specific command is selected. If a run is selected in the main Run Information Table, it becomes the default run number.
- **Start Harvest Run**
Starts a run in the harvester. The run number is taken from the input line above.
- **End Harvest Run**
Ends a run in the harvester. The run number is taken from the input line above.
- **Roll Back Run**
Roll back a run in the harvester. The run number is taken from the input line above.
- **Start Harvest Night**
Starts the night for the harvester, initializing internal routines.

- **End Harvest Night**
Ends the night for the harvester.
- **Close**
Closes the Harvester dialog box and returns to the main window.

Event Builder Subsystem

The Event Builder subsystem window is shown in Figure C.6.

- **Telescope**
The telescope used when a run-specific command is selected. Numbering is 1–4, however some errors may still report with the old 0 – 3 numbering scheme.
- **Run #**
The run number used when a run-specific command is selected. If a run is selected in the main Run Information Table, it becomes the default run number.
- **EVTB Start Run**
Instructs the event builder to start a given run. The run number and telescope number are taken from the input lines above.
- **EVTB End Run**
Terminates the current run on a given telescope. The telescope number is taken from the input line above. The status of the run is then updated. This status includes telescope trigger rate, number of bad events, number of events to the harvester, and number of events written to disk.
- **Get EVTB Status**
Gets the event builder status for a given telescope. The telescope number is taken from the input line above. The status includes telescope trigger rate, number of bad events, number of events to the harvester, and number of events written to disk. This function is called automatically when the dialog is first opened.
- **Active EVTB Runs?**
Sees if a run is currently active on a given telescope. Status for 4 telescopes is given. This function is called automatically when the dialog is first opened.
- **VEventSeq**
Gets the VEventSeq for a given telescope. It displays **nwords** for 4 telescopes. This function is called automatically when the dialog is first opened.
- **Kill ALL VDAQ/DACQ**
This button will kill any active vdaq or dacq processes for the telescope chosen at the top of the dialog box. This is useful after doing bias curves to ensure everything is cleaned up and ready to take normal data again.

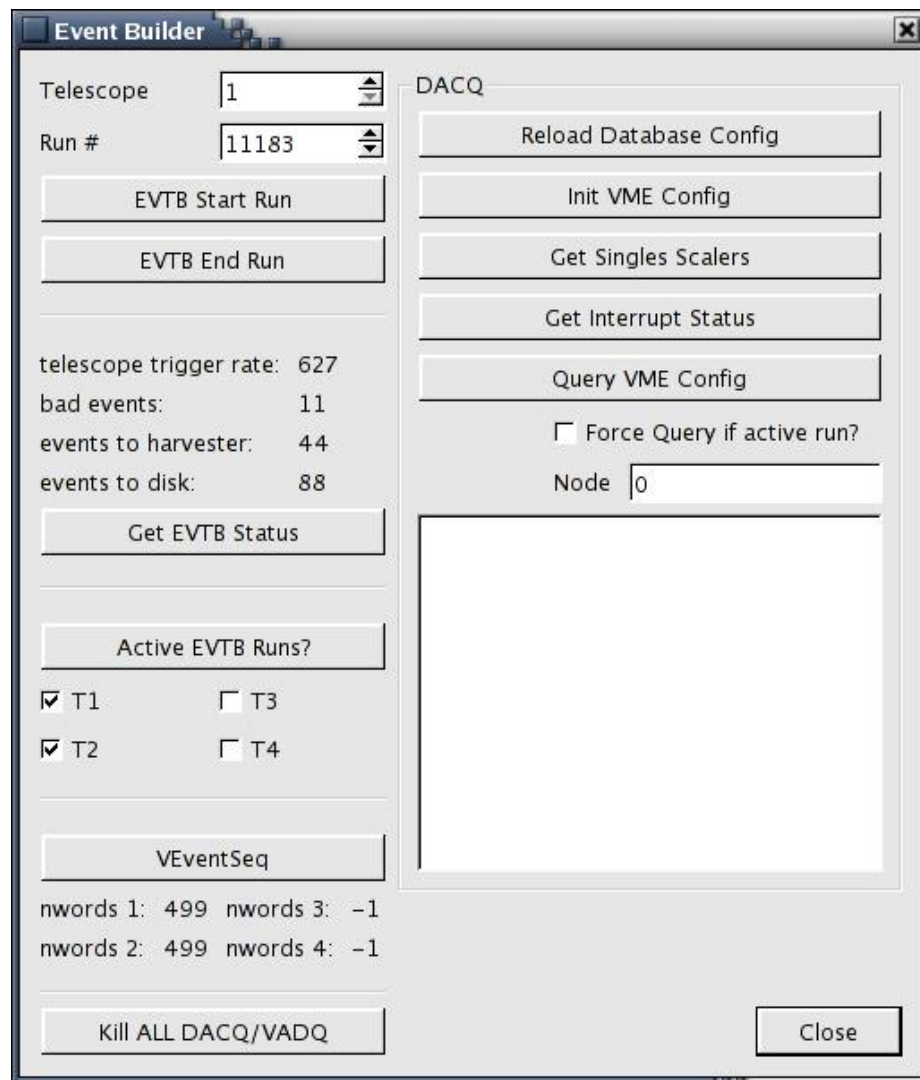


FIGURE C.6: Layout of the Event Builder subsystem window.

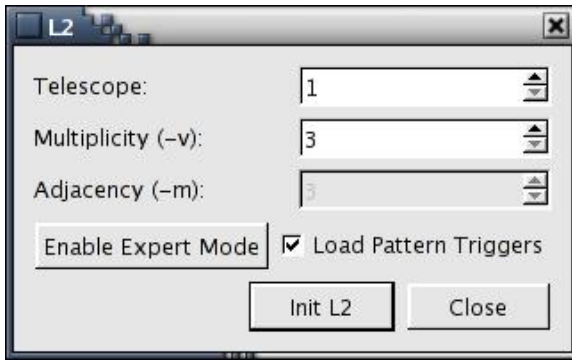


FIGURE C.7: Layout of the L2 subsystem window.

- **DACQ**

Contains a new set of buttons to control the VME-DACQ systems through the Event Builder.

- **Reload Database Config**

Reload the configurations info from the database. **InitVME** should be called after this before a new run is started.

- **Init VME Config**

Initializes VME system, and propogates through any newly reloaded database configurations.

- **Get Singles Scalars**

Gets the Singles Rates on the current telescope. Results are displayed below.

- **Get Interrupt Status**

Gets the interrupt status on the current telescope. Results are displayed below.

- **Query VME Config**

Also self-descriptive. If the Force Query box is checked, the call will be made even if a run is active. This will adversely effect the current run. The query is made of the node listed.

- **Close**

Closes the Event Builder dialog box and returns to the main window.

L2 Subsystem

The L2 subsystem window is shown in Figure C.7.

- **Telescope**

Set which telescope's L2 you wish to deal with

- **Multiplicity**

Choose 3-fold or 4-fold multiplicity.

- **Load Pattern Triggers**

Check this box if the pattern triggers need to be reloaded. Leave unchecked if you simply are resetting L2.

- **Init L2**

Runs the L2 script with the above options. Also makes sure *ecc_host* is running.

- **Enable Expert Mode**

You should only use this if you really know what you are doing. Clicking this button enables the Adjacency option. It also allows for any combination (1 – 5) for Multiplicity and Adjacency, as long as $\text{Multiplicity} \geq \text{Adjacency}$. For clarity, Multiplicity defines how many pixels must have CFD triggers in order for a patch to trigger. Adjacency defines how many pixels must be NEXT to each other for a patch to fire.

L1 Subsystem

Currently not supported, will be used to display L1 rates for each telescope.

Database Subsystem

The Database subsystem window is shown in Figure C.8.

- **Source Info**

If the source you want to observe is not in the source list, you can add it here. Simply type in the new source's name, RA, Dec, and Epoc, and then click **New Source** to confirm the addition. Note: RA and Dec are in RADIANS! To easily convert from hhmmss and ddmms to radians, you can use the program *RADEC2rad* located on the `arrayct1` computer under `/home/observer/shughes/RADEC2rad`.

- **Source**

Lists all sources currently in the database in a pop-up list. Selecting one brings up its corresponding information in the fields below.

- **New Source Name**

Re-lists the source name chosen from the above list, so the source info can be edited. Or, the user may type in a new name to add a new source to the database

- **RA/Dec/Epoch**

Right Ascension, Declination, and Epoch of the source currently described

- **Description**

A brief description of the source can be added to its database entry.

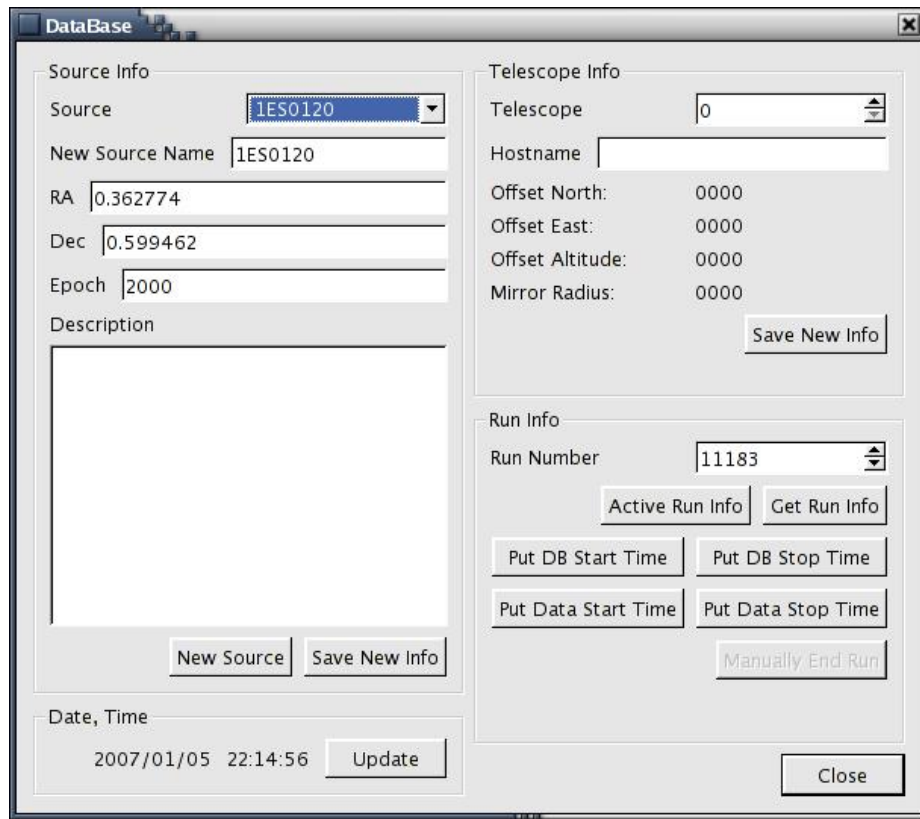


FIGURE C.8: Layout of the Database subsystem window.

- **New Source**
Click to add a new source entry to the database. The values of the above fields are all used.
- **Save New Info**
If you are altering the description or position of an existing source, clicking here will update its information in the database. For this to work, you must not change the New Source Name from its original value.
- **Date, Time**
 - **Date & Time**
Current date and time from the database when the dialog box was opened.
 - **Update**
Click to update the date and time from the database at any point.
- **Telescope Info**
 - **Telescope**
Select the telescope number for which you would like information. The telescope's hostname, north and east offsets from the array center, altitude, and mirror radius are displayed.
 - **Hostname**
Hostname of the above chosen telescope.
 - **Offset North/Offset East/Offset Altitude/Mirror Radius**
Position, etc., of the above telescope.
 - **Save New Info**
Saves the current telescope number and hostname, associating the two with each other in the database.
- **Run Info**
 - **Run Number**
Enter the run number for which you would like to access database information.
 - **Active Run Info**
Opens a new window displaying all the database information for the current active run. If more than one run is active, information will be displayed one run at a time. Clicking the Close button will bring up the info for the next run.
 - **Get Run Info**
Opens a new window with all the database information for the run number entered above. If the run does not exist, most of the info will be left blank.

Run info can be altered in the database in this fashion. However, it is not recommended you use this method for runs currently listed in the main Run Info Table. They can be modified by choosing **Run Info** from the main window, through the **Observer** menu.

- **Put DB Start Time**
Manually enter the current date/time in the DB Start Time field for the run number listed above.
- **Put DB Stop Time**
Manually enter the current date/time in the DB Stop Time field for the run number listed above. This causes the database to end the given run.
- **Put Data Start Time**
Manually enter the current date/time in the Data Start Time field for the run number listed above.
- **Put Data Stop Time**
Manually enter the current date/time in the Data Stop Time field for the run number listed above.

Charge Injection (QI) Subsystem

This subsystem is currently unsupported.

Custom Night

For debugging purposes, each part of Start/End Night can be called individually, or in custom groupings. The window for handling this is shown in Figure C.9.

Start Night and End Night appear as separate tabs, each listing the functions specific to each procedure. Regardless of which items are checked in the other tab, only the items in the visible tab will be executed when **Do Night** is chosen. The items are grouped by subsystem.

- **Start Night**

- **L3**
Init Night calls L3's own night initialization routine.
- **Eventbuilder**
Init VME Config initializes the system for each telescope listed. If settings from the database have changed, they are reloaded.
- **Arrayctl**
Start Night performs Array Control-specific initialization items. Clear Internal Run List removes old, completed runs from the Run Information Table seen in *VAC*.

- **End Night**

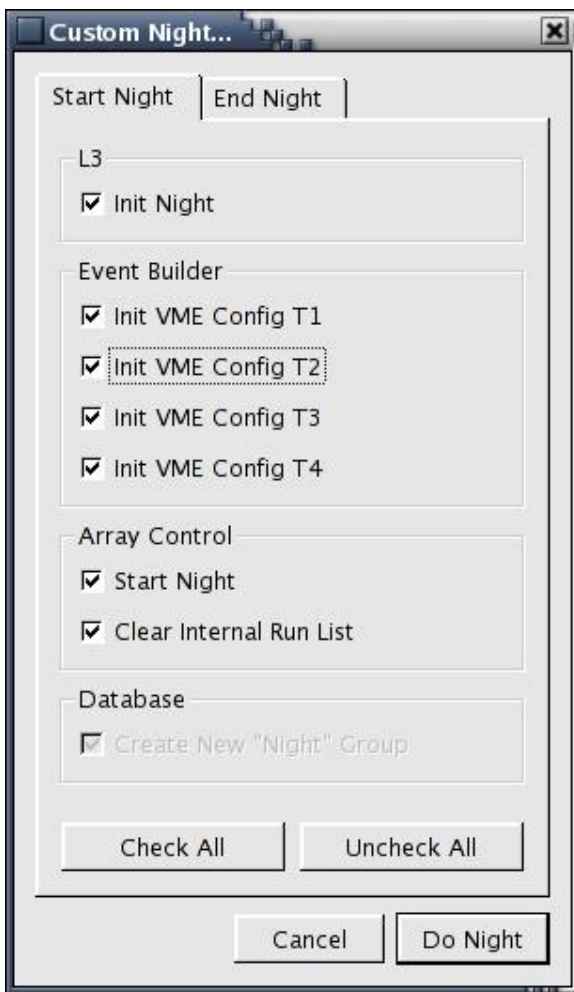


FIGURE C.9: Layout of the Custom Night window.

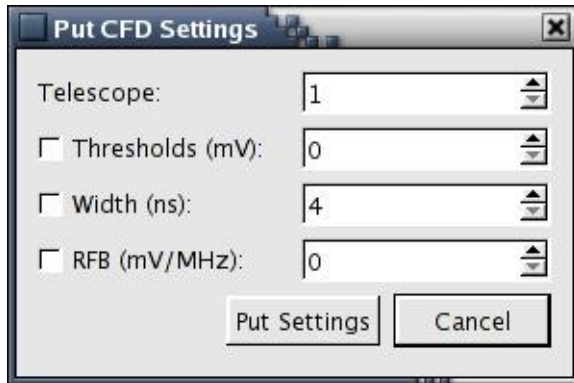


FIGURE C.10: Layout of the Put CFD Settings window.

- **L3**
Quit L3 safely terminates the L3 system.
- **Arrayctl**
End Night performs Array Control-specific nightly clean-up items.
- **Check All/Uncheck All**
For easier handling of a large number of separate steps, these buttons select or deselect all of the above options, regardless of their current state.
- **Do Night**
Sequentially carries out the selected items in the currently visible tab. If a problem occurs in the process, it may be aborted, and the later items will not be completed as requested.

C.2.5 Settings Menu

Various settings used by the Event Builder are stored in the database. These settings effect the CFDs and FADCs. The Settings menu contains interfaces to alter both sets of settings, change the current configuration, and load/save the settings to a file.

Note: The CFD and FADC Settings are not yet complete and should not be used. Doing so may adversely effect the system or the database records.

Put CFD Settings

The Put CFD Settings window is shown in Figure C.10. This panel will run Liz's *vdbput_CFDSettings* script with various options.

- **Telescope**
Choose which telescope you are changing the settings for (1-4).

- **Threshold**

If this box is checked, thresholds will be changed to the value listed. Note, entering a POSITIVE number will yield a NEGATIVE mV setting (i.e. Threshold = 100 → set to -100 mV).

- **Width**

If this box is checked, widths will be changed to the value listed (4 – 25 ns).

- **RFB**

If this box is checked, RFB's will be changed to the value listed (0–127mV/MHz).

- **Put Settings**

Runs the script with the above options in a new terminal window. It will also tell VDAQ to reload the settings from the DB. When it has finished, you may close the window and put settings for another telescope.

- **Cancel**

Does nothing, closes the window.

CFD Settings

This section is currently unsupported.

FADC Settings

This section is currently unsupported.

Bibliography

Aharonian, F., Akhperjanian, A., Beilicke, M., Bernlöhr, K., Börst, H.-G., Bojahr, H., Bolz, O., Coarasa, T., Contreras, J. L., Cortina, J., Denninghoff, S., Fonseca, M. V., Girma, M., Götting, N., Heinzelmann, G., Hermann, G., Heusler, A., Hofmann, W., Horns, D., Jung, I., Kankanyan, R., Kestel, M., Kohnle, A., Konopelko, A., Kornmeyer, H., Kranich, D., Lampeitl, H., Lopez, M., Lorenz, E., Lucarelli, F., Mang, O., Meyer, H., Mirzoyan, R., Moralejo, A., Ona-Wilhelmi, E., Panter, M., Plyasheshnikov, A., Pühlhofer, G., de los Reyes, R., Rhode, W., Ripken, J., Rowell, G., Sahakian, V., Samorski, M., Schilling, M., Siems, M., Sobzynska, D., Stamm, W., Tluczykont, M., Vitale, V., Völk, H. J., Wiedner, C. A., and Wittek, W.: 2003, *Astronomy and Astrophysics* **403**, L1

Aharonian, F., Akhperjanian, A. G., Aye, K.-M., Bazer-Bachi, A. R., Beilicke, M., Benbow, W., Berge, D., Berghaus, P., Bernlöhr, K., Boisson, C., Bolz, O., Braun, I., Breitling, F., Brown, A. M., Bussons Gordo, J., Chadwick, P. M., Chounet, L.-M., Cornils, R., Costamante, L., Degrange, B., Djannati-Ataï, A., O’C. Drury, L., Dubus, G., Emmanoulopoulos, D., Espigat, P., Feinstein, F., Fleury, P., Fontaine, G., Fuchs, Y., Funk, S., Gallant, Y. A., Giebels, B., Gillessen, S., Glicenstein, J. F., Goret, P., Hadjichristidis, C., Hauser, M., Heinzelmann, G., Henri, G., Hermann, G., Hinton, J. A., Hofmann, W., Holleran, M., Horns, D., de Jager, O. C., Khélifi, B., Komin, N., Konopelko, A., Latham, I. J., Le Gallou, R., Lemièrre, A., Lemoine-Goumard, M., Leroy, N., Lohse, T., Martineau-Huynh, O., Marcowith, A., Masterson, C., McComb, T. J. L., de Naurois, M., Nolan, S. J., Noutsos, A., Orford, K. J., Osborne, J. L., Ouchrif, M., Panter, M., Pelletier, G., Pita, S., Pühlhofer, G., Punch, M., Raubenheimer, B. C., Raue, M., Raux, J., Rayner, S. M., Redondo, I., Reimer, A., Reimer, O., Ripken, J., Rob, L., Rolland, L., Rowell, G., Sahakian, V., Saugé, L., Schlenker, S., Schlickeiser, R., Schuster, C., Schwanke, U., Siewert, M., Sol, H., Steenkamp, R., Stegmann, C., Tavernet, J.-P., Terrier, R., Théoret, C. G., Tluczykont, M., Vasileiadis, G., Venter, C., Vincent, P., Völk, H. J., and Wagner, S. J.: 2005a, *Astronomy and Astrophysics* **436**, L17

Aharonian, F., Akhperjanian, A. G., Aye, K.-M., Bazer-Bachi, A. R., Beilicke, M., Benbow, W., Berge, D., Berghaus, P., Bernlöhr, K., Boisson, C., Bolz, O., Braun, I., Breitling, F., Brown, A. M., Bussons Gordo, J., Chadwick, P. M., Chounet, L.-M., Cornils, R., Costamante, L., Degrange, B., Djannati-Ataï, A., O’C. Drury, L., Dubus, G., Emmanoulopoulos, D., Espigat, P., Feinstein, F., Fleury, P., Fontaine,

- G., Fuchs, Y., Funk, S., Gallant, Y. A., Giebels, B., Gillessen, S., Glicenstein, J. F., Goret, P., Hadjichristidis, C., Hauser, M., Heinzelmann, G., Henri, G., Hermann, G., Hinton, J. A., Hofmann, W., Holleran, M., Horns, D., de Jager, O. C., Johnston, S., Khélifi, B., Kirk, J. G., Komin, N., Konopelko, A., Latham, I. J., Le Gallou, R., Lemièrre, A., Lemoine-Goumard, M., Leroy, N., Martineau-Huynh, O., Lohse, T., Marcowith, A., Masterson, C., McComb, T. J. L., de Naurois, M., Nolan, S. J., Noutsos, A., Orford, K. J., Osborne, J. L., Ouchrif, M., Panter, M., Pelletier, G., Pita, S., Pühlhofer, G., Punch, M., Raubenheimer, B. C., Raue, M., Raux, J., Rayner, S. M., Redondo, I., Reimer, A., Reimer, O., Ripken, J., Rob, L., Rolland, L., Rowell, G., Sahakian, V., Saugé, L., Schlenker, S., Schlickeiser, R., Schuster, C., Schwanke, U., Siewert, M., Skjæraasen, O., Sol, H., Steenkamp, R., Stegmann, C., Tavernet, J.-P., Terrier, R., Théoret, C. G., Tluczykont, M., Vasileiadis, G., Venter, C., Vincent, P., Völk, H. J., and Wagner, S. J.: 2005b, *Astronomy and Astrophysics* **442**, 1
- Aharonian, F., Akhperjanian, A. G., Aye, K.-M., Bazer-Bachi, A. R., Beilicke, M., Benbow, W., Berge, D., Berghaus, P., Bernlöhr, K., Boisson, C., Bolz, O., Braun, I., Breitling, F., Brown, A. M., Bussons Gordo, J., Chadwick, P. M., Chounet, L.-M., Cornils, R., Costamante, L., Degrange, B., Djannati-Ataï, A., O’C. Drury, L., Dubus, G., Emmanoulopoulos, D., Espigat, P., Feinstein, F., Fleury, P., Fontaine, G., Fuchs, Y., Funk, S., Gallant, Y. A., Giebels, B., Gillessen, S., Glicenstein, J. F., Goret, P., Hadjichristidis, C., Hauser, M., Heinzelmann, G., Henri, G., Hermann, G., Hinton, J. A., Hofmann, W., Holleran, M., Horns, D., de Jager, O. C., Khélifi, B., Komin, N., Konopelko, A., Latham, I. J., Le Gallou, R., Lemièrre, A., Lemoine, M., Leroy, N., Lohse, T., Marcowith, A., Masterson, C., McComb, T. J. L., de Naurois, M., Nolan, S. J., Noutsos, A., Orford, K. J., Osborne, J. L., Ouchrif, M., Panter, M., Pelletier, G., Pita, S., Pühlhofer, G., Punch, M., Raubenheimer, B. C., Raue, M., Raux, J., Rayner, S. M., Redondo, I., Reimer, A., Reimer, O., Ripken, J., Rob, L., Rolland, L., Rowell, G., Sahakian, V., Saugé, L., Schlenker, S., Schlickeiser, R., Schuster, C., Schwanke, U., Siewert, M., Sol, H., Steenkamp, R., Stegmann, C., Tavernet, J.-P., Terrier, R., Théoret, C. G., Tluczykont, M., Vasileiadis, G., Venter, C., Vincent, P., Völk, H. J., and Wagner, S. J.: 2005c, *Astronomy and Astrophysics* **437**, 95
- Aharonian, F., Akhperjanian, A. G., Bazer-Bachi, A. R., Beilicke, M., Benbow, W., Berge, D., Bernlöhr, K., Boisson, C., Bolz, O., Borrel, V., Braun, I., Breitling, F., Brown, A. M., Chadwick, P. M., Chounet, L.-M., Cornils, R., Costamante, L., Degrange, B., Dickinson, H. J., Djannati-Ataï, A., O’C. Drury, L., Dubus, G., Emmanoulopoulos, D., Espigat, P., Feinstein, F., Fontaine, G., Fuchs, Y., Funk, S., Gallant, Y. A., Giebels, B., Gillessen, S., Glicenstein, J. F., Goret, P., Hadjichristidis, C., Hauser, M., Heinzelmann, G., Henri, G., Hermann, G., Hinton, J. A., Hofmann, W., Holleran, M., Horns, D., Jacholkowska, A., de Jager, O. C., Khélifi, B., Komin, N., Konopelko, A., Latham, I. J., Le Gallou, R., Lemièrre, A., Lemoine-Goumard, M., Leroy, N., Lohse, T., Martin, J. M., Martineau-Huynh, O.,

- Marcowith, A., Masterson, C., McComb, T. J. L., de Naurois, M., Nolan, S. J., Noutsos, A., Orford, K. J., Osborne, J. L., Ouchrif, M., Panter, M., Pelletier, G., Pita, S., Pühlhofer, G., Punch, M., Raubenheimer, B. C., Raue, M., Raux, J., Rayner, S. M., Reimer, A., Reimer, O., Ripken, J., Rob, L., Rolland, L., Rowell, G., Sahakian, V., Saugé, L., Schlenker, S., Schlickeiser, R., Schuster, C., Schwanke, U., Siewert, M., Sol, H., Spangler, D., Steenkamp, R., Stegmann, C., Tavernet, J.-P., Terrier, R., Théoret, C. G., Tluczykont, M., Vasileiadis, G., Venter, C., Vincent, P., Völk, H. J., and Wagner, S. J.: 2005d, *Astronomy and Astrophysics* **441**, 465
- Aharonian, F., Akhperjanian, A. G., Bazer-Bachi, A. R., Beilicke, M., Benbow, W., Berge, D., Bernlöhr, K., Boisson, C., Bolz, O., Borrel, V., Braun, I., Brown, A. M., Bühler, R., Büsching, I., Carrigan, S., Chadwick, P. M., Chounet, L.-M., Coignet, G., Cornils, R., Costamante, L., Degrange, B., Dickinson, H. J., Djannati-Ataï, A., Drury, L. O., Dubus, G., Egberts, K., Emmanoulopoulos, D., Espigat, P., Feinstein, F., Ferrero, E., Fiasson, A., Fontaine, G., Funk, S., Funk, S., Füßling, M., Gallant, Y. A., Giebels, B., Glicenstein, J. F., Goret, P., Hadjichristidis, C., Hauser, D., Hauser, M., Heinzlmann, G., Henri, G., Hermann, G., Hinton, J. A., Hoffmann, A., Hofmann, W., Holleran, M., Hoppe, S., Horns, D., Jacholkowska, A., de Jager, O. C., Kendziorra, E., Kerschhaggl, M., Khélifi, B., Komin, N., Konopelko, A., Kosack, K., Lamanna, G., Latham, I. J., Le Gallou, R., Lemièrre, A., Lemoine-Goumard, M., Lenain, J.-P., Lohse, T., Martin, J. M., Martineau-Huynh, O., Marcowith, A., Masterson, C., Maurin, G., McComb, T. J. L., Moulin, E., de Naurois, M., Nedbal, D., Nolan, S. J., Noutsos, A., Orford, K. J., Osborne, J. L., Ouchrif, M., Panter, M., Pelletier, G., Pita, S., Pühlhofer, G., Punch, M., Ranchon, S., Raubenheimer, B. C., Raue, M., Rayner, S. M., Reimer, A., Ripken, J., Rob, L., Rolland, L., Rosier-Lees, S., Rowell, G., Sahakian, V., Santangelo, A., Saugé, L., Schlenker, S., Schlickeiser, R., Schröder, R., Schwanke, U., Schwarzbürg, S., Schwemmer, S., Shalchi, A., Sol, H., Spangler, D., Spanier, F., Steenkamp, R., Stegmann, C., Superina, G., Tam, P. H., Tavernet, J.-P., Terrier, R., Tluczykont, M., van Eldik, C., Vasileiadis, G., Venter, C., Vialle, J. P., Vincent, P., Völk, H. J., Wagner, S. J., and Ward, M.: 2006, *Science* **314**, 1424
- Aharonian, F. A., Akhperjanian, A. G., Andronache, M., Barrio, J. A., Bernlöhr, K., Bojahr, H., Calle, I., Contreras, J. L., Cortina, J., Daum, A., Deckers, T., Denninghoff, S., Fonseca, V., Gonzalez, J. C., Götting, N., Heinzlmann, G., Hemberger, M., Hermann, G., Heß, M., Heusler, A., Hofmann, W., Hohl, H., Horns, D., Ibarra, A., Kankanyan, R., Kettler, J., Köhler, C., Konopelko, A., Kornmeyer, H., Kestel, M., Kranich, D., Krawczynski, H., Lampeitl, H., Lindner, A., Lorenz, E., Magnussen, N., Mang, O., Meyer, H., Mirzoyan, R., Moralejo, A., Padilla, L., Panter, M., Petry, D., Plaga, R., Plyasheshnikov, A., Prahl, J., Pühlhofer, G., Rauterberg, G., Renault, C., Rhode, W., Röhring, A., Sahakian, V., Samorski, M., Schilling, M., Schröder, F., Stamm, W., Völk, H. J., Wiebel-Sooth, B., Wiedner, C., Willmer, M., and Wittek, W.: 1999, *Astronomy and Astrophysics* **350**, 757

- Aharonian, F. A., Hofmann, W., Konopelko, A. K., and Völk, H. J.: 1997, *Astroparticle Physics* **6**, 343
- Albert, J., Aliu, E., Anderhub, H., Antoranz, P., Armada, A., Asensio, M., Baixeras, C., Barrio, J. A., Bartelt, M., Bartko, H., Bastieri, D., Bavikadi, S. R., Bednarek, W., Berger, K., Bigongiari, C., Biland, A., Bisesi, E., Bock, R. K., Bordas, P., Bosch-Ramon, V., Bretz, T., Britvitch, I., Camara, M., Carmona, E., Chilingarian, A., Ciprini, S., Coarasa, J. A., Commichau, S., Contreras, J. L., Cortina, J., Curtef, V., Danielyan, V., Dazzi, F., De Angelis, A., de los Reyes, R., De Lotto, B., Domingo-Santamaría, E., Dorner, D., Doro, M., Errando, M., Fagiolini, M., Ferenc, D., Fernández, E., Firpo, R., Flix, J., Fonseca, M. V., Font, L., Fuchs, M., Galante, N., Garczarczyk, M., Gaug, M., Giller, M., Goebel, F., Hakobyan, D., Hayashida, M., Hengstebeck, T., Höhne, D., Hose, J., Hsu, C. C., Isar, P. G., Jaco, P., Kalekin, O., Kosyra, R., Kranich, D., Laatiaoui, M., Laille, A., Lenisa, T., Liebing, P., Lindfors, E., Lombardi, S., Longo, F., López, J., López, M., Lorenz, E., Lucarelli, F., Majumdar, P., Maneva, G., Mannheim, K., Mansutti, O., Mariotti, M., Martínez, M., Mase, K., Mazin, D., Merck, C., Meucci, M., Meyer, M., Miranda, J. M., Mirzoyan, R., Mizobuchi, S., Moralejo, A., Nilsson, K., Oña-Wilhelmi, E., Orduña, R., Otte, N., Oya, I., Paneque, D., Paoletti, R., Paredes, J. M., Pasanen, M., Pascoli, D., Paus, F., Pavel, N., Pegna, R., Persic, M., Peruzzo, L., Piccioli, A., Poller, M., Pooley, G., Prandini, E., Raymers, A., Rhode, W., Ribó, M., Rico, J., Riegel, B., Rissi, M., Robert, A., Romero, G. E., Rügamer, S., Saggion, A., Sánchez, A., Sartori, P., Scalzotto, V., Scapin, V., Schmitt, R., Schweizer, T., Shayduk, M., Shinozaki, K., Shore, S. N., Sidro, N., Sillanpää, A., Sobczynska, D., Stamerra, A., Stark, L. S., Takalo, L., Temnikov, P., Tesaro, D., Teshima, M., Tonello, N., Torres, A., Torres, D. F., Turini, N., Vankov, H., Vitale, V., Wagner, R. M., Wibig, T., Wittek, W., Zanin, R., and Zapatero, J.: 2006, *Science* **312**, 1771
- Baixeras, C. and et al.: 2005, in *International Cosmic Ray Conference*, pp 227–+
- Barrau, A., Bazer-Bachi, R., Beyer, E., Cabot, H., Cerutti, M., Chounet, L. M., Debais, G., Degrange, B., Delchini, H., Denance, J. P., Descotes, G., Dezalay, J. P., Djannati-Atai, A., Dumora, D., Espigat, P., Fabre, B., Fleury, P., Fontaine, G., George, R., Ghesquiere, C., Gilly, J., Goret, P., Gouiffes, C., Gouillaud, J. C., Gregory, C., Grenier, I. A., Iacoucci, L., Kalt, L., Le Bohec, S., Malet, I., Meynadier, C., Mols, J. P., Mora de Freitas, P., Morano, R., Morinaud, G., Munz, F., Palatka, M., Palfrey, T. A., Pare, E., Pons, Y., Punch, M., Quebert, J., Ragan, K., Renault, C., Rivoal, M., Rob, L., Schovanek, P., Smith, D., Tabary, A., Tavernet, J. P., Toussenel, F., and Vrana, J.: 1998, *ArXiv Astrophysics e-prints*, astro-ph/9804046
- Bednarek, W.: 1997, *MNRAS* **285**, 69
- Bednarek, W. and Protheroe, R. J.: 1999, *MNRAS* **310**, 577

- Blandford, R. D. and Rees, M. J.: 1978, in A. M. Wolfe (ed.), *Pittsburgh Conference on BL Lac Objects, Pittsburgh, Pa., April 24-26, 1978, Proceedings. (A79-30026 11-90) Pittsburgh, Pa., University of Pittsburgh, 1978, p. 328-341; Discussion, p. 341-347. NATO-supported research*, pp 328–341
- Błażejowski, M., Blaylock, G., Bond, I. H., Bradbury, S. M., Buckley, J. H., Carter-Lewis, D. A., Celik, O., Cogan, P., Cui, W., Daniel, M., Duke, C., Falcone, A., Fegan, D. J., Fegan, S. J., Finley, J. P., Fortson, L., Gammell, S., Gibbs, K., Gillanders, G. G., Grube, J., Gutierrez, K., Hall, J., Hanna, D., Holder, J., Horan, D., Humensky, B., Kenny, G., Kertzman, M., Kieda, D., Kildea, J., Knapp, J., Kosack, K., Krawczynski, H., Krennrich, F., Lang, M., LeBohec, S., Linton, E., Lloyd-Evans, J., Maier, G., Mendoza, D., Milovanovic, A., Moriarty, P., Nagai, T. N., Ong, R. A., Power-Mooney, B., Quinn, J., Quinn, M., Ragan, K., Reynolds, P. T., Rebillot, P., Rose, H. J., Schroedter, M., Sembroski, G. H., Swordy, S. P., Syson, A., Valcarel, L., Vassiliev, V. V., Wakely, S. P., Walker, G., Weekes, T. C., White, R., Zweerink, J., Mochejska, B., Smith, B., Aller, M., Aller, H., Teräsranata, H., Boltwood, P., Sadun, A., Stanek, K., Adams, E., Foster, J., Hartman, J., Lai, K., Böttcher, M., Reimer, A., and Jung, I.: 2005, *ApJ* **630**, 130
- Boettcher, M., Mause, H., and Schlickeiser, R.: 1997, *Astronomy and Astrophysics* **324**, 395
- Buckley, J.: 1999, in *International Cosmic Ray Conference*, pp 267–+
- Buckley, J. H., Akerlof, C. W., Biller, S., Carter-Lewis, D. A., Catanese, M., Cawley, M. F., Connaughton, V., Fegan, D. J., Finley, J. P., Gaidos, J., Hillas, A. M., Kartje, J. F., Koenigl, A., Krennrich, F., Lamb, R. C., Lessard, R., Macomb, D. J., Mattox, J. R., McEnery, J. E., Mohanty, G., Quinn, J., Rodgers, A. J., Rose, H. J., Schubnel, M. S., Sembroski, G., Smith, P. S., Weekes, T. C., Wilson, C., and Zweerink, J.: 1996, *ApJL* **472**, L9+
- Burrows, D. N., Hill, J. E., Nousek, J. A., Wells, A., Short, A., Turner, M., Citterio, O., Tagliaferri, G., and Chincarini, G.: 2003, in G. R. Ricker and R. K. Vanderspek (eds.), *AIP Conf. Proc. 662: Gamma-Ray Burst and Afterglow Astronomy 2001: A Workshop Celebrating the First Year of the HETE Mission*, pp 488–490
- Catanese, M. and Sambruna, R. M.: 2000, *ApJL* **534**, L39
- Catanese, M. and Weekes, T. C.: 1999, *Publ. Astron. Soc. Pac.* **111**, 1193
- Cawley, M. F., Fegan, D. J., Harris, K., Kwok, P. W., Hillas, A. M., Lamb, R. C., Lang, M. J., Lewis, D. A., Macomb, D., Reynolds, P. T., Schmid, D. J., Vacanti, G., and Weekes, T. C.: 1990, *Experimental Astronomy* **1**, 173
- Celik, O.: 2007, in *VERITAS Collaboration Meeting*

- Chiappetti, L., Maraschi, L., Tavecchio, F., Celotti, A., Fossati, G., Ghisellini, G., Giommi, P., Pian, E., Tagliaferri, G., Treves, A., Urry, C. M., and Zhang, Y. H.: 1999, *ApJ* **521**, 552
- Clark, G. W., Garmire, G. P., and Kraushaar, W. L.: 1968, *ApJL* **153**, L203+
- Coppi, P. S.: 1992, *MNRAS* **258**, 657
- Coppi, P. S. and Aharonian, F. A.: 1999, *ApJL* **521**, L33
- Cui, W.: 2006, *ArXiv Astrophysics e-prints*, astro-ph/0608042
- Danaher, S., Fegan, D. J., Porter, N. A., Weekes, T. C., and Cole, T.: 1982, *Solar Energy* **28**, 335
- Daum, A., Hermann, G., Hess, M., Hofmann, W., Lampeitl, H., Pühlhofer, G., Aharonian, F., Akhperjanian, A. G., Barrio, J. A., Beglarian, A. S., Bernlöhr, K., Beteta, J. J. G., Bradbury, S. M., Contreras, J. L., Cortina, J., Deckers, T., Feigl, E., Fernandez, J., Fonseca, V., Frass, A., Funk, B., Gonzalez, J. C., Heinzlmann, G., Hemberger, M., Heusler, A., Holl, I., Horns, D., Kankanyan, R., Kirstein, O., Köhler, C., Konopelko, A., Kranich, D., Krawczynski, H., Kornmayer, H., Lindner, A., Lorenz, E., Magnussen, N., Meyer, H., Mirzoyan, R., Möller, H., Moralejo, A., Padilla, L., Panter, M., Petry, D., Plaga, R., Prahl, J., Prosch, C., Rauterberg, G., Rhode, W., Röhring, A., Sahakian, V., Samorski, M., Sanchez, J. A., Schmele, D., Stamm, W., Ulrich, M., Völk, H. J., Westerhoff, S., Wiebel-Sooth, B., Wiedner, C. A., Willmer, M., and Wirth, H.: 1997, *Astroparticle Physics* **8**, 1
- Davies, J. M. and Cotton, E. S.: 1957, *Solar Energy* **1**, 16
- Dingus, B. L., Atkins, R., Benbow, W., Berley, D., Chen, M. L., Coyne, D. G., Dorfan, D. E., Ellsworth, R. W., Evans, D., Falcone, A., Fleysher, L., Fleysher, R., Gisler, G., Goodman, J. A., Haines, T. J., Hoffman, C. M., Hugenberber, S., Kelley, L. A., Leonor, I., McConnell, M., McCullough, J. F., McEnery, J. E., Miller, R. S., Mincer, A. I., Morales, M. F., Nemethy, P., Ryan, J. M., Shen, B., Shoup, A., Sinnis, C., Smith, A. J., Sullivan, G. W., Tumer, T., Wang, K., Wascko, M. O., Westerhoff, S., Williams, D. A., and Yang, T.: 2000, in M. L. McConnell and J. M. Ryan (eds.), *American Institute of Physics Conference Series*, pp 642–+
- Edelson, R. A. and Krolik, J. H.: 1988, *ApJ* **333**, 646
- Fenimore, E. E., Laros, J. G., Klebesadel, R. W., Stockdale, R. E., and Kane, S. R.: 1982, in R. E. Lingens, H. S. Hudson, and D. M. Worall (eds.), *AIP Conf. Proc. 77: Gamma Ray Transients and Related Astrophysical Phenomena*, pp 201–209
- Fichtel, C. E., Bertsch, D. L., Hartman, R. C., Hunter, S. D., Kanbach, G., Kniffen, D. A., Kwok, P. W., Lin, Y. C., Mattox, J. R., Mayer-Hasselwander, H. A., Michelson, P. F., von Montigny, C., Nolan, P. L., Pinkau, K., Rothermel, H., Schneid,

- E. J., Sommer, M., Sreekumar, P., and Thompson, D. J.: 1993, *Astronomy and Astrophysics Supplement Series* **97**, 13
- Gaidos, J. A., Akerlof, C. W., Biller, S. D., Boyle, P. J., Breslin, A. C., Buckley, J. H., Carter-Lewis, D. A., Catanese, M., Cawley, M. F., Fegan, D. J., Finley, J. P., Hillas, A. M., Krennrich, F., Lamb, R. C., Lessard, R., McEnery, J., Mohanty, G., Moriarty, P., Quinn, J., Rodgers, A., Rose, H. J., Samuelson, F., Schubnell, M. S., Sembroski, G., Srinivasan, R., Weekes, T. C., Wilson, C. L., and Zweerink, J.: 1996, *Nature* **383**, 319
- Gehrels, N., Chipman, E., and Kniffen, D. A.: 1993, *Astronomy and Astrophysics Supplement Series* **97**, 5
- Ghisellini, G.: 1999, *Astroparticle Physics* **11**, 11
- Ghisellini, G., Tavecchio, F., and Chiaberge, M.: 2005, *Astronomy and Astrophysics* **432**, 401
- Gingrich, D. M., Boone, L. M., Bramel, D., Carson, J., Covault, C. E., Fortin, P., Hanna, D. S., Hinton, J. A., Jarvis, A., Kildea, J., Lindner, T., Mueller, C., Mukherjee, R., Ong, R. A., Ragan, K., Scalzo, R. A., Theoret, C. G., Williams, D. A., and Zweerink, J. A.: 2005, *ArXiv Astrophysics e-prints*, astro-ph/0506613
- Ginzburg, V. L. and Syrovatskii, S. I.: 1969, *Ann. Rev. Astron. Astrophys.* **7**, 375
- Gould, R. J. and Schröder, G. P.: 1967, *Phys. Rev.* **155**, 1408
- Hartman, R. C., Bertsch, D. L., Bloom, S. D., Chen, A. W., Deines-Jones, P., Esposito, J. A., Fichtel, C. E., Friedlander, D. P., Hunter, S. D., McDonald, L. M., Sreekumar, P., Thompson, D. J., Jones, B. B., Lin, Y. C., Michelson, P. F., Nolan, P. L., Tompkins, W. F., Kanbach, G., Mayer-Hasselwander, H. A., Mücke, A., Pohl, M., Reimer, O., Kniffen, D. A., Schneid, E. J., von Montigny, C., Mukherjee, R., and Dingus, B. L.: 1999, *ApJS* **123**, 79
- Henri, G. and Saugé, L.: 2006, *ApJ* **640**, 185
- Hermann, G.: 2006, in *Ground-based Gamma-ray Astronomy: Towards the Future*
- Hoffman, C. M., Sinnis, C., Fleury, P., and Punch, M.: 1999, *Reviews of Modern Physics* **71**, 897
- Holder, J., Atkins, R. W., Badran, H. M., Blaylock, G., Bradbury, S. M., Buckley, J. H., Byrum, K. L., Carter-Lewis, D. A., Celik, O., Chow, Y. C. K., Cogan, P., Cui, W., Daniel, M. K., de La Calle Perez, I., Dowdall, C., Dowkontt, P., Duke, C., Falcone, A. D., Fegan, S. J., Finley, J. P., Fortin, P., Fortson, L. F., Gibbs, K., Gillanders, G., Glidewell, O. J., Grube, J., Gutierrez, K. J., Gyuk, G., Hall, J., Hanna, D., Hays, E., Horan, D., Hughes, S. B., Humensky, T. B., Imran, A.,

- Jung, I., Kaaret, P., Kenny, G. E., Kieda, D., Kildea, J., Knapp, J., Krawczynski, H., Krennrich, F., Lang, M. J., Lebohec, S., Linton, E., Little, E. K., Maier, G., Manseri, H., Milovanovic, A., Moriarty, P., Mukherjee, R., Ogden, P. A., Ong, R. A., Petry, D., Perkins, J. S., Pizlo, F., Pohl, M., Quinn, J., Ragan, K., Reynolds, P. T., Roache, E. T., Rose, H. J., Schroedter, M., Sembroski, G. H., Sleege, G., Steele, D., Swordy, S. P., Syson, A., Toner, J. A., Valcarcel, L., Vassiliev, V. V., Wakely, S. P., Weekes, T. C., White, R. J., Williams, D. A., and Wagner, R.: 2006, *Astroparticle Physics* **25**, 391
- Holt, S., Neff, S. G., and Urry, C. M.: 1992, *Testing the AGN Paradigm*, Springer Verlag
- Horan, D.: 2001, *Ph.D. thesis*, University College Dublin
- Horan, D. and Weekes, T. C.: 2004, *New Astronomy Review* **48**, 527
- Inoue, S. and Takahara, F.: 1996, *ApJ* **463**, 555
- Jahoda, K., Markwardt, C. B., Radeva, Y., Rots, A. H., Stark, M. J., Swank, J. H., Strohmayer, T. E., and Zhang, W.: 2006, *ApJS* **163**, 401
- Jelley, J. V.: 1958, *Cerenkov Radiation and its Applications*, Pergamon Press, New York
- Katz, J. I.: 2006, *ArXiv Astrophysics e-prints*, astro-ph/0603772
- Kertzman, M. P. and Sembroski, G. H.: 1994, *Nuclear Instruments and Methods in Physics Research A* **343**, 629
- Kino, M., Takahara, F., and Kusunose, M.: 2002, *ApJ* **564**, 97
- Kirk, J. G. and Duffy, P.: 1999, *Journal of Physics G Nuclear Physics* **25**, 163
- Kirk, J. G. and Mastichiadis, A.: 1999, *Astroparticle Physics* **11**, 45
- Konopelko, A., Mastichiadis, A., Kirk, J., de Jager, O. C., and Stecker, F. W.: 2003, *ApJ* **597**, 851
- Kosack, K.: 2005, *Ph.D. thesis*, Washington University in St. Louis
- Kosack, K., Badran, H. M., Bond, I. H., Boyle, P. J., Bradbury, S. M., Buckley, J. H., Carter-Lewis, D. A., Celik, O., Connaughton, V., Cui, W., Daniel, M., D'Vali, M., de la Calle Perez, I., Duke, C., Falcone, A., Fegan, D. J., Fegan, S. J., Finley, J. P., Fortson, L. F., Gaidos, J. A., Gammell, S., Gibbs, K., Gillanders, G. H., Grube, J., Gutierrez, K., Hall, J., Hall, T. A., Hanna, D., Hillas, A. M., Holder, J., Horan, D., Jarvis, A., Jordan, M., Kenny, G. E., Kertzman, M., Kieda, D., Kildea, J., Knapp, J., Krawczynski, H., Krennrich, F., Lang, M. J., Le Bohec, S., Linton, E., Lloyd-Evans, J., Milovanovic, A., McEnery, J., Moriarty, P., Muller, D., Nagai,

- T., Nolan, S., Ong, R. A., Pallassini, R., Petry, D., Power-Mooney, B., Quinn, J., Quinn, M., Ragan, K., Rebillot, P., Reynolds, P. T., Rose, H. J., Schroedter, M., Sembroski, G. H., Swordy, S. P., Syson, A., Vassiliev, V. V., Wakely, S. P., Walker, G., Weekes, T. C., and Zweerink, J.: 2004, *ApJL* **608**, L97
- Krawczynski, H.: 2004, *New Astronomy Review* **48**, 367
- Krawczynski, H.: 2005, *ArXiv Astrophysics e-prints*, astro-ph/0508621
- Krawczynski, H.: 2006, *ArXiv Astrophysics e-prints*, astro-ph/0610641
- Krawczynski, H., Coppi, P. S., and Aharonian, F.: 2002, *MNRAS* **336**, 721
- Krawczynski, H., Coppi, P. S., Maccarone, T., and Aharonian, F. A.: 2000, *Astronomy and Astrophysics* **353**, 97
- Krawczynski, H., Hughes, S. B., Horan, D., Aharonian, F., Aller, M. F., Aller, H., Boltwood, P., Buckley, J., Coppi, P., Fossati, G., Götting, N., Holder, J., Horns, D., Kurtanidze, O. M., Marscher, A. P., Nikolashvili, M., Remillard, R. A., Sadun, A., and Schröder, M.: 2004, *ApJ* **601**, 151
- Krawczynski, H., Sambruna, R., Kohnle, A., Coppi, P. S., Aharonian, F., Akhperjanian, A., Barrio, J., Bernlöhr, K., Börst, H., Bojahr, H., Bolz, O., Contreras, J., Cortina, J., Denninghoff, S., Fonseca, V., Gonzalez, J., Götting, N., Heinzelmann, G., Hermann, G., Heusler, A., Hofmann, W., Horns, D., Ibarra, A., Jung, I., Kankanyan, R., Kestel, M., Kettler, J., Konopelko, A., Kornmeyer, H., Kranich, D., Lampeitl, H., Lorenz, E., Lucarelli, F., Magnussen, N., Mang, O., Meyer, H., Mirzoyan, R., Moralejo, A., Padilla, L., Panter, M., Plaga, R., Plyasheshnikov, A., Pühlhofer, G., Rauterberg, G., Röhring, A., Rhode, W., Rowell, G., Sahakian, V., Samorski, M., Schilling, M., Schröder, F., Siems, M., Stamm, W., Tluczykont, M., Völk, H. J., Wiedner, C. A., and Wittek, W.: 2001, *ApJ* **559**, 187
- Krennrich, F., Bond, I. H., Bradbury, S. M., Buckley, J. H., Carter-Lewis, D. A., Cui, W., de la Calle Perez, I., Fegan, D. J., Fegan, S. J., Finley, J. P., Gaidos, J. A., Gibbs, K., Gillanders, G. H., Hall, T. A., Hillas, A. M., Holder, J., Horan, D., Jordan, M., Kertzman, M., Kieda, D., Kildea, J., Knapp, J., Kosack, K., Lang, M. J., LeBohec, S., Moriarty, P., Müller, D., Ong, R. A., Pallassini, R., Petry, D., Quinn, J., Reay, N. W., Reynolds, P. T., Rose, H. J., Sembroski, G. H., Sidwell, R., Stanton, N., Swordy, S. P., Vassiliev, V. V., Wakely, S. P., and Weekes, T. C.: 2002, *ApJL* **575**, L9
- Levine, A. M., Bradt, H., Cui, W., Jernigan, J. G., Morgan, E. H., Remillard, R., Shirey, R. E., and Smith, D. A.: 1996, *ApJL* **469**, L33+
- Levinson, A.: 2005, in *KITP Program: Physics of Astrophysical Outflows and Accretion Disks*

- Longair, M. S.: 1992, *High Energy Astrophysics Volume 1: Particles, photons, and their detection*, Cambridge University Press, Cambridge
- Lorenz, E. and Martinez, M.: 2005, *Astronomy and Geophysics* **46**, 21
- Maraschi, L., Ghisellini, G., and Celotti, A.: 1992, *ApJL* **397**, L5
- Mastichiadis, A. and Kirk, J. G.: 1997, *Astronomy and Astrophysics* **320**, 19
- Mimica, P., Aloy, M. A., Müller, E., and Brinkmann, W.: 2004, *Astronomy and Astrophysics* **418**, 947
- Morselli, A.: 2003, *Chinese Journal of Astronomy and Astrophysics Supplement* **3**, 523
- Perkins, J. S.: 2006, *Ph.D. thesis*, Washington University in St. Louis
- Pian, E., Vacanti, G., Tagliaferri, G., Ghisellini, G., Maraschi, L., Treves, A., Urry, M., Fiore, F., Giommi, P., Palazzi, E., Chiappetti, L., and Sambruna, R. M.: 1998, *ApJL* **492**, L17+
- Piner, B. G. and Edwards, P. G.: 2004, *ApJ* **600**, 115
- Piner, B. G. and Edwards, P. G.: 2005, *ApJ* **622**, 168
- Pühlhofer, G., Bolz, O., Götting, N., Heusler, A., Horns, D., Kohnle, A., Lampeitl, H., Panter, M., Tluczykont, M., Aharonian, F., Akhperjanian, A., Beilicke, M., Bernlöhr, K., Börst, H., Bojahr, H., Coarasa, T., Contreras, J. L., Cortina, J., Denninghoff, S., Fonseca, M. V., Girma, M., Heinzelmann, G., Hermann, G., Hofmann, W., Jung, I., Kankanyan, R., Kestel, M., Konopelko, A., Kornmeyer, H., Kranich, D., Lopez, M., Lorenz, E., Lucarelli, F., Mang, O., Meyer, H., Mirzoyan, R., Moralejo, A., Ona-Wilhelmi, E., Plyasheshnikov, A., de Los Reyes, R., Rhode, W., Ripken, J., Rowell, G., Sahakian, V., Samorski, M., Schilling, M., Siems, M., Sobzynska, D., Stamm, W., Vitale, V., Völk, H. J., Wiedner, C. A., and Wittek, W.: 2003, *Astroparticle Physics* **20**, 267
- Punch, M., Akerlof, C. W., Cawley, M. F., Chantell, M., Fegan, D. J., Fennell, S., Gaidos, J. A., Hagan, J., Hillas, A. M., Jiang, Y., Kerrick, A. D., Lamb, R. C., Lawrence, M. A., Lewis, D. A., Meyer, D. I., Mohanty, G., O'Flaherty, K. S., Reynolds, P. T., Rovero, A. C., Schubnell, M. S., Sembroski, G., Weekes, T. C., and Wilson, C.: 1992, *Nature* **358**, 477
- Rebillot, P. F., Badran, H. M., Blaylock, G., Bradbury, S. M., Buckley, J. H., Carter-Lewis, D. A., Celik, O., Chow, Y. C., Cogan, P., Cui, W., Daniel, M., Duke, C., Falcone, A., Fegan, S. J., Finley, J. P., Fortson, L. F., Gillanders, G. H., Grube, J., Gutierrez, K., Gyuk, G., Hanna, D., Holder, J., Horan, D., Hughes, S. B., Kenny, G. E., Kertzman, M., Kieda, D., Kildea, J., Kosack, K., Krawczynski,

- H., Krennrich, F., Lang, M. J., Le Bohec, S., Linton, E., Maier, G., Moriarty, P., Perkins, J., Pohl, M., Quinn, J., Ragan, K., Reynolds, P. T., Rose, H. J., Schroedter, M., Sembroski, G. H., Steele, G., Swordy, S. P., Valcarcel, L., Vassiliev, V. V., Wakely, S. P., Weekes, T. C., Zweerink, J., VERITAS Collaboration, Aller, M., Aller, H., Boltwood, P., Jung, I., Kranich, D., Nilsson, K., Pasanen, M., Sadun, A., and Sillanpaa, A.: 2006, *ApJ* **641**, 740
- Reynolds, P. T., Akerlof, C. W., Cawley, M. F., Chantell, M., Fegan, D. J., Hillas, A. M., Lamb, R. C., Lang, M. J., Lawrence, M. A., Lewis, D. A., Macomb, D., Meyer, D. I., Mohanty, G., O’Flaherty, K. S., Punch, M., Schubnell, M. S., Vacanti, G., Weekes, T. C., and Whitaker, T.: 1993, *ApJ* **404**, 206
- Ritz, S., Grindlay, J., Meegan, C., Michelson, P. F., and GLAST Mission Team: 2005, in *Bulletin of the American Astronomical Society*, pp 1198–+
- Rothschild, R. E., Blanco, P. R., Gruber, D. E., Heindl, W. A., MacDonald, D. R., Marsden, D. C., Pelling, M. R., Wayne, L. R., and Hink, P. L.: 1998, *ApJ* **496**, 538
- Rybicki, G. B. and Lightman, A. P.: 1979, *Radiative Processes in Astrophysics*, John Wiley & Sons, New York
- Sambruna, R. M., Aharonian, F. A., Krawczynski, H., Akhperjanian, A. G., Barrio, J. A., Bernlöhner, K., Bojahr, H., Calle, I., Contreras, J. L., Cortina, J., Denninghoff, S., Fonseca, V., Gonzalez, J. C., Götting, N., Heinzlmann, G., Hemberger, M., Hermann, G., Heusler, A., Hofmann, W., Horns, D., Ibarra, A., Kankanyan, R., Kestel, M., Kettler, J., Köhler, C., Kohnle, A., Konopelko, A., Kornmeyer, H., Kranich, D., Lampeitl, H., Lindner, A., Lorenz, E., Magnussen, N., Mang, O., Meyer, H., Mirzoyan, R., Moralejo, A., Padilla, L., Panter, M., Plaga, R., Plyashnikov, A., Prahl, J., Pühlhofer, G., Rauterberg, G., Röhring, A., Sahakian, V., Samorski, M., Schilling, M., Schmele, D., Schröder, F., Stamm, W., Tluczykont, M., Völk, H. J., Wiebel-Sooth, B., Wiedner, C., Willmer, M., Wittek, W., Chou, L., Coppi, P. S., Rothschild, R., and Urry, C. M.: 2000, *ApJ* **538**, 127
- Schmitt, J. L.: 1968, *Nature* **218**, 663
- Sembay, S., Edelson, R., Markowitz, A., Griffiths, R. G., and Turner, M. J. L.: 2002, *ApJ* **574**, 634
- Sikora, M. and Madejski, G.: 2001, in F. A. Aharonian and H. J. Völk (eds.), *American Institute of Physics Conference Series*, pp 275–+
- Smith, D. A., Brion, E., Britto, R., Bruel, P., Bussons Gordo, J., Dumora, D., Durand, E., Eschstruth, P., Espigat, P., Holder, J., Jacholkowska, A., Lavallo, J., Le Gallou, R., Lott, B., Manseri, H., Münz, F., Nuss, E., Piron, F., Rannot, R. C., Reposeur, T., and Sako, T.: 2006, *Astronomy and Astrophysics* **459**, 453

- Sokolov, A. and Marscher, A. P.: 2005, *ApJ* **629**, 52
- Stecker, F. W., de Jager, O. C., and Salamon, M. H.: 1992, *ApJL* **390**, L49
- Takahashi, T., Kataoka, J., Madejski, G., Mattox, J., Urry, C. M., Wagner, S., Aharonian, F., Catanese, M., Chiappetti, L., Coppi, P., Degrange, B., Fossati, G., Kubo, H., Krawczynski, H., Makino, F., Marshall, H., Maraschi, L., Piron, F., Remillard, R., Takahara, F., Tashiro, M., Terasranta, H., and Weekes, T.: 2000, *ApJL* **542**, L105
- Takahashi, T., Tashiro, M., Madejski, G., Kubo, H., Kamae, T., Kataoka, J., Kii, T., Makino, F., Makishima, K., and Yamasaki, N.: 1996, *ApJL* **470**, L89+
- Tanihata, C., Urry, C. M., Takahashi, T., Kataoka, J., Wagner, S. J., Madejski, G. M., Tashiro, M., and Kouda, M.: 2001, *ApJ* **563**, 569
- Tavecchio, F.: 2005, in M. Novello, S. Perez Bergliaffa, and R. Ruffini (eds.), *The Tenth Marcel Grossmann Meeting. On recent developments in theoretical and experimental general relativity, gravitation and relativistic field theories*, pp 512–529
- Tavecchio, F., Maraschi, L., and Ghisellini, G.: 1998, *ApJ* **509**, 608
- Ter Haar, D.: 1950, *Reviews of Modern Physics* **22**, 119
- Thompson, D. J., Bertsch, D. L., Dingus, B. L., Esposito, J. A., Etienne, A., Fichtel, C. E., Friedlander, D. P., Hartman, R. C., Hunter, S. D., Kendig, D. J., Mattox, J. R., McDonald, L. M., von Montigny, C., Mukherjee, R., Ramanamurthy, P. V., Sreekumar, P., Fierro, J. M., Lin, Y. C., Michelson, P. F., Nolan, P. L., Shriver, S. K., Willis, T. D., Kanbach, G., Mayer-Hasselwander, H. A., Merck, M., Radecke, H.-D., Kniffen, D. A., and Schneid, E. J.: 1995, *ApJS* **101**, 259
- Vincent, P.: 2005, in *International Cosmic Ray Conference*, pp 163–+
- Weekes, T.: 2003, *Very High Energy Gamma-Ray Astronomy*, Institute of Physics Publishing, Bristol
- Weekes, T. C., Badran, H., Biller, S. D., Bond, I., Bradbury, S., Buckley, J., Carter-Lewis, D., Catanese, M., Criswell, S., Cui, W., Dowkontt, P., Duke, C., Fegan, D. J., Finley, J., Fortson, L., Gaidos, J., Gillanders, G. H., Grindlay, J., Hall, T. A., Harris, K., Hillas, A. M., Kaaret, P., Kertzman, M., Kieda, D., Krennrich, F., Lang, M. J., LeBohec, S., Lessard, R., Lloyd-Evans, J., Knapp, J., McKernan, B., McEnery, J., Moriarty, P., Muller, D., Ogden, P., Ong, R., Petry, D., Quinn, J., Reay, N. W., Reynolds, P. T., Rose, J., Salamon, M., Sembroski, G., Sidwell, R., Slane, P., Stanton, N., Swordy, S. P., Vassiliev, V. V., and Wakely, S. P.: 2002, *Astroparticle Physics* **17**, 221

Weekes, T. C., Cawley, M. F., Fegan, D. J., Gibbs, K. G., Hillas, A. M., Kowk, P. W., Lamb, R. C., Lewis, D. A., Macomb, D., Porter, N. A., Reynolds, P. T., and Vacanti, G.: 1989, *ApJ* **342**, 379

Weekes, T. C. and Turver, K. E.: 1977, in R. D. Wills and B. Battick (eds.), *ESA SP-124: Recent Advances in Gamma-Ray Astronomy*, pp 279–286